



## 저작자표시-비영리 2.0 대한민국

이용자는 아래의 조건을 따르는 경우에 한하여 자유롭게

- 이 저작물을 복제, 배포, 전송, 전시, 공연 및 방송할 수 있습니다.
- 이차적 저작물을 작성할 수 있습니다.

다음과 같은 조건을 따라야 합니다:



저작자표시. 귀하는 원저작자를 표시하여야 합니다.



비영리. 귀하는 이 저작물을 영리 목적으로 이용할 수 없습니다.

- 귀하는, 이 저작물의 재이용이나 배포의 경우, 이 저작물에 적용된 이용허락조건을 명확하게 나타내어야 합니다.
- 저작권자로부터 별도의 허가를 받으면 이러한 조건들은 적용되지 않습니다.

저작권법에 따른 이용자의 권리는 위의 내용에 의하여 영향을 받지 않습니다.

이것은 [이용허락규약\(Legal Code\)](#)을 이해하기 쉽게 요약한 것입니다.

[Disclaimer](#) 

이학박사 학위논문

Spin Dynamics in Multiferroic  $\text{BiFeO}_3$ :  
Interplay of Dzyaloshinskii-Moriya Interaction  
and Anisotropy

다강체  $\text{BiFeO}_3$ 의 스핀동역학 연구:  
Dzyaloshinskii-Moriya 상호작용과  
비등방성의 상호 영향

2015년 2월

서울대학교 대학원  
물리천문학부 물리학전공  
정재홍



Spin Dynamics in Multiferroic BiFeO<sub>3</sub>:  
Interplay of Dzyaloshinskii-Moriya Interaction  
and Anisotropy

지도 교수 박 제 근

이 논문을 이학박사 학위논문으로 제출함

2015년 2월

서울대학교 대학원  
물리천문학부 물리학전공

정 재 홍

정재홍의 이학박사 학위논문을 인준함

2014년 12월

위 원 장 \_\_\_\_\_ (인)

부위원장 \_\_\_\_\_ (인)

위 원 \_\_\_\_\_ (인)

위 원 \_\_\_\_\_ (인)

위 원 \_\_\_\_\_ (인)



# Abstract

Multiferroic materials, which exhibit both ferroelectricity and magnetism simultaneously, have attracted huge interest for coexistence of two different order parameters and the coupling between them. These compounds have been widely studied for new devices using the magnetoelectric coupling. Bismuth ferrite,  $\text{BiFeO}_3$  is an excellent candidate because it is the only example that shows multiferroicity above room temperature with a ferroelectric transition at  $T_C \simeq 1100$  K and an antiferromagnetic transition at  $T_N \simeq 640$  K. It also has a complex magnetic structure below  $T_N$ : an incommensurate spin cycloid with an extremely long period of  $\approx 620$  Å and a weak ferromagnetic local moment induced by spin canting perpendicular to the cycloid plane. In order to understand the nature of the complex magnetic structure and the magnetoelectric coupling, it is important to investigate spin dynamics and hence determine the spin Hamiltonian.

In this study, magnon and phonon excitations in  $\text{BiFeO}_3$  were measured by inelastic neutron scattering experiments on single crystals, and the fundamental spin Hamiltonian was constructed. Although the inelastic neutron scattering technique is the most efficient way to observe magnetic excitations, it is necessary to prepare a large amount of the sample. Ten single crystals with the total mass of 1.8 g were coaligned within 2 degrees using the neutron four-circle diffractometer FCD at HANARO. The spin waves dispersion was measured over the entire Brillouin zone using two time-of-flight spectrometers: AMATERAS at J-PARC and MERLIN at ISIS. The full spin waves up to 72.5 meV can be explained by a simple spin Hamiltonian with two exchange interactions for the nearest and next nearest neighbors. In order to observe small effects induced by the complex magnetic structure, the magnon dispersion was measured around the magnetic zone center at low energy at various temperatures using the cold neutron triple-axis spectrometer 4F2 at LLB. The higher energy part of magnon and phonon spectrum was also measured using a thermal triple-axis spectrometer 1T1 at LLB. Low-energy magnon excitations in  $\text{BiFeO}_3$  show unique features associated directly with the interplay of the Dzyaloshinskii-Moriya interaction and a small single-ion anisotropy. These two interactions are the most important to understand the unusual magnetic ground state and the magnetoelectric coupling in this material. For the theoretical calculation of the magnon dispersion with the full spin Hamiltonian, perturbative methods based on the linear spin wave theory

in the rotating frame were developed. By carefully examining the experimental data with several model calculations, all parameters of the spin Hamiltonian were determined as a function of temperature. The easy-axis type anisotropy was confirmed and the anharmonicity of the spin cycloid was also determined. Temperature dependence of the parameters was described with a direct connection to the physical properties and structural deformations in  $\text{BiFeO}_3$ . Taking advantage of a wide energy-momentum coverage of the inelastic neutron scattering, phonon dispersions in  $\text{BiFeO}_3$  were also measured.

**Keywords:** multiferroic,  $\text{BiFeO}_3$ , magnon, spin waves, inelastic neutron scattering

**Student Number:** 2007-20440

# Contents

<b>1</b>	<b>Introduction</b>	<b>1</b>
1.1	Multiferroics and the DM interaction . . . . .	1
1.2	Room temperature multiferroic BiFeO <sub>3</sub> . . . . .	5
1.3	Outline of thesis . . . . .	8
<b>2</b>	<b>Experimental techniques</b>	<b>11</b>
2.1	Inelastic neutron scattering technique . . . . .	11
2.1.1	Advantages of neutron scattering . . . . .	11
2.1.2	Techniques for inelastic neutron scattering . . . . .	14
2.2	Detector trajectory in ToF measurement . . . . .	17
2.2.1	Measurement for 1- and 2-dimensional systems . . . . .	18
2.2.2	Measurement for 3-dimensional systems . . . . .	21
2.3	Single crystal experiments on AMATERAS, MERLIN and 4F2 . . . . .	21
2.3.1	Coalignment of single crystals . . . . .	21
2.3.2	ToF spectrometer AMATERAS with fixed geometry . . . . .	24
2.3.3	ToF spectrometer MERLIN with the sample rotation method . . . . .	25
2.3.4	Cold-neutron triple-axis spectrometer 4F2 . . . . .	27
<b>3</b>	<b>Spin waves calculations</b>	<b>31</b>
3.1	Effective spin Hamiltonian . . . . .	31
3.1.1	Landau-Ginzberg free energy . . . . .	31
3.1.2	Microscopic spin Hamiltonian . . . . .	31
3.1.3	DM interaction and single-ion anisotropy . . . . .	33
3.2	Linear spin wave theory on a rotating frame . . . . .	35
3.2.1	Holstein-Primakoff transform . . . . .	35
3.2.2	Rotating local frame method . . . . .	38
3.2.3	Simple cycloid systems: $\mathcal{J}$ - $\mathcal{J}'$ - $\mathcal{D}_u$ model . . . . .	38
3.3	Perturbative treatment for the complex ground states . . . . .	41
3.3.1	Canted spin cycloid: $\mathcal{J}$ - $\mathcal{J}'$ - $\mathcal{D}_u$ - $\mathcal{D}_c$ model . . . . .	41
3.3.2	Anharmonic spin cycloid: $\mathcal{J}$ - $\mathcal{J}'$ - $\mathcal{D}_u$ - $\mathcal{K}$ model . . . . .	44

<b>4</b>	<b>Magnon and phonon excitations in BiFeO<sub>3</sub></b>	<b>49</b>
4.1	High energy spin waves governed by exchange interactions . . . . .	49
4.1.1	Analysis of AMATERAS data . . . . .	49
4.1.2	Analysis of MERLIN data . . . . .	51
4.1.3	Determination of superexchange interactions . . . . .	53
4.2	Low energy spin waves governed by DM interaction and anisotropy	57
4.2.1	Analysis of 4F2 data . . . . .	57
4.2.2	Model Hamiltonian and simulations . . . . .	59
4.2.3	Determination of DM interaction and SIA . . . . .	61
4.2.4	Temperature dependence of interaction parameters . . . . .	61
4.3	Phonon dispersion in BiFeO <sub>3</sub> . . . . .	65
4.3.1	Analysis of MERLIN, 4F2 and 1T1 data . . . . .	65
<b>5</b>	<b>Summary</b>	<b>69</b>
<b>A</b>	<b>Magnetic ground state</b>	<b>71</b>
A.1	Hexagonal vs. pseudocubic notations . . . . .	71
A.2	Spin cycloid: $\mathcal{J}$ - $\mathcal{J}'$ - $\mathcal{D}_u$ model . . . . .	72
A.3	Canted spin cycloid: $\mathcal{J}$ - $\mathcal{J}'$ - $\mathcal{D}_u$ - $\mathcal{D}_c$ model . . . . .	73
A.4	Anharmonic spin cycloid: $\mathcal{J}$ - $\mathcal{J}'$ - $\mathcal{D}_u$ - $\mathcal{K}$ model . . . . .	76
A.5	Anharmonicity of spin cycloid . . . . .	79
<b>B</b>	<b>Equivalence of L-G free energy and spin Hamiltonian</b>	<b>85</b>
<b>C</b>	<b>Codes for the detector trajectory</b>	<b>89</b>
<b>D</b>	<b>Codes for the spin waves calculations</b>	<b>95</b>
	<b>References</b>	<b>115</b>
	국문초록	121
	<b>Acknowledgements</b>	<b>123</b>

# List of Tables

1.1	Basic prime ferroicities . . . . .	1
4.1	Temperature dependence of interaction parameters . . . . .	63



# List of Figures

1.1	Prime ferroicities and multiferroicity . . . . .	3
1.2	The number of related publications . . . . .	3
1.3	Single crystals and huge polarization of BiFeO <sub>3</sub> . . . . .	5
1.4	Atomic structure of BiFeO <sub>3</sub> . . . . .	7
1.5	Complex magnetic structure of BiFeO <sub>3</sub> . . . . .	8
2.1	Scattering cross-section of X-ray and neutrons . . . . .	12
2.2	Coverage of inelastic neutron scattering . . . . .	13
2.3	Excitations measurement using neutrons . . . . .	13
2.4	Time-of-flight inelastic neutron scattering technique . . . . .	15
2.5	Neutron triple-axis spectrometry . . . . .	16
2.6	Detector trajectory in ToF measurement . . . . .	17
2.7	ToF measurement for 1D systems . . . . .	19
2.8	ToF measurement for 2D systems . . . . .	19
2.9	ToF measurement for 3D systems . . . . .	20
2.10	Neutron four-circle diffractometer FCD at HANARO . . . . .	22
2.11	Design for sample holders . . . . .	22
2.12	Full assembly of single crystals . . . . .	23
2.13	Final mosaicity results after coalignment . . . . .	23
2.14	AMATERAS beamline at J-PARC in Japan . . . . .	24
2.15	Detector coverage in the AMATERAS experiment . . . . .	25
2.16	MERLIN beamline at ISIS in UK . . . . .	26
2.17	Detector coverage with sample rotation method . . . . .	26
2.18	4F2 beamline at LLB in France . . . . .	28
2.19	Scanning with the resolution ellipsoid . . . . .	28
3.1	Superexchange interactions . . . . .	32
3.2	Dzyaloshinskii-Moriya interaction . . . . .	34
4.1	Analysis of the AMATERAS data . . . . .	50
4.2	Experimental results from the AMATERAS data . . . . .	51
4.3	Analysis of the MERLIN data . . . . .	52
4.4	Full dispersion along high symmetry directions . . . . .	53
4.5	Full dispersion with $\mathcal{J}$ -only and $\mathcal{J}$ - $\mathcal{J}'$ models . . . . .	54

4.6	High energy dispersion along the L-M-L direction . . . . .	55
4.7	Calculated spin wave dispersion with $\mathcal{J}$ - $\mathcal{J}'$ and $\mathcal{J}$ - $\mathcal{J}'$ - $\mathcal{D}_u$ models .	56
4.8	Low energy magnon dispersion measured in 4F2 . . . . .	58
4.9	Calculated magnon dispersion and simulations . . . . .	60
4.10	Simulation results and the best fits for $\mathcal{J}$ , $\mathcal{D}_u$ , $\mathcal{K}$ . . . . .	62
4.11	Temperature dependence of interaction parameters . . . . .	63
4.12	Phonon dispersion measured using ToF . . . . .	66
4.13	Phonon dispersion measured using TAS . . . . .	66
4.14	Phonon dispersion calculated by DFT . . . . .	67
A.1	Anharmonicity of spin cycloid . . . . .	83
C.1	Simulation for $Q$ coverage . . . . .	93
C.2	Simulation for $Q$ - $E$ coverage . . . . .	93

# 1. Introduction

Multiferroic materials, which have more than two ferroic properties simultaneously, are studied widely and deeply in past 20 years. Especially, a compound having both ferroelectricity and ferromagnetism is hugely attractive due to possible applications for multifunctional devices. Among several multiferroic compounds,  $\text{BiFeO}_3$  is the most promising candidate because it exhibits multiferroicity above room temperature.

## 1.1 Multiferroics and the DM interaction

Materials often show large changes of physical properties in a narrow temperature range when they are cooled. This is a phase transition to an ordered state through breaking one of the symmetries in the material. While the crystal is in a nonferroic state above the critical temperature  $T_c$ , it undergoes a spontaneous phase transition to a ferroic state upon cooling down below  $T_c$ . These are usually driven by the four fundamental degrees of freedom: the electric charge, spin or orbital angular momentum or the structure of the atomic lattice. For example, in ferroelectrics, a spontaneous dipole moment is induced along the axis which breaks the inversion symmetry. Ferromagnets break time reversal symmetry, so a spontaneous magnetization is induced by a parallel ordering of electronic spins. In ferroelastic crystals, the shape of the unit cell is changed at the phase transition, hence a strain is induced (see table 1.1). Although a number of materials show one of these ferroic ordering, materials showing two or more are few.

The term *multiferroic* is formally defined as materials that exhibit more than one primary ferroic property in a single phase when it was first used by H. Schmid

Ferroicity	Induced property	Switching field	Broken symmetry
Ferroelasticity	Strain	Stress	(Point-group)
Ferroelectricity	Polarization	Electric field	Space inversion
Ferromagnetism	Magnetization	Magnetic field	Time reversal

Table 1.1: Basic prime ferroicities with spontaneously induced properties below phase transition temperature, external fields switching the properties, and broken symmetries.

in 1994. Today the term has been expanded to include any type of long range magnetic ordering, spontaneous electric polarization, and/or ferroelasticity as shown in figure 1.1. Historically, compounds having both ferroelectric and magnetic orderings were first studied as magnetoelectric materials in the 1960s. Some compounds such as  $\text{Cr}_2\text{O}_3$ ,  $\alpha\text{-Fe}_2\text{O}_3$ ,  $\text{MnCO}_3$ , and  $\text{FeBO}_3$  were examined in Russia to explain the weak ferromagnetic component in these materials [1–4]. From these studies, Dzyaloshinskii discovered that there is a new type of exchange interaction with broken inversion symmetry, and Moriya adopted the phenomenological form and derived microscopic expressions for its strength [5, 6]. This anisotropic exchange interaction, now known as the Dzyaloshinskii-Moriya (DM) interaction, can be written as  $\mathcal{H}_{\text{DM}} = \mathbf{D} \cdot \mathbf{S}_i \times \mathbf{S}_j$  with  $\mathbf{D}$  being the DM vector and  $\mathbf{S}_i$  the spin vector at the  $i$  site. Because the DM interaction is antisymmetric unlike the Heisenberg exchange interaction, it had great importance in the development of the theory of magnetism. However, it failed to attract wider interest due to the relatively few materials having such behavior, until the issue emerged again in the late 1990s and early 2000s by a number of people such as Schmid and Spaldin [7, 8]. This was the beginning of a renaissance in multiferroic research, as noted by Spaldin and Fiebig [9]. For the last 20 years, a number of new multiferroic materials were found and a large volume of papers were published including many reviews [10–17]. Over 3000 papers were counted on  $\text{BiFeO}_3$  alone by the Web of Science up to now, mostly written within the past ten years (see figure 1.2).

Because the DM interaction originates from the relativistic spin-orbit coupling microscopically, its strength scales with atomic number as  $Z^4$ . While all multiferroics discovered so far involve  $3d$  transition metal ions where the spin-orbit interaction is expected to be small, it will be interesting to find what phenomena can come from a larger spin-orbit coupling on multiferroic materials where the magnetism arises from  $4d$  or  $5d$  electrons, particularly given the recent strong interest in spin-orbit physics [18]. The DM interaction is also important as being the microscopic origin of the magnetoelectric coupling which gives rise to the magnetically induced ferroelectricity in perovskite manganites [19, 20]. In these materials, the ferroelectric ordering accompanies a magnetic spiral order. Whilst the spiral itself is caused by competition between the superexchange and DM interaction, it is the DM interaction that stabilises the oxygen displacements, causing the net electric polarization [11]. This mechanism has subsequently been

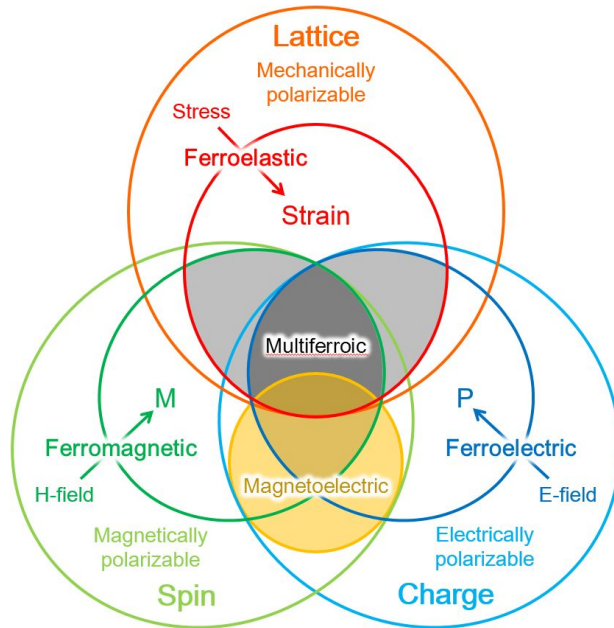


Figure 1.1: Three prime ferroicities with their associated degree of freedom and spontaneously induced ferroic properties. Light and dark gray areas denote multiferroics. The yellow shaded circle shows the region of magnetoelectric materials which includes materials without ferroic order. Adapted from [10].

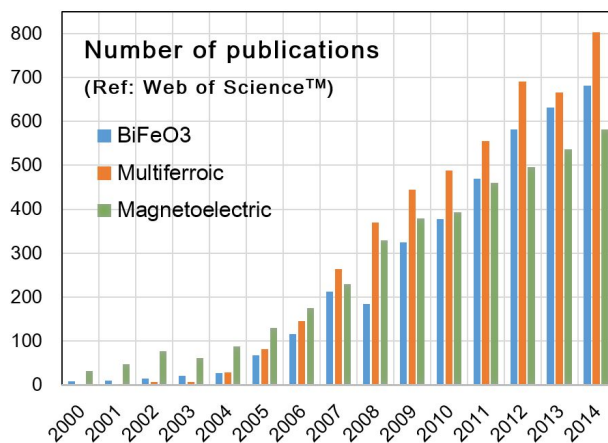


Figure 1.2: The number of publications with BiFeO<sub>3</sub>, multiferroic and magneto-electric as keywords, collected from Web of Science™.

termed the *inverse Dzyaloshinskii-Moriya interaction*, the “inverse” coming from the sense that the DM interaction causes inversion symmetry breaking rather than a non-centrosymmetric bond giving a nonzero DM interaction.

An equivalent approach, called the *spin current* mechanism or KNB model [21] also gives a net ferroelectric polarization in conjunction with a magnetic spiral, but has a different microscopic origin. The spin current  $\mathbf{j} \propto \mathbf{S}_i \times \mathbf{S}_j$  arises from the spiral, and this current induces a net polarization  $\mathbf{P} \perp \mathbf{j}$ , analogous to the magnetic moment induced by a charge current. In both these mechanisms, a magnetic spiral order breaks inversion symmetry and allows the emergence of an electric polarization [11].

The multiferroic compounds can be divided into two groups [22]: type I (or “proper”) multiferroics where there is coexistence of magnetism and ferroelectricity but each arises from different sources; and type II (“improper”) multiferroics where a magnetic order causes ferroelectricity<sup>1</sup>. The first group contains the older multiferroics, including BiFeO<sub>3</sub>, studied by early researchers in Russia, whilst the second group encompasses compounds such as the perovskite manganites (e.g. TbMnO<sub>3</sub> [23]), or MnWO<sub>4</sub> [24] which have spiral magnetic structures that break inversion symmetry, or mixed valent materials such as LuFe<sub>2</sub>O<sub>4</sub> [25] or Ca<sub>3</sub>CoMnO<sub>6</sub> [26], where the ferroelectric polarization comes from the magnetically induced polar charge ordering.

Of the many multiferroic systems thus found, several families in particular have drawn intense interests: hexagonal  $RMnO_3$ , orthorhombic (perovskite)  $RMnO_3$  and  $RMn_2O_5$  [17], and BiFeO<sub>3</sub>. While the orthorhombic  $RMnO_3$  and  $RMn_2O_5$  are attractive because they are type-II multiferroics with strong magnetoelectric couplings, the ordering occurs at quite low temperatures (< 77 K). BiFeO<sub>3</sub> and the hexagonal  $RMnO_3$ , on the other hand, have much larger transition temperatures. The microscopic magnetoelectric coupling was first demonstrated by second harmonic spectroscopy in HoMnO<sub>3</sub> [27], and later found to arise from a large magnetoelastic coupling, which is most likely to be related to

---

<sup>1</sup>Although non-standard, the “proper”/“improper” terminology, deriving from the description of ferroelectrics, is gradually coming into usage. A proper ferroelectric has the polarization as the primary order parameter, whereas in an improper ferroelectric, the polarization is a secondary (induced) order parameter. Type II multiferroics, where the polarization is induced by magnetic order is clearly an improper ferroelectric, whereas type I multiferroics (the case of BiFeO<sub>3</sub> where neither magnetic nor electric orders induce the other) may be proper or improper ferroelectrics. For example, both BiFeO<sub>3</sub> and hexagonal  $RMnO_3$  belong to the type I group although BiFeO<sub>3</sub> is often thought of as a proper ferroelectric whereas  $RMnO_3$  is known as an improper ferroelectric.

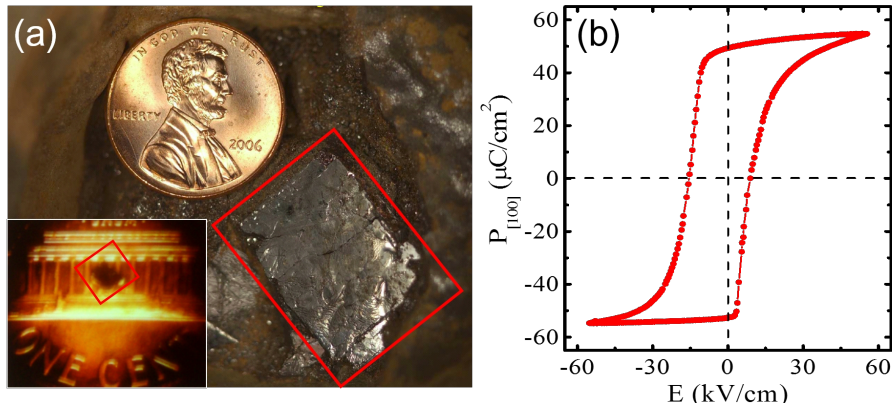


Figure 1.3: (a) Big single crystals grown by flux method. Inset shows the much smaller typical size of crystals previously available. (b) Hysteresis loop in the  $P$ - $E$  curve with huge electric polarization of BiFeO<sub>3</sub> [36].

the geometrical frustration inherent in the two-dimensional triangular lattice of Mn moments [28]. More recently, it was shown that the spin waves of this triangular lattice exhibit the hitherto unobserved magnon breakdown due to nonlinear magnon-magnon interaction [29].

## 1.2 Room temperature multiferroic BiFeO<sub>3</sub>

Whilst the study of multiferroics address many important questions of scientific interest, the key motivation behind many recent efforts has been the possible applications of this class of materials which potentially allow devices to manipulate magnetic moments by electric fields or vice versa [30]. For this purpose, however, a material which is multiferroic at room temperature or above is essential. Thus far, only BiFeO<sub>3</sub> satisfies this criterion, and over the past decade, there have been many successful realization of this possibility in the form of thin film devices [31, 32]. Another possible candidate for room temperature applications are the hexaferrites, (Ba,Sr)<sub>2</sub>(Mg,Zn)<sub>2</sub>Fe<sub>12</sub>O<sub>22</sub> [33–35], whose transitions are lower than room temperatures but exhibit noticeable magnetoelectric coupling near room temperature.

The current strong interest in BiFeO<sub>3</sub> can be traced back to two seminal works, the first of which is a thin film study [32] by the group of Ramesh, which reported a large electric polarization  $\approx 60 \mu\text{C}/\text{cm}^2$  in stark contrast to previous

studies ( $P \lesssim 10 \mu\text{C}/\text{cm}^2$ ) and also a large ferromagnetic moment  $\approx 1 \mu_B/\text{Fe}$ , both attributed to epitaxial strain effects in the thin films. Whilst the large polarization was subsequently confirmed and also found in bulk single crystals [37], the large moment was later revealed to be not intrinsic [38, 39], with the consensus being that there may be much weaker ferromagnetic moment in thin film  $\text{BiFeO}_3$  of  $\approx 0.02 \mu_B/\text{Fe}$  [40]. The second important contribution is the report by Cheong's group of a large photovoltaic effect in single crystal  $\text{BiFeO}_3$  [41], which also reported the measurement of the currently accepted intrinsic polarization  $P = 86 \mu\text{C}/\text{cm}^2$ , in line with theoretical predictions. Finally a significant driver is the recent advance in synthesis techniques which have produced large, high quality single crystals. It is especially needed for the inelastic neutron scattering measurements [42] described latter, which simply could not be carried out on the small samples previously available. For example, I show in Figure 1.3 the crystals grown by Cheong's group compared to those available before since the 1950s.

$\text{BiFeO}_3$  adopts the noncentrosymmetric  $R3c$  space group at room temperatures with a ferroelectric transition at  $T_C \simeq 1100 \text{ K}$  and an antiferromagnetic phase transition at  $T_N \simeq 640 \text{ K}$  [43–46]. From early on, the nature of the ferroelectric transition and the space group of the paraelectric phase were examined by several groups with as many as 6 proposals being put forward [47–51]. The general consensus emerging is that the paraelectric phase structure has the orthorhombic  $Pbnm$  space group symmetry. The main driving force of the ferroelectric phase transitions seems to be the stereochemical activity of the Bi 6s lone-pair, resulting in a displacement of Bi and O sublattices. However, the recent high-resolution neutron diffraction studies on high quality single crystals showed that the Fe sublattice is also displaced and gives a sizeable contribution to the total electric polarization [52].

This Fe displacement thus appears to be the natural source of the magnetoelectric coupling in this material, via the exchange-striction mechanism below the onset of the ordering of the Fe moments at  $T_N$ . The largest Fe-Fe exchange interaction is the nearest neighbour superexchange which is antiferromagnetic and leads to a simple G-type magnetic ordering [46]. In addition, there is also an antisymmetric DM interaction due to the broken inversion symmetry in the ferroelectric phase, which produces a cycloid magnetic structure with an exceptionally long period  $\approx 620 \text{ \AA}$  [53]. It is important to note that this cycloid structure causes a cancellation of a linear magnetoelectric effect but that when it is suppressed

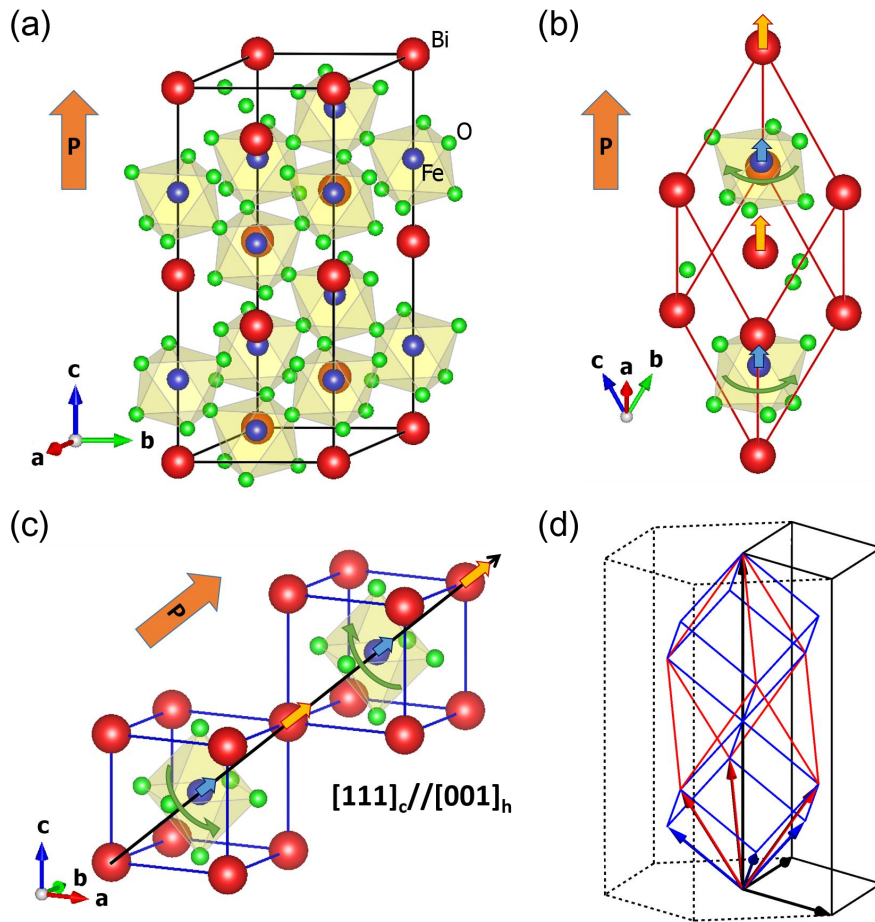


Figure 1.4: Atomic unit cells in (a) rhombohedral, (b) hexagonal and (c) pseudo-cubic notations. Yellow (light blue) arrows on the Bi (Fe) ions represent the cation shifts at the ferroelectric transition, and green arrows show the antiferro-distortive rotation of the FeO<sub>6</sub> octahedra. (d) Comparison among three notations [36].

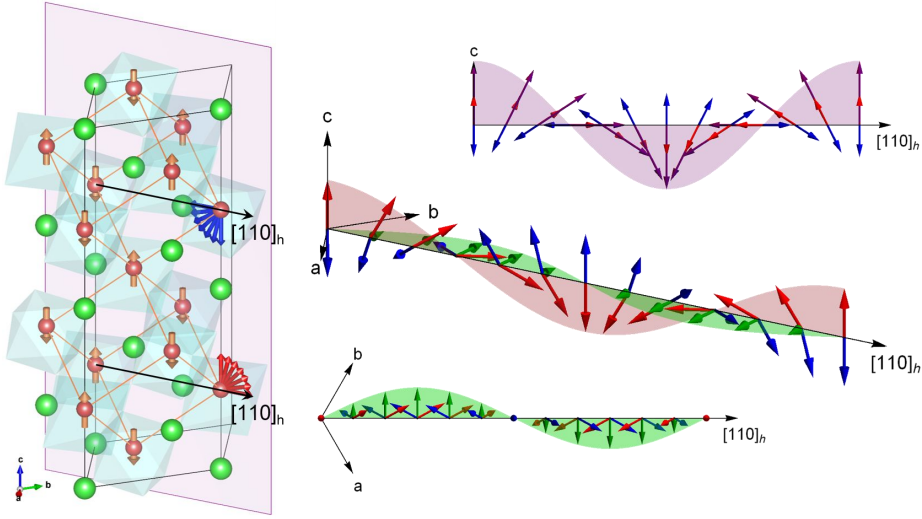


Figure 1.5: Magnetic structure of  $\text{BiFeO}_3$ . Red and blue arrows represent spins on two sublattices. Purple and green arrows denote the antiferromagnetic vector and local ferromagnetic vector, respectively. Non-collinear cycloid structure along  $[1\ 0\ 0]_h$  and spin density waves on  $ab$ -plane are shown.

by epitaxial strain or high magnetic fields, a such a linear effect ensues [54]. The presence of a single ion anisotropy (SIA) should render the cycloid anharmonic. However, neutron diffraction measurements found this to be quite small and below the detectability threshold of current instruments [55]. A further interesting aspect of the magnetic structure is a spin density wave (SDW) induced by a second effective DM vector alternating along the  $c$ -axis as seen by polarized SANS measurements [56]. However, the canting angle estimated from the SANS experiment is at least one order of magnitude larger than that obtained by fitting the spin wave spectrum measured by inelastic neutron scattering (INS), which requires further examination [57].

### 1.3 Outline of thesis

In chapter 2, I will introduce the experimental techniques, especially inelastic neutron scattering (including time-of-flight and triple-axis spectroscopy). As the experiments require large samples in order to obtain good signals, I collected several single crystals and coaligned them using the neutron diffractometer FCD,

which is also described in chapter 2. This chapter also includes details of the experiments on AMATERAS in J-PARC, MERLIN in ISIS and 4F2 in LLB.

Next, theory and calculations for spin waves dispersion are covered in chapter 3. The effective spin Hamiltonian consistent with the Landau-Ginzberg free energy is examined. In order to calculate spin waves dispersion relations for the complex non-collinear magnetic structure, a perturbative method was developed using a linear spin waves theory in a rotating frame.

In chapter 4, I will show experimental results in two parts. The high-energy spin waves were measured using TOF spectrometers. It is remarkably consistent with a G-type antiferromagnetic ordering [42]. To see the effects due to the DM interaction and SIA, the low-energy spin waves were measured below  $\approx 10$  meV using cold neutron TAS. There is rich interplay between the DM interaction and SIA to be seen in the low-energy spin waves [57]. In addition, phonon dispersion measured at a high momentum region will be compared with theoretical calculations.



## 2. Experimental techniques

Inelastic neutron scattering (INS) is arguably the only established experimental method to measure a dispersion relation of magnetic excitations. In order to measure spin waves in  $\text{BiFeO}_3$ , several experiments were conducted using two representative techniques. One is the time-of-flight (ToF) technique, and another is triple-axis (three-axis) spectrometry (TAS). Because a large amount of samples are necessary for typical inelastic neutron scattering measurement, several single crystals were coaligned to increase the effective mass. Three neutron spectrometers are introduced with some recent methods such as the repetition-rate multiplication (RRM) and sample rotation method.

### 2.1 Inelastic neutron scattering technique

#### 2.1.1 Advantages of neutron scattering

In scattering experiments, energy, momentum and spin of incident beam are changed by interacting with materials. When the change of scattered beam is measured, we can study characteristic features in target materials. In a solid, atoms and molecules form a periodic structure with a period from a few to a few tens of angstroms. To capture this structure in detail, a beam having a wavelength of a few Å is necessary. Thus we use X-ray, electron beam or neutron beam. Using neutrons is the most efficient way to study magnetic materials. Although some techniques using X-ray have been developed recently, most researches for magnetic properties are still done by neutron scattering.

While X-rays are scattered by the electron cloud around ions in a solid, neutrons are scattered by nuclei, mediated by strong nuclear force described by a Fermi potential. Moreover, neutrons interact with spins of electrons because they have spins too. The scattering cross-section of X-rays is proportional to the square of atomic number,  $Z^2$ , so it is difficult to measure light atoms like hydrogen or lithium and impossible to distinguish isotopes, which have the same atomic number but a different mass. On the other hand, because scattering cross-section of neutrons depends on isospins of nuclei, it has an advantage to measure light atoms like lithium or oxygen, and to discriminate between atoms having a similar atomic number (see figure 2.1). X-ray can be better in only limited cases that the

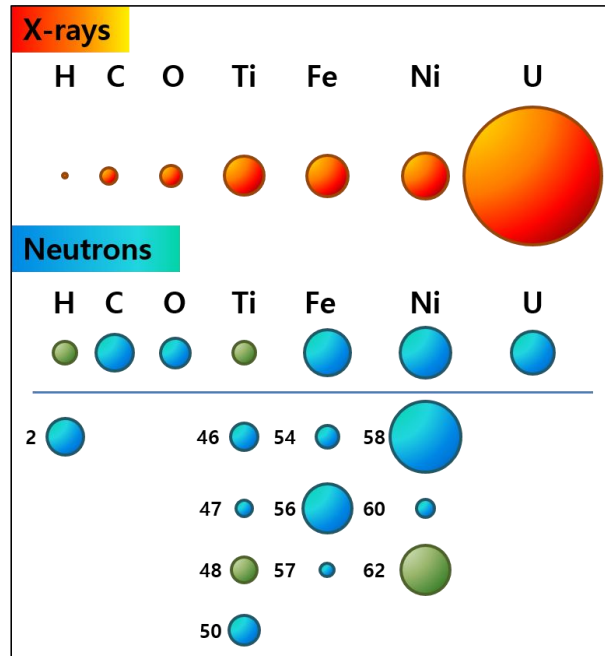


Figure 2.1: Element dependence of scattering cross-section of X-ray and neutrons [58], adapted from [59].

sample has huge neutron absorption like Gd and Ir and big enough single crystals are not available. Therefore, neutron scattering is the strongest technique to study magnetic materials with several advantages including that it can measure a spontaneous magnetization without applying an external magnetic field.

The study of the dynamics of materials has an important role in understanding many topics in condensed matter physics such as high-temperature superconductors, multiferroics, phonon-magnon interaction, quantum magnets and so on. Although there are several inelastic scattering measurements using synchrotron X-ray, inelastic neutron scattering is still used most widely for magnetic studies. One important reason is that momentum resolved measurements are possible unlike conventional optical measurements. The number of neutrons measured by inelastic neutron scattering in a small energy range at some angle from a sample can be defined as the double differential scattering cross-section, which is given by Fermi's golden rule. Another reason is that magnetic scattering cross-section is relatively higher than for photons. It also has a wide coverage in momentum and energy, as shown in figure 2.2.

The double differential scattering cross-section is closely related to the gener-

## 2.1. Inelastic neutron scattering technique

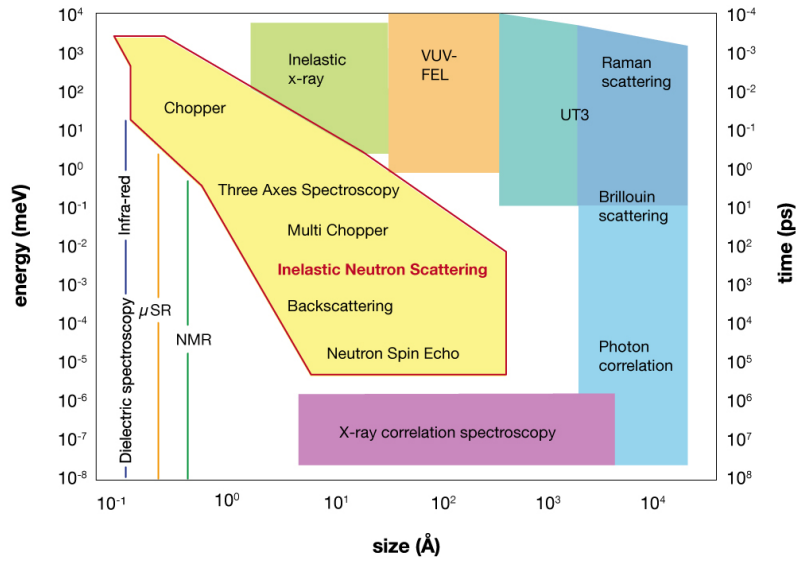


Figure 2.2: Wide length-energy coverages of inelastic neutron scattering technique compared to other investigation methods [60].

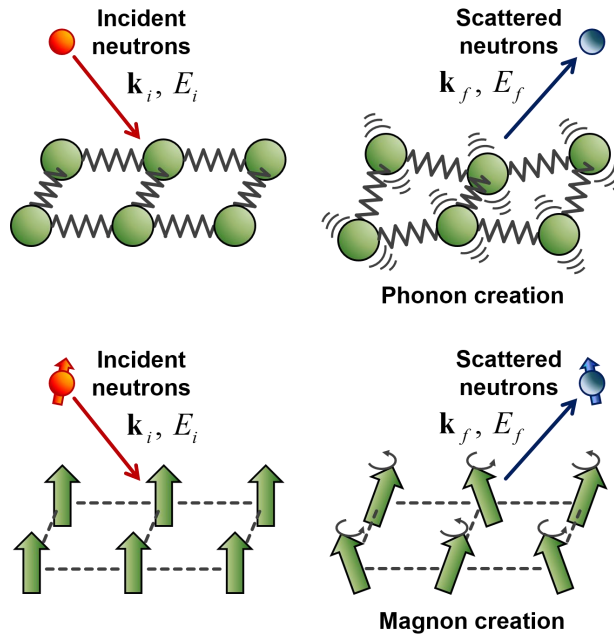


Figure 2.3: Schematics for measurement of quasi-particle excitations such as phonons and magnons using neutrons [58].

alized susceptibility, which is the Fourier transform of the pair correlation function in real space and time. A big advantage for neutron scattering is that this can be theoretically calculated. The schematics for measuring phonons or magnons are shown in figure 2.3. By measuring the difference of momentum, energy and spin between incident and scattered neutrons, momentum, energy and spin of excitations created or annihilated in materials can be determined.

### 2.1.2 Techniques for inelastic neutron scattering

There are typically four methods for inelastic neutron scattering (INS): triple-axis (or three-axis, TAS), time-of-flight (ToF), backscattering and spin-echo spectrometries (or spectroscopies), and each is suited to a particular type of measurement. In the first three (TAS, ToF, backscattering), the neutron counts detected is proportional to the scattering function in energy and reciprocal space  $S(\mathbf{Q}, \omega)$  which is also related to the imaginary part of the dynamical susceptibility. The last technique (spin-echo spectroscopy) measures the time-transformed scattering function  $S(\mathbf{Q}, \tau)$  by an indirect method and will not be discussed in detail.

The conservation of energy and momentum is required in the scattering process,

$$\mathbf{Q} = \mathbf{k}_i - \mathbf{k}_f \quad (2.1)$$

$$\hbar\omega = E_i - E_f = \frac{\hbar^2}{2m_n} (k_i^2 - k_f^2) \quad (2.2)$$

so the neutron trajectory is restricted. All INS methods rely on fixing either one of  $\mathbf{k}_i$  or  $\mathbf{k}_f$  and detecting the other by measuring the energy (directly in TAS, or as the time-of-flight) and direction of the neutron after scattering.

In the ToF method, neutrons are thought of as particles with energy given by their speed. If  $\mathbf{k}_i$  is fixed, it is called direct geometry. If  $\mathbf{k}_f$  is fixed, it is indirect geometry. In direct geometry, a chopper selects neutrons with one velocity (or energy) at one time. This pulse of neutrons is then scattered from the sample in different directions to be detected in a large area detector at different angles. If the neutrons lose energy to the sample, they will slow and be detected later than the expected pulse, as shown by  $t_{\text{det}}$  and  $t_{\text{exp}}$  in figure 2.4. If they gain energy from the sample, they will be detected faster. The angle of the detector determines  $\mathbf{Q}$  as shown in figure 2.4. Due to equations 2.1 and 2.2  $E$  and  $\mathbf{Q}$  are related as described in section 2.2.

Time-of-flight scattering can be performed at either a research reactor or a

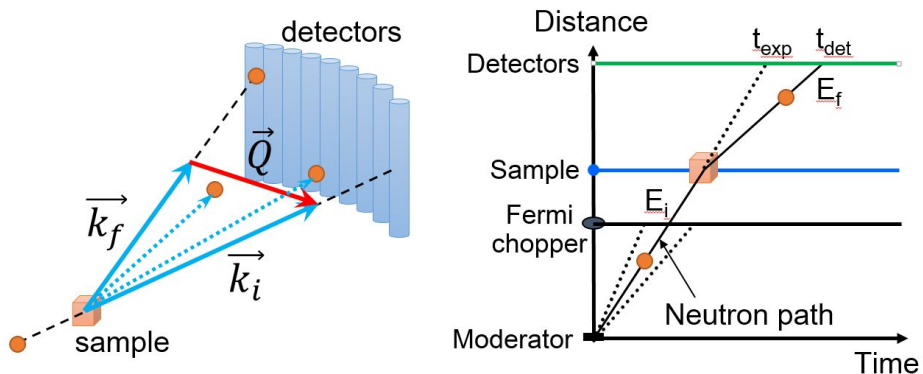


Figure 2.4: Configuration and schematics for time-of-flight technique. Momentum and energy transfer of the scattered neutrons are measured by flight time.

spallation source. If a reactor is used, more than one chopper is needed to create a pulse, but a spallation source naturally creates pulses. In this thesis, I have used the direct geometry spectrometers AMATERAS at J-PARC and MERLIN at ISIS which are both spallation sources, as described in sections 2.3.2 and 2.3.3.

Triple-axis spectrometry (or three-axis spectroscopy, TAS) measures the energy of the neutron by using monochromator and analyser crystals using Bragg scattering. The Bragg law is

$$n\lambda = 2d \sin \theta \quad (2.3)$$

so the neutron energy ( $E = 4\pi^2\hbar^2/2m_n\lambda$ ) changes with the angle  $\theta$  of a monochromator crystal with lattice spacing  $d$ . The three-axis spectrometer has arms which rotate around the three axes of the monochromator ( $2\theta_M$ ), sample ( $2\theta_S$ ) and analyser ( $2\theta_A$ ) to measure the initial energy ( $E_i$  from  $2\theta_M$ ), final energy ( $E_f$  from  $2\theta_A$ ) and momentum in the scattering plane ( $\mathbf{Q}$  from  $\theta_S$  and  $2\theta_S$ ), as shown in figure 2.5. The three axes allows measurement of the scattering function at any point in energy and momentum space physically accessible by the spectrometer. This makes TAS the most flexible INS method, but it does not give a good overview of dispersion like the ToF method. In this thesis, I have used the spectrometers 4F2 and 1T1 at LLB, as described in section 2.3.4.

The triple-axis spectrometry method was first developed by Bertram Brockhouse at the National Research Experimental NRX reactor at the Chalk River Laboratories in Canada. The first results from the prototype triple-axis spectrometer were published in January 1955 and the first true triple-axis spectrometer was built in 1956. B. Brockhouse shared the 1994 Nobel prize with C. Shull for

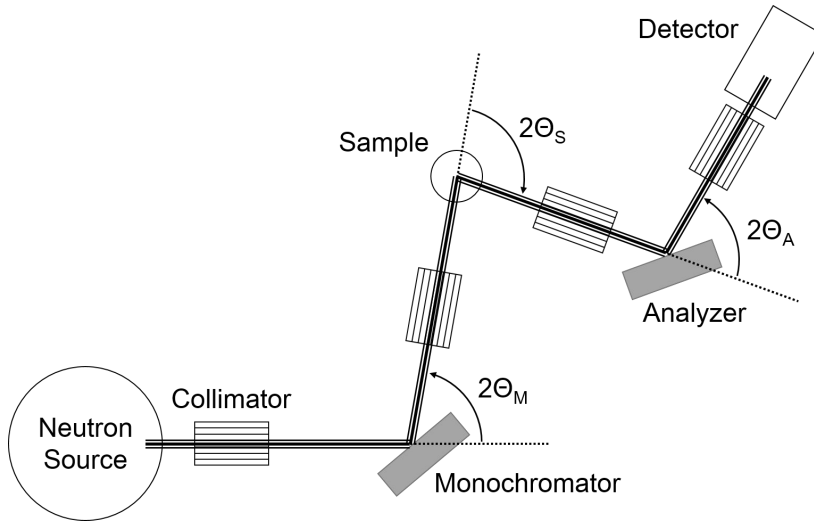


Figure 2.5: Schematics for neutron triple-axis spectrometry. Momentum and energy transfer of the scattered neutrons are measured by three scattering angles.

Physics for this development, “for pioneering contributions to the development of neutron scattering techniques for studies of condensed matter” and “for the development of neutron spectroscopy”.

Neutron backscattering is similar to TAS as it uses crystals to fix the neutron energy. The crystals are set so neutrons are backscattered ( $2\theta_{M,A} \approx 180^\circ$ ) so the energy resolution is very good, in the order of  $\mu\text{eV}$ . Because the monochromator and analyser cannot be rotated as in TAS, the neutron energy has to be changed by changing  $d$  in equation 2.3. This is done by using different crystals for large energy transfer. Very small energy transfer can be measured by thermal expansion of the monochromator or analyser crystals or by rotating them around the axis of the neutron beam to change the neutron speed by Doppler shift. So, it is not as flexible as TAS, but has better energy resolution.

Neutron spin echo spectroscopy is an inelastic neutron scattering technique invented by Ferenc Mezei in the 1970s, and developed in collaboration with John Hayter. In recognition of his work and in other areas, Mezei was awarded the first Walter Haelg Prize in 1999. Unlike other methods above, spin echo spectroscopy is an interferometry method which measures the time Fourier transform of  $S(\mathbf{Q}, \omega)$ ,  $S(\mathbf{Q}, \tau)$  instead of the scattering function directly. It does this by using polarised neutrons precessing in a constant magnetic field. The polarisation direction of the neutron is then dependent on their speed, because faster neutrons will have

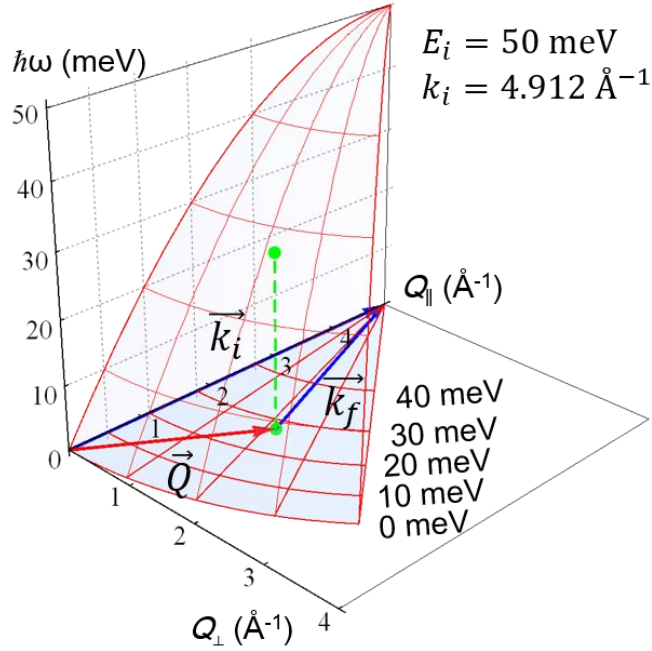


Figure 2.6: Detector trajectory on momentum-energy space. Umbrella-shaped curved surface can be measured by a single scan with a fixed sample.

less time in the field and precesses less. The strength of the magnetic field or its length can be changed to measure the maximum polarisation, and this is used to indirectly find the neutron speed. The technique can measure quasielastic signals with resolution in order of neV, or dispersive excitations with  $\mu\text{eV}$  resolution in resonant spin echo spectroscopy.

## 2.2 Detector trajectory in ToF measurement

In a direct geometry ToF spectrometer, neutrons are detected in a detector at a fixed position given by the angles  $(\theta, \phi)$  at a time from which their energy  $\hbar\omega$  can be determined. Equations 2.1 and 2.2 means that the momentum transfer

magnitude is fixed by the energy transfer as

$$\begin{aligned}
 |\mathbf{Q}|^2 &= |\mathbf{k}_i|^2 + |\mathbf{k}_f|^2 - 2\mathbf{k}_i \cdot \mathbf{k}_f \\
 &= 2 \left( |\mathbf{k}_i|^2 - \frac{m_n \omega}{\hbar} \right) - 2\mathbf{k}_i \cdot \mathbf{k}_f \\
 &= 2 \left( |\mathbf{k}_i|^2 - \frac{m_n \omega}{\hbar} \right) - 2|\mathbf{k}_i| \sqrt{|\mathbf{k}_i|^2 - 2\frac{m_n \omega}{\hbar}} \\
 &\quad \times (\sin \theta_i \sin \theta_f \cos(\phi_i - \phi_f) + \cos \theta_i \cos \theta_f)
 \end{aligned} \tag{2.4}$$

where  $\theta$  is the polar angle and  $\phi$  is the azimuthal angle. So, when  $\mathbf{k}_i$  is fixed, the energy transfer  $\omega$  follows a line through detector-space  $(\theta_f, \phi_f)$  called a detector trajectory, which is approximately a cosine in the scattering angle  $\cos(\phi_i - \phi_f)$  at a fixed detector elevation as shown in figure 2.6. I here assume horizontal detector array from 0 to 45 degrees with respect to the incident beam. This trajectory is modified when the sample is rotated, changing  $(\theta_i, \phi_i)$ , as discussed in section 2.3.3. The envelope of the cosine is dependent on  $E_i \propto |\mathbf{k}_i|^2$ , as shown in figure 2.6 in the  $Q_{\perp}$ - $Q_{\parallel}$  plane.

### 2.2.1 Measurement for 1- and 2-dimensional systems

It is easy to measure a dispersion in 1-dimensional systems. Regardless of the momentum perpendicular to the major chain axis, spin waves dispersion has the same information,  $S(q, E)$ . Thus it can be measured with a simple detector trajectory because it always intersects with spin waves as shown in figure 2.7. By putting the chain direction of the sample perpendicular to the incident beam, i.e.,  $k_i \perp Q_{chain}$ , the full dispersion can be projected onto the  $Q_{chain}$ - $E$  plane.

In 2-dimensional systems, it is still simple to measure a dispersion using the typical detector trajectory. Full information of excitations is 3-dimensional: 2-dimensional momentum space of interest and energy. Because the dispersion does not have  $Q_z$  dependence, full 3-dimensional information can be easily determined by combining several constant- $Q_z$  plane when the incident beam is perpendicular to the plane of interest, as shown in figure 2.8.

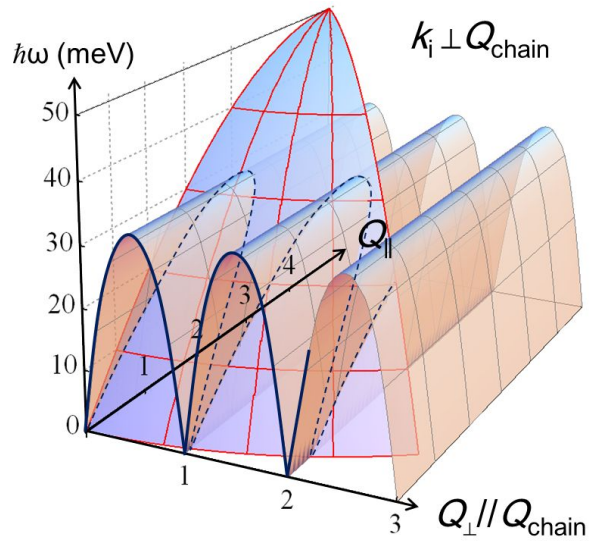


Figure 2.7: Schematics to measure excitations in 1-dimensional systems using the ToF method.

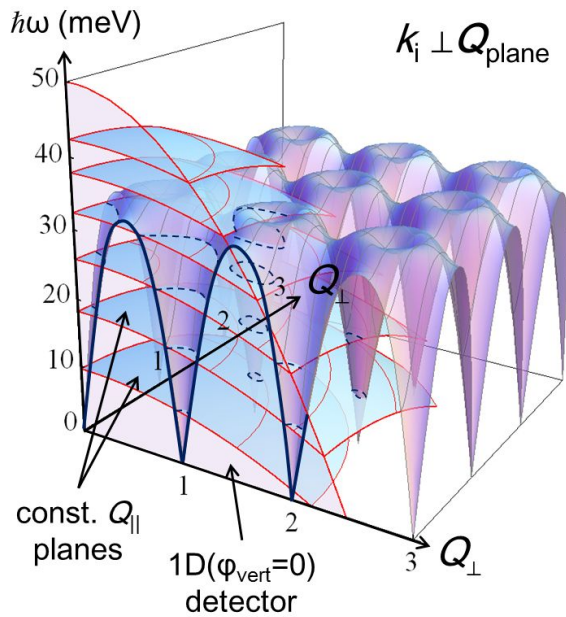


Figure 2.8: Schematics to measure excitations in 2-dimensional systems using the ToF method.

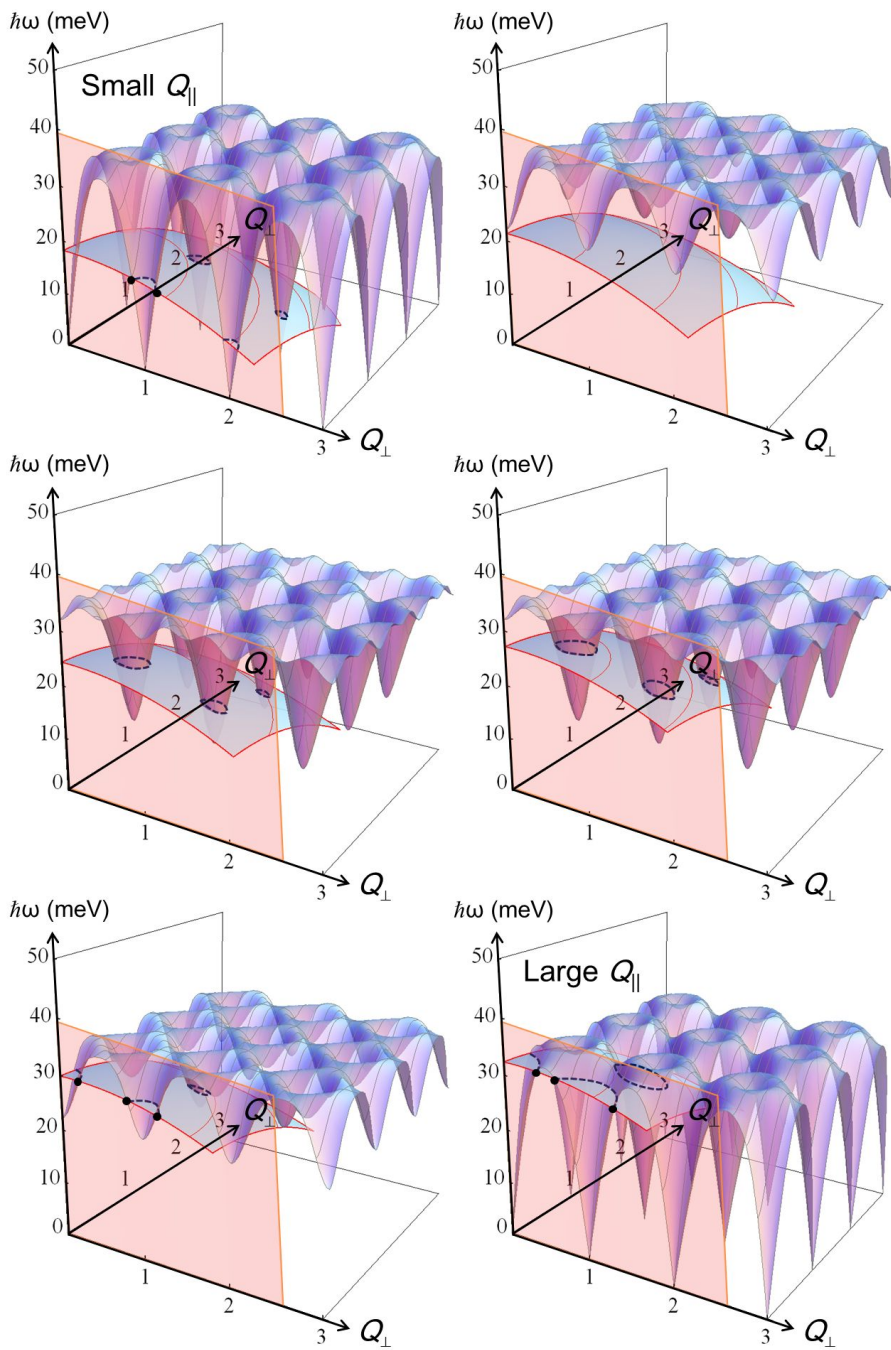


Figure 2.9: Schematics to measure excitations in 3-dimensional systems.

### 2.2.2 Measurement for 3-dimensional systems

However, it becomes more difficult for 3-dimensional systems. For each constant- $Q_z$  plane with a different momentum, it shows a different dispersion (see figure 2.9), so it is impossible to measure 4-dimensional information by a single-shot measurement. Thus we need to collect a number of datasets by rotating the sample or changing the incident energy, which will be covered in section 2.3.3, for the full 4-dimensional  $S(\mathbf{q}, \omega)$ .

## 2.3 Single crystal experiments on AMATERAS, MERLIN and 4F2

Although INS is the best way to measure spin waves, it is necessary to prepare a big amount of samples for INS. Single crystals with a mass from a few hundred milligrams to several grams are typically demanded. Since a big single crystal of  $\text{BiFeO}_3$  synthesized recently was not heavy enough, I coaligned several single crystals to increase a total mass of samples. Ten single crystals with a total mass of about 1.8 g were coaligned along 3 directions within 2 degrees using the neutron four circle diffractometer (FCD) at HANARO in Korea.

I have carried out high resolution inelastic neutron scattering experiments with two time-of-flight spectrometers: one is AMATERAS at J-PARC in Japan and another MERLIN at ISIS in UK. All experiments were done at 5 K. For technical reasons discussed below, data taken at AMATERAS are useful especially for the low energy part of the spin waves whilst the detailed features of the high energy part of the spin waves are clearer in the data taken at MERLIN.

### 2.3.1 Coalignment of single crystals

The FCD is a neutron four-circle diffractometer (figure 2.10) at High-flux Advanced Neutron Application Reactor (HANARO) in Korea Atomic Energy Research Institute (KAERI). It is designed for nuclear and magnetic structure analysis on single crystals by measuring intensities of several thousand diffraction spots with four angles:  $\phi$ ,  $\chi$  and  $\omega$  in space and diffraction angle  $2\theta$ .

I used this to coalign several pieces of  $\text{BiFeO}_3$  single crystals. Ten single crystals, each with a mass of about 100–500 mg, were attached on the top of a aluminum plate holder (figure 2.11) using a mixture of cyanoacrylates (instant



Figure 2.10: Neutron four-circle diffractometer FCD at HANARO in Daejeon, Korea.

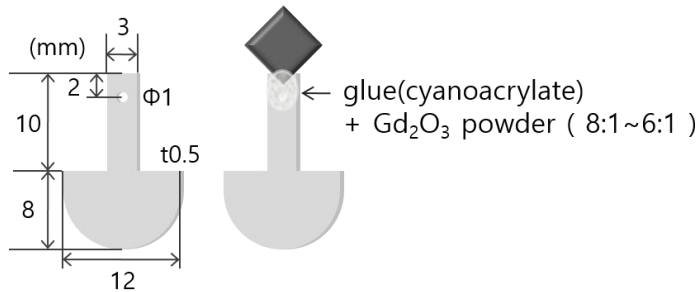


Figure 2.11: Desing for sample holders and assembly plate. A round bottom of the holder was designed for tilting the sample easily on the assembly plate.

glue) and  $Gd_2O_3$  powders with a ratio of 8:1 to 6:1.  $Gd_2O_3$  was used in order to reduce possible backgrounds from hydrogen atoms in the glue. Each single crystal was measured to find out the crystallographic directions on the scattering plane,  $b^*-c^*$ . Using the aluminum plate holder, each crystal was adjusted to have the same direction with respect to the collecting plate.

Then, adding crystals one by one from the smallest one, I checked the mosaicity along three major directions:  $[0\ 1\ 2]_h$ ,  $[0\ 0\ 6]_h$  and  $[0\ 3\ 0]_h$ . Every crystal was carefully aligned by sliding, tilting and twisting of the sample plate. Considering a typical beam size of neutron spectrometers, ten crystals were collected within a width of 20 mm and a height of 10 mm as shown in figure 2.12.

Finally, 10 crystals were coaligned within 2 degrees horizontally as shown in figure 2.13. I note that two or three peaks appear for two other directions even if they show almost one peak for  $(0, 1, 2)$ . This can originate from a slight distortion

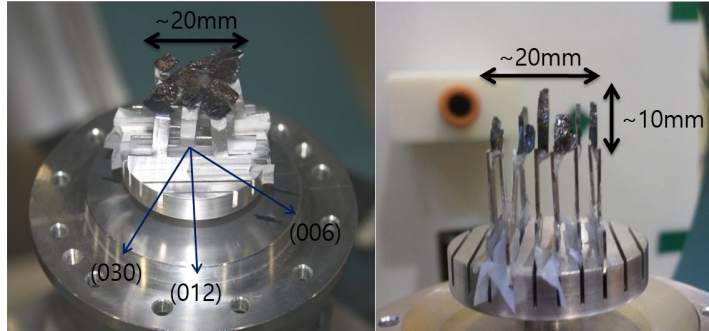


Figure 2.12: Full assembly of ten single crystals accumulated within a width of 20 mm and a height of 10 mm.

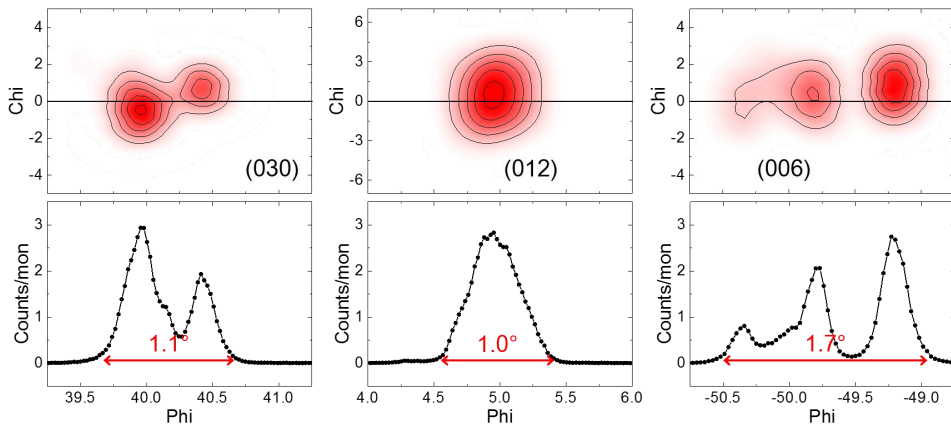


Figure 2.13: Final mosaicity results along three major directions:  $[0\ 1\ 2]_h$ ,  $[0\ 0\ 6]_h$  and  $[0\ 3\ 0]_h$ .

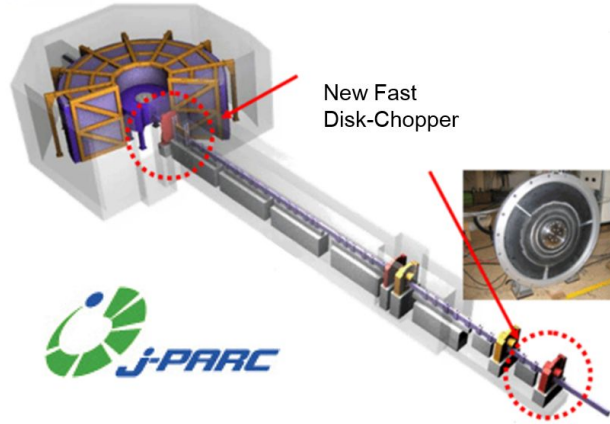


Figure 2.14: ToF spectrometer AMATERAS at J-PARC in Tokai, Japan.

of crystal structure or twins. Although it caused a little difficulty to determine the exact direction when the sample was mounted on spectrometers, there was no problem in determining spin waves due to relatively low instrumental resolution.

### 2.3.2 ToF spectrometer AMATERAS with fixed geometry

AMATERAS is a cold-neutron disk-chopper spectrometer in the Japan Proton Accelerator Research Complex (J-PARC). It is focused to detect dynamical properties in atomic, molecular and magnetic systems in a relatively low-energy range with high resolution. The incident energy can be chosen in  $1 < E_i < 80$  meV typically, and it has wide detector banks of 5–110 degrees horizontally and -16–23 degrees vertically. The resolution  $\Delta E/E_i$  is quite good, a minimum  $\approx 1\%$  at  $E_i < 3$  meV and  $\approx 4\text{--}5\%$  even at  $E_i < 80$  meV.

I carried out the AMATERAS experiment with fixed geometries: incident neutron beam parallel to the  $[0\ 0\ 1]_h$  ( $c^*$ ) or  $[1\ 2\ 0]_h$  ( $b^*$ ) axes with the incident energy of 94.154 meV. Thanks to the so-called repetition rate multiplication (RRM) technique [61], I was also able to have additional data for several other incident energies such as 23.630 and 10.513 meV. In order to determine spin waves from the AMATERAS data, I had to search through the data to determine the energy of the spin waves at  $q$  points concerned, which are covered by the experiment. In this configuration, the detector trajectories are shown in figure 2.15.

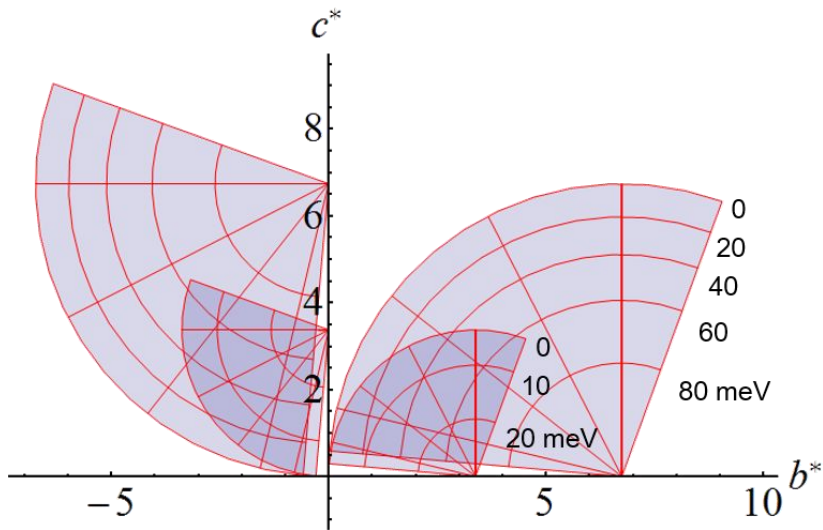


Figure 2.15: Detector coverage in the AMATERAS experiment with detector banks of 5–110 degrees horizontally. Incident neutron beam was parallel to the  $c^*$  or  $b^*$  axes with the incident energy of 94.154 meV.

### 2.3.3 ToF spectrometer MERLIN with the sample rotation method

MERLIN is a high count rate, medium energy resolution, direct geometry chopper spectrometer. It was designed to be a high intensity, medium energy resolution spectrometer that would complement the high-resolution MAPS spectrometer, and replace the HET spectrometer. MERLIN's design exploited recent advances in technology with a supermirror guide to enhance flux, as well as 3 m long position-sensitive detectors in vacuum, making it ideal for the study of single crystals. The detector bank covers a massive  $\pi$  steradians of solid angle with an angular range from  $-45^\circ$  to  $135^\circ$  in the horizontal plane, and  $\pm 30^\circ$  in the vertical plane. This allows a large coverage of  $Q$ - $\omega$  space to be accessed in a single run. Since 2014, Merlin has been running in event mode, and by using the new Gd chopper combined with a disk chopper, it is able to run in repetition-rate multiplication (RRM) mode, allowing users to simultaneously measure with several incident energies.

In order to overcome the technical difficulty with the traditional method in the AMATERAS experiment, the measurement was performed while rotating the samples from  $-90$  to  $+80$  degrees with the incident beam parallel to the

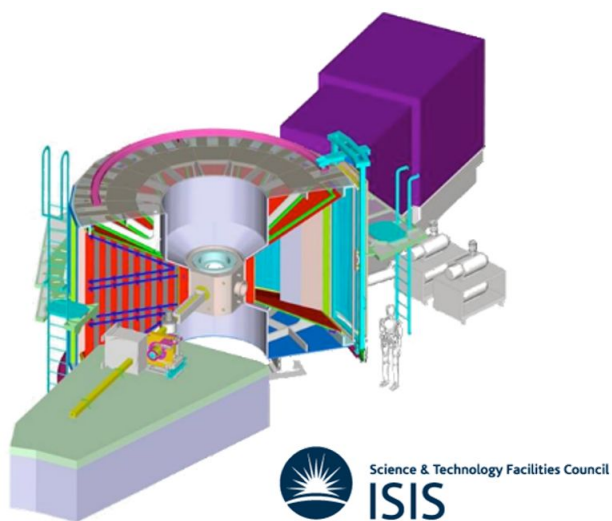


Figure 2.16: ToF spectrometer MERLIN beamline at ISIS in UK.

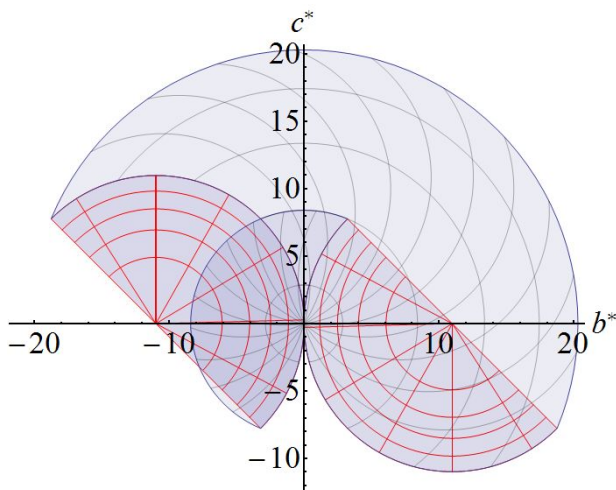


Figure 2.17: Detector coverage with sample rotation from  $-90$  to  $+80$  degrees with the scattering plane on  $b^*$ - $c^*$  plane.

[0 0 1] direction initially: the scattering plane is on the  $b^*$ - $c^*$  plane. After the experiments, I combined all the 171 individual data files to make a single file containing the full four dimensional information of momentum and energy of the spin waves. The incident energy of 250 meV was chosen to make the detector coverage wide enough to cover the full Brillouin zone of the anticipated spin waves of BiFeO<sub>3</sub> as shown in figure 2.17, in particular the high energy parts whose detailed features are missing in the AMATERAS data. With this configuration and the sample rotation method, I was able to cover the full Brillouin zone of BiFeO<sub>3</sub> and project the spin waves with an energy transfer higher than 30 meV for any directions of the Brillouin zone. The final data in the four-dimensional  $q$ - $E$  space is crucial to determine exchange interactions precisely.

### 2.3.4 Cold-neutron triple-axis spectrometer 4F2

The TAS method is described in section 2.1.2. 4F2 uses pyrolytic graphite (PG) as monochromators and analysers, providing wavelengths between 6 and 2 Å ( $1.05 < k_i < 2.7 \text{ \AA}^{-1}$ ,  $2.3 < E_i < 15.1 \text{ meV}$ ), and is designed for measuring low energy dispersive excitations, with  $\hbar\omega < 4 \text{ meV}$ . It has a double monochromator so the incident beam direction does not need to be rotated to obtain different energy incident neutrons. The neutron background is also reduced. The monochromator has a computer-controlled vertical focusing, and many possible collimators are available: 60', 30', or 15' before or 60', 40', 20', or 10' after the monochromators and an optional 25' or 15' can be added between the two monochromators.

The pyrolytic graphite analyzer is normally used in a horizontally focusing geometry. In this mode, the curvature of the analyzer is controlled by the computer, and the collimators (60', 40', 20', 10') are replaced by wedge-shaped tunnels. The sample table is equipped with two orthogonal non-magnetic goniometers, allowing tilts of  $\pm 20^\circ$ . Their upper face (serving as a support for the various sample environments) is located 270 mm below the axis of the beam. The sample-to-monochromator and sample-to-analyzer distances can be adjusted to accommodate various sample environments.

In the experiments on BiFeO<sub>3</sub>, 4F2 was operated in two configurations: 1) with fixed  $k_f = 1.55 \text{ \AA}^{-1}$  ( $E_f = 4.97 \text{ meV}$ ) and 2)  $k_f = 1.2 \text{ \AA}^{-1}$  ( $E_f = 2.98 \text{ meV}$ ) with open collimation and focused monochromators and analyzers. The sample assembly was sealed with helium gas as a heat-exchange gas in the aluminum sample can and cooled down to 15 K using the liquid helium cryostat.

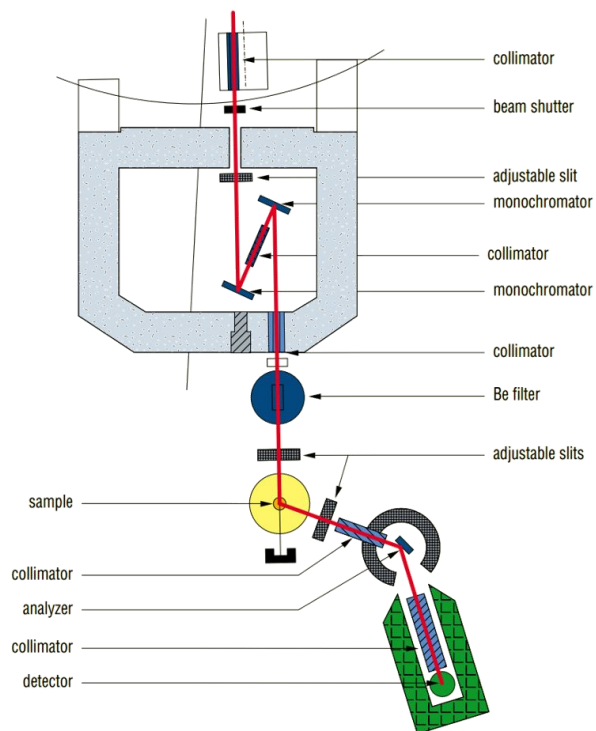


Figure 2.18: Cold neutron TAS, 4F2 beamline at LLB in France

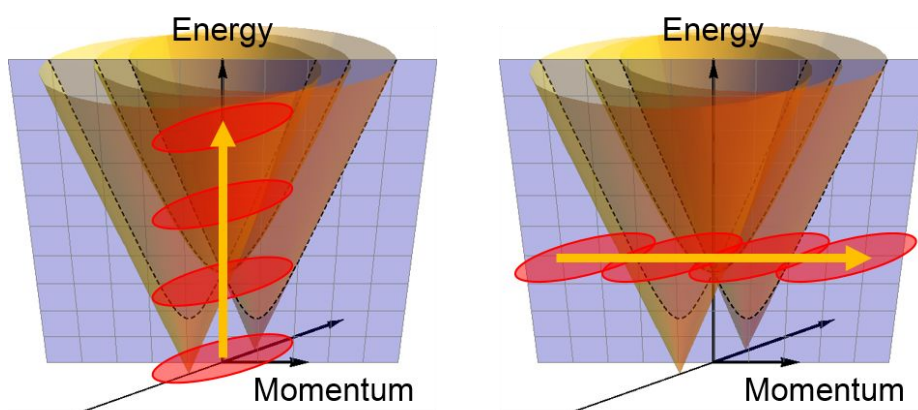


Figure 2.19: Scanning with resolution ellipsoid. Schematics for constant-momentum and constant-energy scans.

Figure 2.19 shows schematics of constant-momentum and constant-energy measurements respectively. The resolution ellipsoid is defined by the incident beam divergence, collimator transmission functions and the mosaic distributions of the monochromator and the analyzer crystals. By moving this ellipsoid in the momentum-energy space, dispersive excitations are detected. It is important in practice to optimize the orientation of the resolution ellipsoid such that the two longer axes are parallel to the dispersion surface. In this “focused” condition, the measured width of the dispersion is small. The measurement was done while considering this condition to improve momentum and energy resolutions.



## 3. Spin waves calculations

### 3.1 Effective spin Hamiltonian

#### 3.1.1 Landau-Ginzberg free energy

The crystal and magnetic symmetries of the structure of a material constrains its physical properties. This can be used to construct phenomenological models of these properties based on the Landau theory of phase transitions. On the basis of this approach, a variety of unusual effects, such as the Dzyaloshinskii-Moriya interaction, weak ferromagnetism, the linear magnetoelectric effect and so on, were discovered in past century. Kadomtseva *et al.* analyzed the magnetoelectric properties of BiFeO<sub>3</sub>, starting from the space group  $R\bar{3}c$  as a parent symmetry for  $R3c$  symmetry. Following their analysis, one can find several invariant terms that correspond to the irreducible representations and are responsible for the weak ferromagnetism, linear ME effect and inhomogeneous ME interaction [62].

Finally, the usual expression for the Landau-Ginzburg free energy describing BiFeO<sub>3</sub> can be written in the following form:

$$f_l = \int d\mathbf{r} A(\nabla\mathbf{l})^2 + \lambda\mathbf{l}^2 + G\mathbf{l}^4 - \alpha\mathbf{P} \cdot [\mathbf{l}(\nabla \cdot \mathbf{l}) + \mathbf{l} \times (\nabla \times \mathbf{l})] - 2\beta M_0 \mathbf{P} \cdot (\mathbf{m} \times \mathbf{l}) - K_u l_c^2 \quad (3.1)$$

where  $M_0$  is the magnitude of the magnetization vector  $\mathbf{M}_i$  of sublattices,  $\mathbf{P}$  is the spontaneous polarization vector, and  $\mathbf{m} = (\mathbf{M}_1 + \mathbf{M}_2)/2M_0$  and  $\mathbf{l} = (\mathbf{M}_1 - \mathbf{M}_2)/2M_0$  are the magnetization and antiferromagnetic unit vectors, respectively. The first three terms denote the exchange interactions; the fourth term is the Lifshitz invariant which results in the cycloid, the fifth term is the Dzyaloshinskii-Moriya-like invariant which gives a weak ferromagnetism [62], and both terms are related to the microscopic Dzyaloshinskii-Moriya interaction [63]; the sixth term is the single ion anisotropy. I will discuss the microscopic spin Hamiltonian corresponding to the L-G free energy in the following section.

#### 3.1.2 Microscopic spin Hamiltonian

The magnetic excitations are mostly easily calculated using a microscopic spin Hamiltonian in linear spin wave theory [42, 64–67]. The form of the Hamiltonian

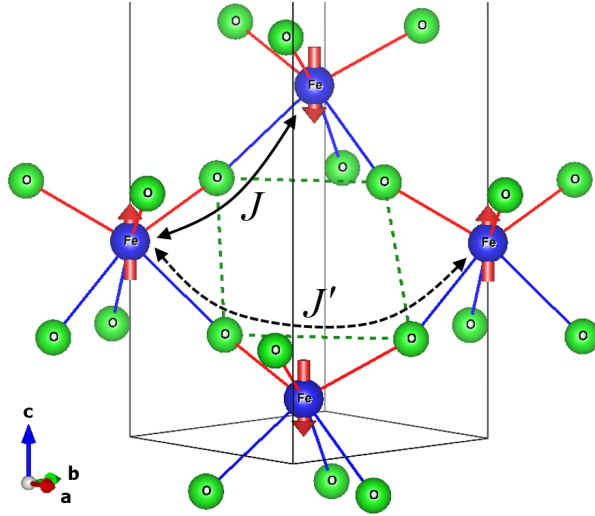


Figure 3.1: The Fe–O–Fe and Fe–O–O–Fe paths for the superexchange interaction between the NN and NNN in the distorted FeO<sub>6</sub> octahedra. Red and blue lines represent a short and long Fe–O bond, respectively [36].

most commonly used for BiFeO<sub>3</sub> is

$$\mathcal{H} = \mathcal{J} \sum_{\mathbf{r}, \alpha} \mathbf{S}_{\mathbf{r}} \cdot \mathbf{S}_{\mathbf{r}+\alpha} + \mathcal{J}' \sum_{\mathbf{r}, \beta} \mathbf{S}_{\mathbf{r}} \cdot \mathbf{S}_{\mathbf{r}+\beta} - \mathcal{D}_u \sum_{\mathbf{r}} \hat{\mathbf{u}} \cdot (\mathbf{S}_{\mathbf{r}} \times \mathbf{S}_{\mathbf{r}+a\hat{\mathbf{v}}}) - \mathcal{D}_c \sum_{\mathbf{r}} (-1)^{6\mathbf{r} \cdot \hat{\mathbf{c}}/c} \hat{\mathbf{c}} \cdot (\mathbf{S}_{\mathbf{r}} \times \mathbf{S}_{\mathbf{r}+\frac{c}{2}\hat{\mathbf{c}}}) - \mathcal{K} \sum_{\mathbf{r}} (\mathbf{S}_{\mathbf{r}} \cdot \hat{\mathbf{c}})^2, \quad (3.2)$$

where  $\alpha$  and  $\beta$  refer respectively to nearest and next-nearest neighbour iron atoms, and  $\mathbf{u}$ ,  $\mathbf{v}$  and  $\mathbf{c}$  refer to the Cartesian directions which defines the cycloid with the propagation direction along  $\mathbf{v}||[1\bar{1}0]_{\text{pc}}$  (in pseudocubic (pc) notation,  $[110]_{\text{hex}}$  in hexagonal notation), and the moment initially align parallel or antiparallel to  $\mathbf{c}||[111]_{\text{pc}}$  ( $[001]_{\text{hex}}$ ). The first and second terms are the diagonal Heisenberg exchange interactions (see figure 3.1), the third and fourth are the antisymmetric Dzyaloshinskii-Moriya (DM) exchange terms, and the final terms is the (easy-axis) single ion anisotropy.

The equivalence of the parameters  $\mathcal{J}$ ,  $\mathcal{D}_u$  and  $\mathcal{K}$  in the spin Hamiltonian (3.2) with  $A$ ,  $\lambda$ ,  $\alpha$  and  $K_u$  in the free energy (3.1) may be determined by equating the ground state energy obtained for particular configurations (such as a collinear AFM, harmonic or anharmonic cycloid structure) given by the two approaches

as detailed in Appendix B and are given by,

$$\lambda = \frac{6S^2}{V} (-3\mathcal{J} + 6\mathcal{J}') \quad (3.3)$$

$$A = \frac{6S^2}{V} a_{hex}^2 \left( \frac{\mathcal{J} - 4\mathcal{J}'}{4} \right) \quad (3.4)$$

$$\alpha = \frac{6S^2}{V} \frac{1}{P_s} a_{hex} \mathcal{D}_u \quad (3.5)$$

$$\beta = \frac{6S^2}{V} \frac{1}{M_0 P_s} \mathcal{D}_c \quad (3.6)$$

$$K_u = \frac{6S^2}{V} \mathcal{K}, \quad (3.7)$$

where  $V$  is the volume of the hexagonal unit cell with six Fe ions and  $P_s$  is the saturated ferroelectric polarization.

### 3.1.3 DM interaction and single-ion anisotropy

The DM interaction arises from the spin-orbit coupling which permits spin-flip hopping between neighbouring ions that leads, in a second order perturbation theory, to the antisymmetric exchange term  $\mathbf{D}_{ij} \cdot (\mathbf{S}_i \times \mathbf{S}_j)$  [6]. The  $\mathbf{D}$  coefficient is only non-zero when the mid-point between spins  $\mathbf{S}_i$  and  $\mathbf{S}_j$  is not at an inversion centre. This is satisfied in BiFeO<sub>3</sub> below the ferroelectric transition due to the ferroelectric distortion which causes a displacement of the oxygen ligand in the Fe-O-Fe bond. The DM interaction tends to cause neighbouring spins to align perpendicular to each other, and thus competes with the exchange interaction which favours their (anti-)parallel alignment, the result often being either a canting of the spins, or in the case of BiFeO<sub>3</sub> a long range cycloid.

In BiFeO<sub>3</sub>, the DM interaction between the nearest neighbours can be described by two effective DM terms, though the summation of the DM vectors is along the  $c$ -axis due to the 3-fold symmetry of the  $R3c$  crystal structure. As shown in figure 3.2, the DM interaction can be effectively rewritten as

$$\begin{aligned} \mathcal{H}_{\text{DM}} &= - \sum_{\mathbf{r}, \Delta} \mathbf{D}_{\Delta} \cdot (\mathbf{S}_{\mathbf{r}} \times \mathbf{S}_{\mathbf{r}+\Delta}) \\ &= - \sum_{\mathbf{r}} \mathbf{D}_u \cdot (\mathbf{S}_{\mathbf{r}} \times \mathbf{S}_{\mathbf{r}+a\hat{v}}) - \sum_{\mathbf{r}} \mathbf{D}_c \cdot \left( \mathbf{S}_{\mathbf{r}} \times \mathbf{S}_{\mathbf{r}+\frac{c}{2}\hat{c}} \right) \end{aligned} \quad (3.8)$$

with  $\mathbf{D}_u = \mathcal{D}_u \hat{\mathbf{u}}$  working between the next nearest neighbors along  $v$ -axis and

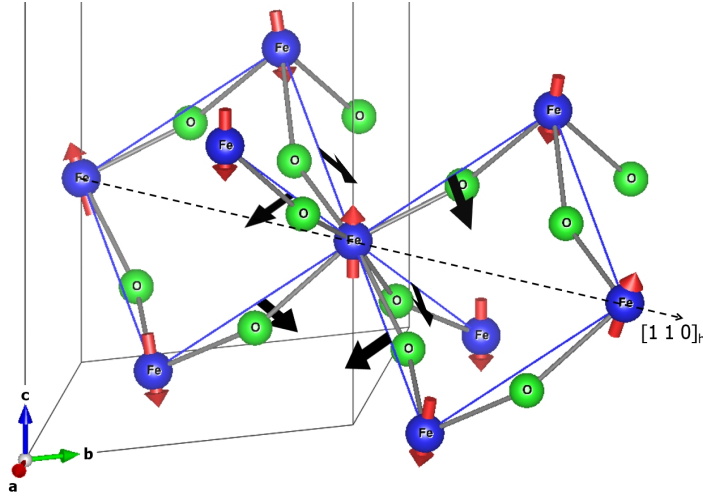


Figure 3.2: The DM vectors (black arrows) for nearest neighbors on distorted octahedra and part of the spin cycloid (red arrows). The net effect of the DM interaction can be described by two effective DM vectors along two directions perpendicular to the cycloid direction [36].

$\mathbf{D}_c = \mathcal{D}_c(-1)^{\frac{6r-c}{c}} \hat{\mathbf{c}}$  working alternately on different layers along the  $c$ -axis, where  $\hat{\mathbf{u}}$ ,  $\hat{\mathbf{v}}$  and  $\hat{\mathbf{c}}$  are the unit vectors along  $[1 \bar{1} 0]_{\text{hex}}$ ,  $[1 1 0]_{\text{hex}}$  and  $[0 0 1]_{\text{hex}}$ , respectively. The first term mainly produces the spin cycloid structure [53] propagating along the  $v$ -axis on the  $vc$ -plane, and the second term produces a spin density wave perpendicular to the cycloid plane [56]. The latter also induces weak ferromagnetism by canting the spins in the  $uv$ -plane when the spin cycloid is suppressed.

The single ion anisotropy Hamiltonian is given by

$$\mathcal{H}_{\text{SIA}} = -\mathcal{K} \sum_{\mathbf{r}} (\mathbf{S}_{\mathbf{r}} \cdot \hat{\mathbf{c}})^2, \quad (3.9)$$

where the sign of  $\mathcal{K}$  determines whether it is of an easy-axis ( $\mathcal{K} > 0$ ) or easy-plane ( $\mathcal{K} < 0$ ) form. While the DM interaction is due mainly to the spin orbit coupling, the SIA comes mainly from an anisotropic deformation of the orbital due to the spontaneous polarization in  $\text{BiFeO}_3$ . Recent DFT calculations [68] suggests that the competing antiferrodistortive (AFD) and ferroelectric (FE) distortions produces, respectively, easy-plane (AFD) and easy-axis (FE) anisotropies. The final form of the SIA is then determined by the relative amplitudes of these two distortions, which Weingart *et al.* concluded to be of the easy-plane type with a

magnitude of  $-1.3 \mu\text{eV}$  [68], in contrast to much of the literature which assumes an easy-axis type anisotropy: a more recent DFT calculation found a magnetic easy axis with  $\mathcal{K} = 3.5 \mu\text{eV}$  [69]. Moreover, the spin cycloid is no longer harmonic when the SIA is included [36]. While NMR and Mössbauer measurements [70–72] indicated that a large anharmonicity is present, this could not be measured by neutron diffraction [55, 73–75]. A precise measurement of the strength of the DM interaction and SIA would thus resolve this inconsistency. Finally, the measurements of Rovillain *et al.* [76] and theory of de Sousa *et al.* [77] suggests that the SIA may be altered by an applied electric field in a linear magnetoelectric effect.

## 3.2 Linear spin wave theory on a rotating frame

To determine the magnon dispersion, the usual steps in linear spin wave theory, namely bosonization of the Hamiltonian (3.2) by using the Holstein-Primakoff [78] transformation and diagonalization in momentum space using the Bogoliubov transformation, are carried out yielding the excitation energies  $\hbar\omega(\mathbf{q})$ , and for inelastic neutron scattering, the scattering function  $S(\mathbf{q}, \omega)$ .

### 3.2.1 Holstein-Primakoff transform

The basic idea of the Holstein-Primakoff transform is to express the state of a spin using a set of bosonic operators. This can be illustrated for the classical example of the angular momentum operators of quantum mechanics. For any set of right-handed orthogonal axes, the components of this vector operator can be defined as  $S^x$ ,  $S^y$  and  $S^z$ , which are mutually noncommuting, i.e.,  $[S^x, S^y] = i\hbar S^z$  and cyclic permutations. In order to uniquely specify the states of a spin, one can diagonalize any set of commuting operators. Normally the SU(2) Casimir operators  $S^2$  and  $S^z$  are used, which leads to states with the quantum numbers  $|S, m\rangle$ :

$$S^2 |S, m\rangle = \hbar^2 S(S+1) |S, m\rangle, \quad (3.10)$$

$$S^z |S, m\rangle = \hbar m |S, m\rangle, \quad (3.11)$$

where the projection quantum number  $m$  takes on all the values  $-S, -S+1, \dots, S-1, S$ .

For a single particle of spin  $S$  (i.e., a single irreducible representation of

### 3. Spin waves calculations

---

SU(2)), now consider the state with maximal projection  $|S, m = +S\rangle$ , the extremal weight state as a vacuum for a set of boson operators, and each subsequent state with lower projection quantum number as a boson excitation of the previous one,  $|S, S - n\rangle \mapsto \frac{1}{\sqrt{n!}} (a^\dagger)^n |0\rangle_B$ . Each added boson then corresponds to a decrease of  $\hbar$  in the spin projection. The spin raising and lowering operators  $S^+ = S^x + iS^y$  and  $S^- = S^x - iS^y$  therefore correspond to the bosonic annihilation and creation operators, respectively. The precise relations between the operators must be chosen to ensure the correct commutation relations for the angular momentum operators. The Holstein–Primakoff transformation can be written as:

$$S^+ = \hbar\sqrt{2S}\sqrt{1 - \frac{a^\dagger a}{2S}}a, \quad (3.12)$$

$$S^- = \hbar\sqrt{2S}a^\dagger\sqrt{1 - \frac{a^\dagger a}{2S}}, \quad (3.13)$$

$$S^z = \hbar(S - a^\dagger a). \quad (3.14)$$

The transformation is particularly useful in the case where  $S$  is large, when the square roots can be expanded as Taylor series, to give an expansion in decreasing powers of  $S$ .

As an example, consider the spin Hamiltonian including only the Heisenberg exchange interactions given as

$$\mathcal{H}_{\text{exch}} = \sum_{\mathbf{r}, \Delta} \mathcal{J}_\Delta \mathbf{S}_\mathbf{r} \cdot \mathbf{S}_{\mathbf{r}+\Delta} = \mathcal{J} \sum_{\mathbf{r}, \alpha} \mathbf{S}_\mathbf{r} \cdot \mathbf{S}_{\mathbf{r}+\alpha} + \mathcal{J}' \sum_{\mathbf{r}, \beta} \mathbf{S}_\mathbf{r} \cdot \mathbf{S}_{\mathbf{r}+\beta}, \quad (3.15)$$

where  $\mathcal{J}_\Delta$  is the interaction parameter for neighbouring spins with the displacement vector  $\Delta$  (see figure 3.1). Here,  $\mathcal{J} = \mathcal{J}_\alpha$  and  $\mathcal{J}' = \mathcal{J}_\beta$  are for the NN and NNN with the displacement vectors  $\alpha$  and  $\beta$ , respectively. The magnon dispersion relation  $\omega(\mathbf{q})$  and structure factor  $S(\mathbf{q}, \omega)$  can be calculated using the Holstein–Primakoff boson operators. Assuming a G-type antiferromagnetic (AFM) structure, the spin operators at two AFM sublattices can be written as

$$\begin{aligned} S_1^z &= S - b_1^\dagger b_1 & S_2^z &= -S + b_2^\dagger b_2 \\ S_1^+ &= \sqrt{2S}b_1 & S_2^+ &= \sqrt{2S}b_2^\dagger \\ S_1^- &= \sqrt{2S}b_1^\dagger & S_2^- &= \sqrt{2S}b_2 \end{aligned}, \quad (3.16)$$

with the boson operators  $b_i$  and  $b_i^\dagger$  obeying  $[b_i, b_j^\dagger] = \delta_{ij}$ . In other words, the spin operator vector at the position  $\mathbf{r}$  can be expressed as

$$\begin{aligned} \mathbf{S}_{\mathbf{r}} &= R_x(\mathbf{Q}_G \cdot \mathbf{r}) \mathbf{T}_{\mathbf{r}}, & T_{\mathbf{r}}^x &= \sqrt{S/2} (b_{\mathbf{r}} + b_{\mathbf{r}}^\dagger) \\ & & T_{\mathbf{r}}^y &= -i\sqrt{S/2} (b_{\mathbf{r}} - b_{\mathbf{r}}^\dagger), \\ & & T_{\mathbf{r}}^z &= S - b_{\mathbf{r}}^\dagger b_{\mathbf{r}} \end{aligned} \quad (3.17)$$

where  $R_x$  is the rotation matrix about the  $x$ -axis,  $\mathbf{T}_{\mathbf{r}}$  is the spin operator vector defined in a local frame, in which spins are directed to the positive  $z$ -direction, and  $\mathbf{Q}_G$  is the magnetic propagation vector for the collinear G-type AFM state in BiFeO<sub>3</sub>:

$$\mathbf{Q}_G = [0 \ 0 \ 3]_{\text{hex}} = [0.5 \ 0.5 \ 0.5]_{\text{pc}}. \quad (3.18)$$

The dot product in the Hamiltonian is simply rewritten as  $\mathbf{S}_{\mathbf{r}} \cdot \mathbf{S}_{\mathbf{r}'} = \mathbf{T}_{\mathbf{r}}^T R_x(\mathbf{Q}_G \cdot \Delta) \mathbf{T}_{\mathbf{r}'}$  and the Hamiltonian can be rewritten as

$$\begin{aligned} \mathcal{H}_{\text{exch}} &= \sum_{\mathbf{r}, \Delta} \mathcal{J}_\Delta \cos(\mathbf{Q}_G \cdot \Delta) \left[ S^2 - 2S b_{\mathbf{r}}^\dagger b_{\mathbf{r}} \right] \\ &+ \frac{S}{2} \sum_{\mathbf{r}, \Delta} \mathcal{J}_\Delta [1 + \cos(\mathbf{Q}_G \cdot \Delta)] K_{\mathbf{r}, \mathbf{r}+\Delta} \\ &+ \frac{S}{2} \sum_{\mathbf{r}, \Delta} \mathcal{J}_\Delta [1 - \cos(\mathbf{Q}_G \cdot \Delta)] P_{\mathbf{r}, \mathbf{r}+\Delta} \end{aligned} \quad (3.19)$$

where  $K_{\mathbf{r}, \mathbf{r}'} = b_{\mathbf{r}} b_{\mathbf{r}'}^\dagger + b_{\mathbf{r}'}^\dagger b_{\mathbf{r}}$  and  $P_{\mathbf{r}, \mathbf{r}'} = b_{\mathbf{r}} b_{\mathbf{r}'} + b_{\mathbf{r}}^\dagger b_{\mathbf{r}'}^\dagger$ . Taking the Fourier transform

$$b_{\mathbf{r}} = \frac{1}{\sqrt{N}} \sum_{\mathbf{k}} e^{i\mathbf{k} \cdot \mathbf{r}} b_{\mathbf{k}}, \quad b_{\mathbf{r}}^\dagger = \frac{1}{\sqrt{N}} \sum_{\mathbf{k}} e^{-i\mathbf{k} \cdot \mathbf{r}} b_{\mathbf{k}}^\dagger, \quad (3.20)$$

the Hamiltonian can be rewritten as

$$\mathcal{H}_{\text{exch}} = NS^2 I_0 + S \sum_{\mathbf{k}} \begin{pmatrix} b_{\mathbf{k}}^\dagger & b_{-\mathbf{k}} \end{pmatrix} \begin{pmatrix} A_{\mathbf{k}} & B_{\mathbf{k}} \\ B_{\mathbf{k}} & A_{\mathbf{k}} \end{pmatrix} \begin{pmatrix} b_{\mathbf{k}} \\ b_{-\mathbf{k}}^\dagger \end{pmatrix}, \quad (3.21)$$

where

$$A_{\mathbf{k}} = \frac{1}{2} (I_{\mathbf{k}} + J_{\mathbf{k}}) - I_0, \quad B_{\mathbf{k}} = \frac{1}{2} (J_{\mathbf{k}} - I_{\mathbf{k}}), \quad (3.22)$$

$$I_{\mathbf{k}} = \sum_{\Delta} \mathcal{J}_\Delta \cos(\mathbf{Q}_G \cdot \Delta) \cos(\mathbf{k} \cdot \Delta), \quad J_{\mathbf{k}} = \sum_{\Delta} \mathcal{J}_\Delta \cos(\mathbf{k} \cdot \Delta). \quad (3.23)$$

Performing the Bogoliubov transformation

$$\begin{pmatrix} b_{\mathbf{k}} \\ b_{-\mathbf{k}}^\dagger \end{pmatrix} = \begin{pmatrix} \cosh \lambda_{\mathbf{k}} & \sinh \lambda_{\mathbf{k}} \\ \sinh \lambda_{\mathbf{k}} & \cosh \lambda_{\mathbf{k}} \end{pmatrix} \begin{pmatrix} \gamma_{\mathbf{k}} \\ \gamma_{-\mathbf{k}}^\dagger \end{pmatrix}, \quad (3.24)$$

with  $\tanh 2\lambda_{\mathbf{k}} = -B_{\mathbf{k}}/A_{\mathbf{k}}$ , the Hamiltonian is diagonalized as

$$\mathcal{H}_{\text{exch}} = E_{cl} + S \sum_{\mathbf{k}} \omega_{\mathbf{k}} + \sum_{\mathbf{k}} 2S\omega_{\mathbf{k}} \gamma_{\mathbf{k}}^\dagger \gamma_{\mathbf{k}}, \quad (3.25)$$

$$\omega_{\mathbf{k}} = \sqrt{A_{\mathbf{k}}^2 - B_{\mathbf{k}}^2} = \sqrt{(J_{\mathbf{k}} - I_0)(I_{\mathbf{k}} - I_0)}, \quad (3.26)$$

where  $E_{cl} = NS^2I_0$  is the classical ground-state energy, the second term gives an  $O(1/S)$  quantum correction to the energy, and  $2S\omega_{\mathbf{k}}$  is the magnon energy.

### 3.2.2 Rotating local frame method

A non-collinear spin structure such as a spiral or cycloid usually makes calculation difficult by adding more sites in an effectively extended magnetic unit cell. When the rotating magnetic structure can be described by the magnetic propagation vector, however, it becomes much simpler. To simplify the spin wave calculation for the spiral or cycloid state, the rotated coordinate  $(T_{\mathbf{r}}^x, T_{\mathbf{r}}^y, T_{\mathbf{r}}^z)$  for spins can be introduced, so that the  $z$  axis at each site is aligned with the classical spin direction [79]. Then the spin wave dispersion can be calculated on a single site because the spins expressed in a rotating coordinate frame effectively form a ferromagnetic state. In the following section, I will show how it works for simple cycloid systems.

### 3.2.3 Simple cycloid systems: $\mathcal{J}$ - $\mathcal{J}'$ - $\mathcal{D}_u$ model

Consider the Hamiltonian

$$\mathcal{H} = \mathcal{J} \sum_{\text{NN}} \mathbf{S}_{\mathbf{r}} \cdot \mathbf{S}_{\mathbf{r}'} + \mathcal{J}' \sum_{\text{NNN}} \mathbf{S}_{\mathbf{r}} \cdot \mathbf{S}_{\mathbf{r}'} - \mathcal{D}_u \sum_{\mathbf{r}} \hat{u} \cdot (\mathbf{S}_{\mathbf{r}} \times \mathbf{S}_{\mathbf{r}+a\hat{v}}), \quad (3.27)$$

where the first and second sums run over nearest-neighbor (NN) and next-nearest-neighbor (NNN) pairs, respectively. I have introduced the Dzyaloshinskii-Moriya (DM) interaction  $\mathcal{D}_u$  between NNN pairs  $(\mathbf{r}, \mathbf{r} + a\hat{v})$  along the  $v$  direction. The classical ground state of the model (3.27) is a cycloid in the  $vc$  plane with the

propagation vector  $\mathbf{Q} = q\hat{v} + (6\pi/c)\hat{c}$  with  $qa = 2\mathcal{D}_u/(\mathcal{J} - 4\mathcal{J}')$  for  $\mathcal{D}_u \ll \mathcal{J}, \mathcal{J}'$  (see Appendix A.2).

Using a rotating local frame, the original spin operator  $\mathbf{S}_r$  is obtained with a site-dependent angle  $\mathbf{Q} \cdot \mathbf{r}$  around the  $u$  axis:

$$\begin{aligned} S_r^u &= T_r^x \\ S_r^v &= T_r^y \cos(\mathbf{Q} \cdot \mathbf{r}) - T_r^z \sin(\mathbf{Q} \cdot \mathbf{r}) , \\ S_r^c &= T_r^y \sin(\mathbf{Q} \cdot \mathbf{r}) + T_r^z \cos(\mathbf{Q} \cdot \mathbf{r}) \end{aligned} \quad (3.28)$$

with

$$\begin{aligned} T_r^x &= \sqrt{S/2} (b_r + b_r^\dagger) \\ T_r^y &= -i\sqrt{S/2} (b_r - b_r^\dagger) , \\ T_r^z &= S - b_r^\dagger b_r \end{aligned} \quad (3.29)$$

where  $b_r$  is a bosonic annihilation operator. Taking the Fourier transform (3.20), the linear spin wave Hamiltonian can be calculated in the same way as section 3.2.1:

$$H = E_{\text{cl}} + S \sum_{\mathbf{k}} \begin{pmatrix} b_{\mathbf{k}}^\dagger & b_{-\mathbf{k}} \end{pmatrix} \begin{pmatrix} A_{\mathbf{k}} & B_{\mathbf{k}} \\ B_{\mathbf{k}} & A_{\mathbf{k}} \end{pmatrix} \begin{pmatrix} b_{\mathbf{k}} \\ b_{-\mathbf{k}}^\dagger \end{pmatrix}, \quad (3.30)$$

where

$$E_{\text{cl}} = NS^2 I_0, \quad A_{\mathbf{k}} = \frac{1}{2}(I_{\mathbf{k}} + J_{\mathbf{k}}) - I_0, \quad B_{\mathbf{k}} = \frac{1}{2}(J_{\mathbf{k}} - I_{\mathbf{k}}), \quad (3.31)$$

$$I_{\mathbf{k}} = \sum_{\Delta\mathbf{r}} \mathcal{J}_{\Delta\mathbf{r}} \cos(\mathbf{Q} \cdot \Delta\mathbf{r}) \cos(\mathbf{k} \cdot \Delta\mathbf{r}) - \mathcal{D}_u \sin(\mathbf{Q} \cdot (a\hat{v})) \cos(\mathbf{k} \cdot (a\hat{v})), \quad (3.32)$$

$$J_{\mathbf{k}} = \sum_{\Delta\mathbf{r}} \mathcal{J}_{\Delta\mathbf{r}} \cos(\mathbf{k} \cdot \Delta\mathbf{r}). \quad (3.33)$$

Performing the Bogoliubov transformation (3.24), the Hamiltonian is diagonalized as

$$H = E_{\text{cl}} + S \sum_{\mathbf{k}} \omega_{\mathbf{k}} (\gamma_{\mathbf{k}}^\dagger \gamma_{\mathbf{k}} + \gamma_{-\mathbf{k}} \gamma_{-\mathbf{k}}^\dagger) = E_{\text{cl}} + E_1 + \sum_{\mathbf{k}} 2S\omega_{\mathbf{k}} \gamma_{\mathbf{k}}^\dagger \gamma_{\mathbf{k}}. \quad (3.34)$$

with

$$\omega_{\mathbf{k}} = \sqrt{A_{\mathbf{k}}^2 - B_{\mathbf{k}}^2} = \sqrt{(J_{\mathbf{k}} - I_0)(I_{\mathbf{k}} - I_0)}. \quad (3.35)$$

### 3. Spin waves calculations

---

Here,  $E_{\text{cl}} (\propto S^2)$  is the classical ground-state energy, and

$$E_1 = S \sum_{\mathbf{k}} \omega_{\mathbf{k}} \quad (3.36)$$

gives an  $O(1/S)$  correction to the energy. The propagation vector  $\mathbf{Q}$  for the quantum model can be determined in such a way as to minimize  $E_{\text{cl}} + E_1$ . This in general gives a different result from the classical case. But here the classical value for  $\mathbf{Q}$  is simply used and the quantum correction is ignored, since the quantum effect is expected to be small for  $S = 5/2$  and other effects such as the deviation of the real material from the assumed model are potentially more important. Defining

$$\Omega_{\mathbf{k}} = 2S\omega_{\mathbf{k}} = 2S\sqrt{(J_{\mathbf{k}} - I_0)(I_{\mathbf{k}} - I_0)} \quad (3.37)$$

and ignoring the constant term, the diagonalized Hamiltonian is obtained as

$$H = \sum_{\mathbf{k}} \Omega_{\mathbf{k}} \gamma_{\mathbf{k}}^{\dagger} \gamma_{\mathbf{k}}. \quad (3.38)$$

As low-energy excitations, the magnon mode  $\Omega_{\mathbf{k}}$  contains a gapless phason excitation around  $\mathbf{k} = 0$  and a gapped excitation around  $\mathbf{k} = \pm\mathbf{Q}$  with an excitation energy of  $O(\sqrt{\mathcal{D}_u\mathcal{J}}, \sqrt{\mathcal{D}_u\mathcal{J}'})$ . Using the in-plane components  $S_{\mathbf{r}}^{\pm} = S_{\mathbf{r}}^v \pm iS_{\mathbf{r}}^c$  and the out-of-plane component  $S_{\mathbf{r}}^u$ , the dynamical spin structure factors are defined as

$$S^{\bar{\alpha}\alpha}(\mathbf{k}, \omega) = \sum_n |\langle \Psi_{\mathbf{k}}^{\alpha} | S_{\mathbf{k}}^{\alpha} | \text{GS} \rangle|^2 \delta(\omega - E_{n\mathbf{k}}), \quad (3.39)$$

with  $(\bar{\alpha}, \alpha)$  taking combinations which yield the components  $S^{uu}$ ,  $S^{--}$  and  $S^{+-}$ . Here  $|\Psi_{\mathbf{k}}^{\alpha}\rangle$  is an excited state which is obtained by acting  $S_{\mathbf{k}}^{\alpha}$  on the ground state, and  $E_{n\mathbf{k}}$  is its excitation energy. The Fourier transform of the spin operators,  $S_{\mathbf{k}}^{\alpha} = (1/\sqrt{N}) \sum_{\mathbf{r}} e^{-i\mathbf{k}\cdot\mathbf{r}} S_{\mathbf{r}}^{\alpha}$ , has bosonic expressions

$$S_{\mathbf{k}}^u \approx \sqrt{S/2} e^{\lambda_{\mathbf{k}}} (\gamma_{\mathbf{k}} + \gamma_{-\mathbf{k}}^{\dagger}), \quad (3.40)$$

$$S_{\mathbf{k}}^{\pm} \approx \sqrt{N} S \delta_{\mathbf{k}, \pm\mathbf{Q}} - i\sqrt{S/2} e^{-\lambda_{\mathbf{k}-\mathbf{Q}}} (\gamma_{\mathbf{k}\mp\mathbf{Q}} - \gamma_{-\mathbf{k}\pm\mathbf{Q}}^{\dagger}). \quad (3.41)$$

This indicates that in the one-magnon contribution,  $S^{\mp\pm}(\mathbf{k}, \omega)$  detect the excitations at  $E_{\pm}(\mathbf{k}) \equiv \Omega_{-\mathbf{k}\pm\mathbf{Q}}$  while  $S^{uu}(\mathbf{k}, \omega)$  detects the excitation at  $E_u(\mathbf{k}) \equiv \Omega_{-\mathbf{k}}$ .

The coefficient of the delta function is given by

$$A_u \equiv |\langle \Psi_{\mathbf{k}}^u | S_{\mathbf{k}}^u | \text{GS} \rangle|^2 = \frac{S}{2} e^{2\lambda_{\mathbf{k}}} = \frac{S}{2} \sqrt{\frac{J_{\mathbf{k}} - I_0}{I_{\mathbf{k}} - I_0}}, \quad (3.42)$$

$$A_{\pm} \equiv |\langle \Psi_{\mathbf{k}}^{\pm} | S_{\mathbf{k}}^{\pm} | \text{GS} \rangle|^2 = \frac{S}{2} e^{-2\lambda_{\mathbf{k} \mp \mathbf{Q}}} = \frac{S}{2} \sqrt{\frac{I_{\mathbf{k} \mp \mathbf{Q}} - I_0}{J_{\mathbf{k} \mp \mathbf{Q}} - I_0}}. \quad (3.43)$$

### 3.3 Perturbative treatment for the complex ground states

If a second DM interaction or single-ion anisotropy is added, it becomes much more complicated to calculate the spin waves dispersion. Shunsuke Furukawa developed perturbative methods with me to handle this complex magnetic structure corresponding to the full spin Hamiltonian [80].

#### 3.3.1 Canted spin cycloid: $\mathcal{J}$ - $\mathcal{J}'$ - $\mathcal{D}_u$ - $\mathcal{D}_c$ model

Let us treat first the case where another DM term,

$$\mathcal{D}_c \sum_{\mathbf{r}} (-1)^{m_{\mathbf{r}}} \hat{c} \cdot (\mathbf{S}_{\mathbf{r}} \times \mathbf{S}_{\mathbf{r} + (c/2)\hat{c}}), \quad \text{with } m_{\mathbf{r}} = \frac{\hat{c} \cdot \mathbf{r}}{c/6}, \quad (3.44)$$

is added to the Hamiltonian (3.27). Here the integer  $m_{\mathbf{r}}$  labels the hexagonal layer in which  $\mathbf{r}$  resides. The classical ground state of the model is a canted cycloid (see appendix A.3).

Again using the rotated coordinate  $\mathbf{T}_{\mathbf{r}} = (T_{\mathbf{r}}^x, T_{\mathbf{r}}^y, T_{\mathbf{r}}^z)^t$  for spins, the original spin operator  $\mathbf{S}_{\mathbf{r}} = (S_{\mathbf{r}}^u, S_{\mathbf{r}}^v, S_{\mathbf{r}}^c)^t$  is expressed as

$$\mathbf{S}_{\mathbf{r}} = R_c ((-1)^{m_{\mathbf{r}}} \theta) R_u(\phi_{\mathbf{r}}) \mathbf{T}_{\mathbf{r}}, \quad \phi_{\mathbf{r}} = \mathbf{Q} \cdot \mathbf{r} + \phi_0, \quad (3.45)$$

where  $R_c$  and  $R_u$  are rotation matrix around the  $c$  and  $u$  axes, respectively:

$$R_c(\phi) = \begin{pmatrix} \cos \phi & -\sin \phi & 0 \\ \sin \phi & \cos \phi & 0 \\ 0 & 0 & 1 \end{pmatrix}, \quad R_u(\phi) = \begin{pmatrix} 1 & 0 & 0 \\ 0 & \cos \phi & -\sin \phi \\ 0 & \sin \phi & \cos \phi \end{pmatrix}. \quad (3.46)$$

Using (3.45), each term in the Hamiltonian can be expressed in terms of  $\mathbf{T}_{\mathbf{r}}$  operators. Recalling  $\theta = \mathcal{D}_c / (6\mathcal{J})$ , the resulting expressions are expanded in

### 3. Spin waves calculations

---

terms of  $\theta$  and only terms up to linear order in  $\mathcal{D}_u$  and  $\mathcal{D}_c$  are kept:

$$\begin{aligned}
\mathcal{J}\mathbf{S}_r \cdot \mathbf{S}_{r'} &= \mathcal{J}T_r^x T_{r'}^x + \mathcal{J} \cos(\mathbf{Q} \cdot \Delta\mathbf{r})(T_r^y T_{r'}^y + T_r^z T_{r'}^z) \\
&\quad - \mathcal{J} \sin(\mathbf{Q} \cdot \Delta\mathbf{r})(T_r^y T_{r'}^z - T_r^z T_{r'}^y) \\
&\quad - \frac{1}{3}\mathcal{D}_c [T_r^x T_{r'}^y \cos(\mathbf{q} \cdot \mathbf{r}' + \phi_0) + T_r^y T_{r'}^x \cos(\mathbf{q} \cdot \mathbf{r} + \phi_0)] \\
&\quad + \frac{1}{3}\mathcal{D}_c [T_r^x T_{r'}^z \sin(\mathbf{q} \cdot \mathbf{r}' + \phi_0) + T_r^z T_{r'}^x \sin(\mathbf{q} \cdot \mathbf{r} + \phi_0)] \\
&\quad + O(\mathcal{D}_c^2/\mathcal{J}),
\end{aligned} \tag{3.47}$$

$$\begin{aligned}
\mathcal{J}'\mathbf{S}_r \cdot \mathbf{S}_{r'} &= \mathcal{J}'T_r^x T_{r'}^x + \mathcal{J}' \cos(\mathbf{Q} \cdot \Delta\mathbf{r})(T_r^y T_{r'}^y + T_r^z T_{r'}^z) \\
&\quad - \mathcal{J}' \sin(\mathbf{Q} \cdot \Delta\mathbf{r})(T_r^y T_{r'}^z - T_r^z T_{r'}^y),
\end{aligned} \tag{3.48}$$

$$\begin{aligned}
\mathcal{D}_u \hat{u} \cdot (\mathbf{S}_r \times \mathbf{S}_{r'}) &= \mathcal{D}_u \sin(\mathbf{Q} \cdot \Delta\mathbf{r})(T_r^y T_{r'}^y + T_r^z T_{r'}^z) \\
&\quad + \mathcal{D}_u \cos(\mathbf{Q} \cdot \Delta\mathbf{r})(T_r^y T_{r'}^z - T_r^z T_{r'}^y) + O(\mathcal{D}_u \mathcal{D}_c/J),
\end{aligned} \tag{3.49}$$

$$\begin{aligned}
(-1)^{m_r} \mathcal{D}_c \hat{c} \cdot (\mathbf{S}_r \times \mathbf{S}_{r'}) &= -\mathcal{D}_c [T_r^x T_{r'}^y \cos(\mathbf{q} \cdot \mathbf{r}' + \phi_0) + T_r^y T_{r'}^x \cos(\mathbf{q} \cdot \mathbf{r} + \phi_0)] \\
&\quad + \mathcal{D}_c [T_r^x T_{r'}^z \sin(\mathbf{q} \cdot \mathbf{r}' + \phi_0) + T_r^z T_{r'}^x \sin(\mathbf{q} \cdot \mathbf{r} + \phi_0)] + O(\mathcal{D}_c^2/J),
\end{aligned} \tag{3.50}$$

with  $\mathbf{r}' = \mathbf{r} + \Delta\mathbf{r}$ . The terms linear in  $\mathcal{D}_c$  in eqs. (3.47) and (3.50) are new terms which did not exist in the analysis of the  $\mathcal{J}$ - $\mathcal{J}'$ - $\mathcal{D}_u$  model. Performing the Holstein-Primakoff transformation (3.29) and summing over  $\mathbf{r}$ , these terms are rewritten as

$$\begin{aligned}
&\sum_{\mathbf{r}} [T_r^x T_{r+\Delta\mathbf{r}}^y \cos(\mathbf{q} \cdot (\mathbf{r} + \Delta\mathbf{r}) + \phi_0) + T_r^y T_{r+\Delta\mathbf{r}}^x \cos(\mathbf{q} \cdot \mathbf{r} + \phi_0)] \\
&= \frac{S}{2} \sum_{\mathbf{k}} \left[ e^{i\tilde{\phi}_0} \cos((\mathbf{k} + \mathbf{q}) \cdot \Delta\mathbf{r})(b_{\mathbf{k}+\mathbf{q}}^\dagger + b_{-\mathbf{k}-\mathbf{q}})(b_{\mathbf{k}} - b_{-\mathbf{k}}^\dagger) \right. \\
&\quad \left. - e^{-i\tilde{\phi}_0} \cos((\mathbf{k} - \mathbf{q}) \cdot \Delta\mathbf{r})(b_{\mathbf{k}-\mathbf{q}}^\dagger + b_{-\mathbf{k}+\mathbf{q}})(b_{\mathbf{k}} - b_{-\mathbf{k}}^\dagger) \right], \tag{3.51}
\end{aligned}$$

$$\begin{aligned}
&\sum_{\mathbf{r}} [T_r^x T_{r+\Delta\mathbf{r}}^z \sin(\mathbf{q} \cdot (\mathbf{r} + \Delta\mathbf{r}) + \phi_0) + T_r^z T_{r+\Delta\mathbf{r}}^x \sin(\mathbf{q} \cdot \mathbf{r} + \phi_0)] \\
&= \sqrt{\frac{NS^3}{2}} \cos(\mathbf{q} \cdot \Delta\mathbf{r}) \left[ e^{i\tilde{\phi}_0} (b_{-\mathbf{q}} + b_{\mathbf{q}}^\dagger) - e^{-i\tilde{\phi}_0} (b_{\mathbf{q}} + b_{-\mathbf{q}}^\dagger) \right] + O(S^{1/2}) \tag{3.52}
\end{aligned}$$

with  $\tilde{\phi}_0 = \phi_0 - \pi/2$ . Equation (3.52) vanishes when  $\mathcal{J}$  and  $\mathcal{D}_c$  interactions are combined. This vanishing of bosonic linear terms indicates the stability of the classical configuration. Equation (3.51) gives the following contribution to the spin wave Hamiltonian:

$$\mathcal{H}' = S \sum_{\mathbf{k}} \left[ e^{i\tilde{\phi}_0} F_{\mathbf{k}+\mathbf{q}} (b_{\mathbf{k}+\mathbf{q}}^\dagger + b_{-\mathbf{k}-\mathbf{q}}) (b_{\mathbf{k}} - b_{-\mathbf{k}}^\dagger) - e^{-i\tilde{\phi}_0} F_{\mathbf{k}-\mathbf{q}} (b_{\mathbf{k}-\mathbf{q}}^\dagger + b_{-\mathbf{k}+\mathbf{q}}) (b_{\mathbf{k}} - b_{-\mathbf{k}}^\dagger) \right] \quad (3.53)$$

with

$$F_{\mathbf{k}} = \frac{D_c}{2} \left[ \cos \left( \mathbf{k} \cdot \sum_{\alpha} \mathbf{B}_{\alpha} \right) - \frac{1}{3} \sum_{\alpha} \cos(\mathbf{k} \cdot \mathbf{B}_{\alpha}) \right]. \quad (3.54)$$

The total spin wave Hamiltonian consists of  $\mathcal{H}$  in (3.27) and the perturbation  $\mathcal{H}'$ . In contrast to  $\mathcal{H}$ ,  $\mathcal{H}'$  does not decouple into different modes  $\mathbf{k}$  and so cannot be diagonalized by the Bogoliubov transformation. Specifically, under the action of  $\mathcal{H}'$ , the modes  $\mathbf{k}$  couple with the modes  $\mathbf{k} \pm \mathbf{q}$ , and then the latter couples with  $\mathbf{k} \pm 2\mathbf{q}$ , etc. To treat this problem,  $\mathcal{H}$  is first diagonalized using the Bogoliubov transformation and the diagonalized form (3.38) is obtained. In terms of  $\gamma_{\mathbf{k}}$  operators,  $\mathcal{H}'$  is expressed as

$$\mathcal{H}' = S \sum_{\mathbf{k}} \left[ e^{i\tilde{\phi}_0} F_{\mathbf{k}}^+ (\gamma_{\mathbf{k}+\mathbf{q}}^\dagger + \gamma_{-\mathbf{k}-\mathbf{q}}) (\gamma_{\mathbf{k}} - \gamma_{-\mathbf{k}}^\dagger) - e^{-i\tilde{\phi}_0} F_{\mathbf{k}}^- (\gamma_{\mathbf{k}-\mathbf{q}}^\dagger + \gamma_{-\mathbf{k}+\mathbf{q}}) (\gamma_{\mathbf{k}} - \gamma_{-\mathbf{k}}^\dagger) \right] \quad (3.55)$$

with  $F_{\mathbf{k}}^{\pm} = F_{\mathbf{k} \pm \mathbf{q}} e^{\lambda_{\mathbf{k} \pm \mathbf{q}} - \lambda_{\mathbf{k}}}$ . If only the mixing of  $\mathbf{k}$  and  $\mathbf{k} \pm \mathbf{q}$  is considered, then it becomes possible to decouple  $\mathcal{H}'$  into separate  $\mathbf{k}$  and  $\mathbf{k} \pm \mathbf{q}$  modes and hence diagonalize it. Specifically, equation (3.55) is encapsulated into the form

$$S \boldsymbol{\gamma}^\dagger M \boldsymbol{\gamma}, \quad (3.56)$$

where

$$M = \begin{pmatrix} M_0 + M_1 & M_2 \\ -M_2 & M_0 - M_1 \end{pmatrix}, \quad M_0 = \begin{pmatrix} \omega_{\mathbf{k}+\mathbf{q}} & 0 & 0 \\ 0 & \omega_{\mathbf{k}} & 0 \\ 0 & 0 & \omega_{\mathbf{k}-\mathbf{q}} \end{pmatrix}, \quad (3.57)$$

$$M_1 = \begin{pmatrix} 0 & F_{\mathbf{k}}^+ - F_{\mathbf{k}+\mathbf{q}}^- & 0 \\ F_{\mathbf{k}}^+ - F_{\mathbf{k}+\mathbf{q}}^- & 0 & F_{\mathbf{k}-\mathbf{q}}^+ - F_{\mathbf{k}}^- \\ 0 & F_{\mathbf{k}-\mathbf{q}}^+ - F_{\mathbf{k}}^- & 0 \end{pmatrix}, \quad (3.58)$$

$$M_2 = \begin{pmatrix} 0 & -F_{\mathbf{k}}^+ - F_{\mathbf{k}+\mathbf{q}}^- & 0 \\ F_{\mathbf{k}}^+ + F_{\mathbf{k}+\mathbf{q}}^- & 0 & -F_{\mathbf{k}-\mathbf{q}}^+ - F_{\mathbf{k}}^- \\ 0 & F_{\mathbf{k}-\mathbf{q}}^+ + F_{\mathbf{k}}^- & 0 \end{pmatrix}, \quad (3.59)$$

$$\gamma = \begin{pmatrix} \tilde{\gamma}_{\mathbf{k}+\mathbf{q}} \\ \gamma_{\mathbf{k}} \\ \tilde{\gamma}_{\mathbf{k}-\mathbf{q}} \\ \tilde{\gamma}_{-\mathbf{k}-\mathbf{q}}^\dagger \\ \gamma_{-\mathbf{k}}^\dagger \\ \tilde{\gamma}_{-\mathbf{k}+\mathbf{q}}^\dagger \end{pmatrix}, \quad (3.60)$$

with  $\tilde{\gamma}_{\mathbf{k}\pm\mathbf{q}} = e^{\mp i\tilde{\phi}_0} \gamma_{\mathbf{k}\pm\mathbf{q}}$  and  $\tilde{\gamma}_{-\mathbf{k}\pm\mathbf{q}} = e^{\mp i\tilde{\phi}_0} \gamma_{-\mathbf{k}\pm\mathbf{q}}$ . This can be diagonalized by performing the generalized Bogoliubov transformation. Although the actual implementation of this transformation is a little involved, the energy spectrum can be obtained just by calculating the eigenvalues of  $\eta M$  with  $\eta = \text{diag}(1, 1, 1, -1, -1, -1)$  and multiplying  $2S$  to them.

### 3.3.2 Anharmonic spin cycloid: $\mathcal{J}$ - $\mathcal{J}'$ - $\mathcal{D}_u$ - $\mathcal{K}$ model

If instead of  $\mathcal{D}_c$ , the single anisotropy term,

$$- \mathcal{K} \sum_{\mathbf{r}} (S_{\mathbf{r}}^c)^2 \quad (3.61)$$

is added to the Hamiltonian (3.27), then the classical ground state is an anharmonic cycloid, which has an additional site-dependent modulation in the simple cycloid structure (see appendix A.4).

The original spin operator  $\mathbf{S}_{\mathbf{r}} = (S_{\mathbf{r}}^x, S_{\mathbf{r}}^y, S_{\mathbf{r}}^z)^t$  is expressed as

$$\mathbf{S}_{\mathbf{r}} = R_u(\phi_{\mathbf{r}}) \mathbf{T}_{\mathbf{r}} = \begin{pmatrix} T_{\mathbf{r}}^x \\ T_{\mathbf{r}}^y \cos \phi_{\mathbf{r}} - T_{\mathbf{r}}^z \sin \phi_{\mathbf{r}} \\ T_{\mathbf{r}}^y \sin \phi_{\mathbf{r}} + T_{\mathbf{r}}^z \cos \phi_{\mathbf{r}} \end{pmatrix}, \quad \phi_{\mathbf{r}} = \mathbf{Q} \cdot \mathbf{r} + \phi_0 + \psi_{\mathbf{r}}. \quad (3.62)$$

The value of  $\phi_0$  is not important as long as  $\mathbf{Q}$  is incommensurate, so  $\phi_0 = 0$  is

set for simplicity. Each term in the Hamiltonian is expressed using  $\mathbf{T}_r$  operators:

$$\begin{aligned} \mathbf{S}_r \cdot \mathbf{S}_{r'} &= T_r^x T_{r'}^x + \cos(\phi_{r'} - \phi_r)(T_r^y T_{r'}^y + T_r^z T_{r'}^z) \\ &\quad - \sin(\phi_{r'} - \phi_r)(T_r^y T_{r'}^z - T_r^z T_{r'}^y), \end{aligned} \quad (3.63)$$

$$\begin{aligned} \hat{u} \cdot (\mathbf{S}_r \times \mathbf{S}_{r'}) &= \sin(\phi_{r'} - \phi_r)(T_r^y T_{r'}^y + T_r^z T_{r'}^z) \\ &\quad + \cos(\phi_{r'} - \phi_r)(T_r^y T_{r'}^z - T_r^z T_{r'}^y), \end{aligned} \quad (3.64)$$

$$\begin{aligned} (S_r^c)^2 &= (T_r^y)^2 \sin^2 \phi_r + (T_r^z)^2 \cos^2 \phi_r \\ &\quad + (T_r^y T_r^z + T_r^z T_r^y) \sin \phi_r \cos \phi_r \end{aligned} \quad (3.65)$$

with  $r' = r + \Delta r$ . The spin wave Hamiltonian is calculated as

$$\mathcal{H} = \mathcal{H}_0 + \mathcal{H}', \quad (3.66)$$

where

$$\begin{aligned} \mathcal{H}_0 &= I_0(NS^2 - 2S \sum_{\mathbf{k}} b_{\mathbf{k}}^\dagger b_{\mathbf{k}}) + \frac{S}{2} \sum_{\mathbf{k}} J_{\mathbf{k}}(b_{\mathbf{k}}^\dagger + b_{-\mathbf{k}})(b_{\mathbf{k}} + b_{-\mathbf{k}}^\dagger) \\ &\quad + \frac{S}{2} \sum_{\mathbf{k}} I_{\mathbf{k}}(b_{\mathbf{k}}^\dagger - b_{-\mathbf{k}})(b_{\mathbf{k}} - b_{-\mathbf{k}}^\dagger) \\ &= NS^2 I_0 + S \sum_{\mathbf{k}} (b_{\mathbf{k}}^\dagger, b_{-\mathbf{k}}) \begin{pmatrix} A_{\mathbf{k}} & B_{\mathbf{k}} \\ B_{\mathbf{k}} & A_{\mathbf{k}} \end{pmatrix} \begin{pmatrix} b_{\mathbf{k}} \\ b_{-\mathbf{k}}^\dagger \end{pmatrix}, \end{aligned} \quad (3.67)$$

with the same  $A_{\mathbf{k}}$ ,  $B_{\mathbf{k}}$ ,  $I_{\mathbf{k}}$  and  $J_{\mathbf{k}}$  in eqs. (3.31), (3.32), and (3.33), and

$$\begin{aligned} \mathcal{H}' &= -\frac{1}{2}NS(S+1)\mathcal{K} + \frac{1}{4}S\mathcal{K} \sum_{\mathbf{k}} (b_{\mathbf{k}}^\dagger + b_{-\mathbf{k}})(b_{\mathbf{k}} + b_{-\mathbf{k}}^\dagger) \\ &\quad + S \sum_{\mathbf{k}} C_{\mathbf{k}} \left[ (b_{\mathbf{k}+\mathbf{q}}^\dagger - b_{-\mathbf{k}-\mathbf{q}})(b_{\mathbf{k}-\mathbf{q}} - b_{-\mathbf{k}+\mathbf{q}}^\dagger) \right. \\ &\quad \quad \left. + (b_{\mathbf{k}-\mathbf{q}}^\dagger - b_{-\mathbf{k}+\mathbf{q}})(b_{\mathbf{k}+\mathbf{q}} - b_{-\mathbf{k}-\mathbf{q}}^\dagger) \right] \\ &\quad + SD \sum_{\mathbf{k}} (b_{\mathbf{k}+\mathbf{q}}^\dagger b_{\mathbf{k}-\mathbf{q}} + b_{\mathbf{k}-\mathbf{q}}^\dagger b_{\mathbf{k}+\mathbf{q}} + b_{-\mathbf{k}-\mathbf{q}} b_{-\mathbf{k}+\mathbf{q}}^\dagger + b_{-\mathbf{k}+\mathbf{q}} b_{-\mathbf{k}-\mathbf{q}}^\dagger) \end{aligned} \quad (3.68)$$

with

$$C_{\mathbf{k}} = \frac{1}{4} \tilde{K} \sum_{\Delta \mathbf{r}} \mathcal{J}_{\Delta \mathbf{r}} \sin(\mathbf{q} \cdot \Delta \mathbf{r}) \sin(\mathbf{Q} \cdot \Delta \mathbf{r}) \cos(\mathbf{k} \cdot \Delta \mathbf{r}) + \frac{1}{4} \tilde{K} \mathcal{D}_u \sin(qa) \cos(qa) \cos(\mathbf{k} \cdot (a\hat{v})) + \frac{\mathcal{K}}{8}, \quad (3.69)$$

$$D = \frac{\mathcal{K}}{2} - 2C_{\mathbf{q}}, \quad \tilde{K} = \frac{\mathcal{K}}{I_{2\mathbf{q}} - I_0}. \quad (3.70)$$

Bosonic linear terms disappear as expected from the stability of the classical magnetic order.  $\mathcal{H}_0$  is the same as the spin wave Hamiltonian (3.30) of the  $\mathcal{J}$ - $\mathcal{J}'$ - $\mathcal{D}_u$  model.  $\mathcal{H}'$  is a new part arising from the  $\mathcal{K}$  term, and has a role of mixing the mode  $\mathbf{k}$  with  $\mathbf{k} \pm 2\mathbf{q}$ ,  $\mathbf{k} \pm 4\mathbf{q}$  and so on.

Now, only the mixing of  $\mathbf{k}$  with  $\mathbf{k} \pm 2\mathbf{q}$  is treated perturbatively, i.e., further mixings such as those between  $\mathbf{k}$  and  $\mathbf{k} \pm 4\mathbf{q}$  are ignored. In the Hamiltonian  $\mathcal{H}_0 + \mathcal{H}'$ , only the terms related to  $\pm \mathbf{k}$  are picked up, which are encapsulated into the form

$$Sb(\mathbf{k})^\dagger M(\mathbf{k})b(\mathbf{k}), \quad (3.71)$$

with

$$M(\mathbf{k}) = \begin{pmatrix} M_1(\mathbf{k}) & M_2(\mathbf{k}) \\ M_2(\mathbf{k}) & M_1(\mathbf{k}) \end{pmatrix}, \quad (3.72)$$

$$M_1(\mathbf{k}) = \begin{pmatrix} A_{\mathbf{k}+2\mathbf{q}} + \frac{\mathcal{K}}{4} & C_{\mathbf{k}+\mathbf{q}} + D & 0 \\ C_{\mathbf{k}+\mathbf{q}} + D & A_{\mathbf{k}} + \frac{\mathcal{K}}{4} & C_{\mathbf{k}-\mathbf{q}} + D \\ 0 & C_{\mathbf{k}-\mathbf{q}} + D & A_{\mathbf{k}-2\mathbf{q}} + \frac{\mathcal{K}}{4} \end{pmatrix}, \quad (3.73)$$

$$M_2(\mathbf{k}) = \begin{pmatrix} B_{\mathbf{k}+2\mathbf{q}} + \frac{\mathcal{K}}{4} & -C_{\mathbf{k}+\mathbf{q}} & 0 \\ -C_{\mathbf{k}+\mathbf{q}} & B_{\mathbf{k}} + \frac{\mathcal{K}}{4} & -C_{\mathbf{k}-\mathbf{q}} \\ 0 & -C_{\mathbf{k}-\mathbf{q}} & B_{\mathbf{k}-2\mathbf{q}} + \frac{\mathcal{K}}{4} \end{pmatrix}, \quad (3.74)$$

$$b(\mathbf{k}) = \begin{pmatrix} b_{\mathbf{k}+2\mathbf{q}} \\ b_{\mathbf{k}} \\ b_{\mathbf{k}-2\mathbf{q}} \\ b_{-\mathbf{k}-2\mathbf{q}}^\dagger \\ b_{-\mathbf{k}}^\dagger \\ b_{-\mathbf{k}+2\mathbf{q}}^\dagger \end{pmatrix}. \quad (3.75)$$

Performing a generalized Bogoliubov transformation  $b(\mathbf{k}) = V(\mathbf{k})\tilde{\gamma}(\mathbf{k})$ , this can

be diagonalized into the form

$$S\tilde{\gamma}(\mathbf{k})^\dagger V^\dagger M(\mathbf{k}) V \tilde{\gamma}(\mathbf{k}) = S\tilde{\gamma}(\mathbf{k})^\dagger \text{diag}(\tilde{\omega}_{\mathbf{k}}^+, \tilde{\omega}_{\mathbf{k}}, \tilde{\omega}_{\mathbf{k}}^-, \tilde{\omega}_{\mathbf{k}}^+, \tilde{\omega}_{\mathbf{k}}, \tilde{\omega}_{\mathbf{k}}^-) \tilde{\gamma}(\mathbf{k}). \quad (3.76)$$

Therefore, magnon modes at  $2S\tilde{\omega}_{\mathbf{k}}$  and  $2S\tilde{\omega}_{\mathbf{k}}^\pm$  are obtained by numerical diagonalization.

The spin operators are expressed as

$$S_{\mathbf{r}}^u = T_{\mathbf{r}}^x \approx \sqrt{\frac{S}{2}}(b_{\mathbf{r}} + b_{\mathbf{r}}^\dagger), \quad (3.77)$$

$$\begin{aligned} S_{\mathbf{r}}^\pm &= S_{\mathbf{r}}^y \pm iS_{\mathbf{r}}^z = (T_{\mathbf{r}}^y \pm iT_{\mathbf{r}}^z)e^{\pm i\phi_{\mathbf{r}}} \\ &\approx \left[ \pm iS - i\sqrt{\frac{S}{2}}(b_{\mathbf{r}} - b_{\mathbf{r}}^\dagger) \right] e^{\pm i\mathbf{Q}\cdot\mathbf{r}}. \end{aligned} \quad (3.78)$$

Performing the Fourier transformation,

$$S_{\mathbf{k}}^u \approx \sqrt{\frac{S}{2}}(b_{\mathbf{k}} + b_{-\mathbf{k}}^\dagger) = \sqrt{\frac{S}{2}}(0, 1, 0, 0, 1, 0)V(\mathbf{k})\tilde{\gamma}(\mathbf{k}), \quad (3.79)$$

$$\begin{aligned} S_{\mathbf{k}}^\pm &\approx \pm i\sqrt{N}S\delta_{\mathbf{k},\pm\mathbf{Q}} - i\sqrt{\frac{S}{2}}(b_{\mathbf{k}\mp\mathbf{Q}} - b_{-\mathbf{k}\pm\mathbf{Q}}^\dagger) \\ &= \pm i\sqrt{N}S\delta_{\mathbf{k},\pm\mathbf{Q}} - i\sqrt{\frac{S}{2}}(0, 1, 0, 0, -1, 0)V(\mathbf{k}\mp\mathbf{Q})\tilde{\gamma}(\mathbf{k}\mp\mathbf{Q}). \end{aligned} \quad (3.80)$$

At the wave vector  $\mathbf{k}$ , the following modes are observed:

$$\begin{aligned} (\text{Energy, Intensity}) &= \left( 2S\omega_{-\mathbf{k}}, \frac{S}{2}|V_{25}(\mathbf{k}) + V_{55}(\mathbf{k})|^2 \right), \\ &\quad \left( 2S\omega_{-\mathbf{k}}^+, \frac{S}{2}|V_{24}(\mathbf{k}) + V_{54}(\mathbf{k})|^2 \right), \\ &\quad \left( 2S\omega_{-\mathbf{k}}^-, \frac{S}{2}|V_{26}(\mathbf{k}) + V_{56}(\mathbf{k})|^2 \right), \\ &\quad \left( 2S\omega_{-\mathbf{k}\pm\mathbf{Q}}, \frac{S}{2}|V_{25}(\mathbf{k}\mp\mathbf{Q}) - V_{55}(\mathbf{k}\mp\mathbf{Q})|^2 \right), \\ &\quad \left( 2S\omega_{-\mathbf{k}\pm\mathbf{Q}}^+, \frac{S}{2}|V_{24}(\mathbf{k}\mp\mathbf{Q}) - V_{54}(\mathbf{k}\mp\mathbf{Q})|^2 \right), \\ &\quad \left( 2S\omega_{-\mathbf{k}\pm\mathbf{Q}}^-, \frac{S}{2}|V_{26}(\mathbf{k}\mp\mathbf{Q}) - V_{56}(\mathbf{k}\mp\mathbf{Q})|^2 \right). \end{aligned} \quad (3.81)$$



## 4. Magnon and phonon excitations in BiFeO<sub>3</sub>

Spin waves are the collective excitations of a magnetic fluctuation in the spin structure, which can be quantized as a quasi-particle called a *magnon* with definite energy and momentum and possessing spin  $S = 1$ . The excitation is fully described by the magnon dispersion relation  $\omega(\mathbf{q})$ , a measurement of which is sufficient to determine the underlying interactions governing the spin dynamics. These interactions include the nearest and next-nearest exchange, Dzyaloshinskii-Moriya interactions and the single-ion anisotropy, and were first included in a Hamiltonian to describe the high field spin structure in a Monte-Carlo calculation [81]. They were subsequently determined in detail by spectroscopic measurements [42, 57, 64, 67, 82]. This chapter will cover the high and low energy spin dynamics in turn.

### 4.1 High energy spin waves governed by exchange interactions

The principal interactions, which determines the local G-type antiferromagnetic structure and high Néel temperature ( $T_N \simeq 640$  K) in BiFeO<sub>3</sub>, are the nearest and next-nearest neighbor exchange interactions (denoted NN and NNN in the subsequent discussion respectively). Since the NN Fe-O-Fe bond has an angle close to 180°, this interaction is strongly antiferromagnetic resulting in a structure in which nearest neighboring spins align anti-parallel. The NNN interaction is also antiferromagnetic, and both interactions are shown in figure 3.1. Due to the requirement of sizeable single crystals, the magnon dispersion measurement which could directly determine these interactions was not completed until recently, when the work [42] detailed in this section was carried out. In addition, Matsuda *et al.* reported, shortly after this work, a similar study using a triple-axis spectrometer [82].

#### 4.1.1 Analysis of AMATERAS data

As explained in section 2.3.2, spin waves of BiFeO<sub>3</sub> were measured with the sample fixed. The data measured can be visualized and analyzed using MSlice. MSlice is a program originally developed by Radu Coldea used to display and

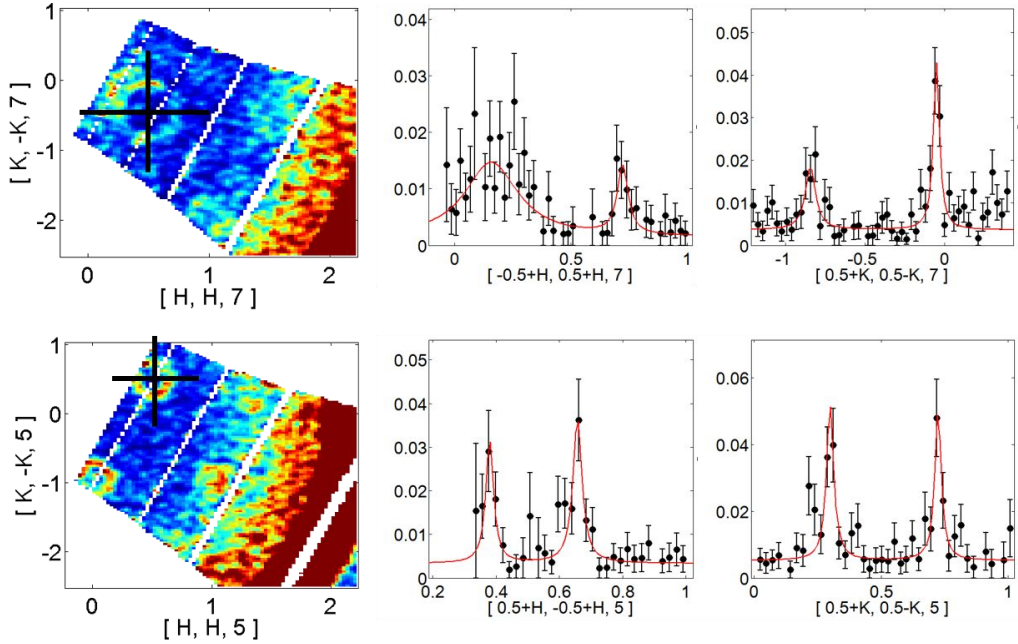


Figure 4.1: Analysis of the experimental data from the AMATERAS experiment using MSlice. A few data points can be obtained by cutting and fitting on the constant- $Q_{\parallel}$  plane.

visualize data given in .spe files produced by Homer. It is available both as a Matlab GUI oriented program and a standalone GUI program.

Experimental data collected with fixed geometry does not contain full 4-dimensional dispersion relation, as already discussed in section 2.2. In order to obtain data points on the highest symmetry axes (see the insert in figure 4.2), I first took slices of data, having an integer  $Q_{\parallel}$  value (see figure 4.1). Although I cannot project all data on a particular plane, the data points obtained from the slices with a constant  $Q_{\parallel}$  can be merged because they have the same spin waves dispersion. Then I cut the slice along the high symmetry direction, and collected peak positions by fitting with a typical Lorentz profile function, as shown in figure 4.1.

In figure 4.2, I show all data points, collected as described above, with the simplest model Hamiltonian that includes only one superexchange interaction term. Surprisingly, the minimal model explains experimental results quite well. However, the number of data points is too limited, especially in high energy region, to determine the interaction strength  $\mathcal{J}$ . Thus another experiment was

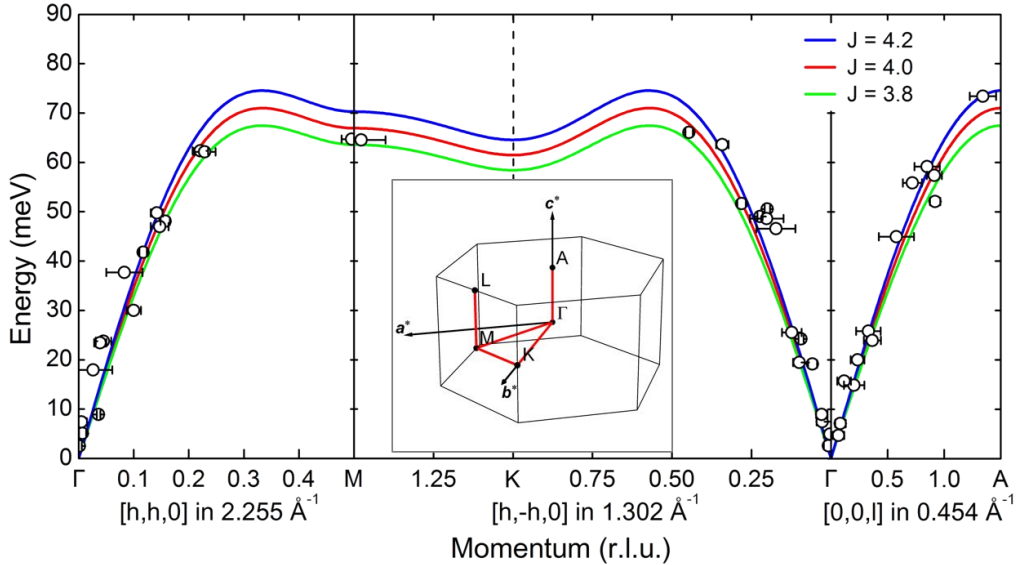


Figure 4.2: Experimental results measured in the AMATERAS experiment with the spin wave dispersion calculated using the simplest model.

conducted with a more advanced method discussed in section 2.3.3, the sample rotation technique.

#### 4.1.2 Analysis of MERLIN data

In the experiment on MERLIN, I collected as many as 171 datasets containing 3-dimensional information at each sample rotation angle. The large number of these single-shot datasets can be merged into a 4-dimensional dataset using Horace program suite. Horace provides the generation, visualization, simulation and fitting of large 4-dimensional datasets obtained by making multiple measurements of a single crystal with varying sample orientation or incident energy from time-of-flight neutron inelastic scattering spectrometers. The feature of Horace that is new compared to MSlice is that it allows us to combine data from multiple runs (each with different incident energy and/or sample orientation) and thus build up a 4-dimensional dataset that, in principle, covers  $\mathbf{Q}$  and energy in all directions.

For a single incident energy and crystal orientation it is clear that one of the components of  $\mathbf{Q}$ , that parallel to the scattered beam, is coupled to time-of-flight rather than detector position. This means that this component of  $\mathbf{Q}$  is coupled to neutron energy transfer. To put simply, the effect of this is that a

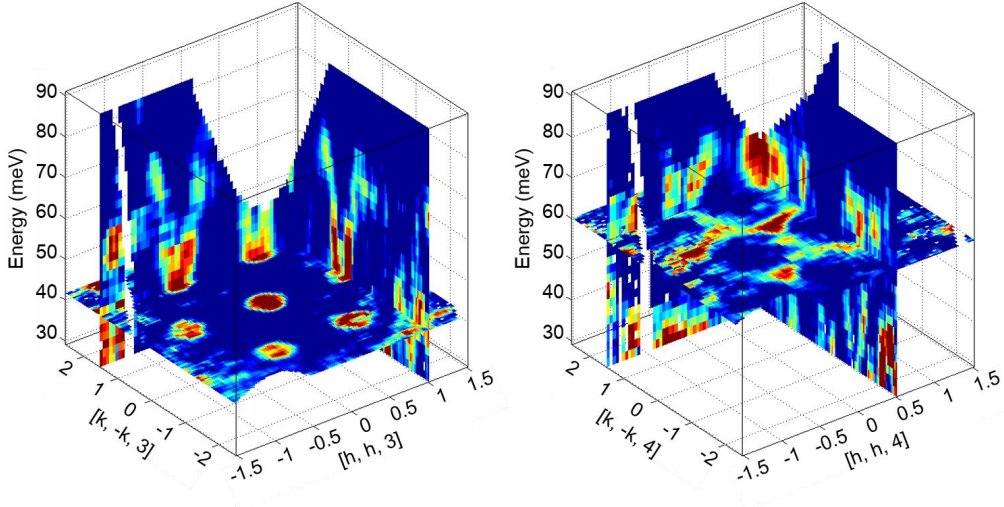


Figure 4.3: Analysis of the experimental data from the MERLIN experiment using Horace. Full 4-dimensional  $\text{Im}[\chi(\mathbf{q}, \omega)]$  were measured in the wide  $q$ - $E$  space.

linear “scan” in  $\mathbf{Q}$  actually follows a curved path in either energy or  $Q_{\parallel}$ . Clearly this can be avoided by taking measurements with a different orientation of the sample with respect to the incident beam, since for different orientations the coupling between  $\mathbf{Q}$  and energy will be different. By making measurements at lots of different sample orientations,  $\mathbf{Q}$  and energy can be completely decoupled.

I found a clear magnon dispersion along all directions using Horace. I show in figure 4.3 some examples that contain full information: energy dispersion along two major axes and constant-energy slice. Although I can obtain the experimental spin waves for any directions of the Brillouin zone using the MERLIN data, I choose  $q$  points of highest symmetry as shown in the insert of figure 4.2. For example, I plot the experimental spin waves for the  $\Gamma$ -M-K- $\Gamma$ -A directions together with the theoretical results in figure 4.4. The contour plot in figure 4.5 is obtained from the combined data of the whole MERLIN experiment while data points denoted by circles are obtained by cutting judiciously the AMATERAS data through each of the related  $q$ - $E$  points. There are two reasons why I do not think that what I measured is not due to phonons. First of all, according to theoretical phonon calculations [83], the experimental dispersion curves are too steep to be acoustic phonon. For example, the acoustic mode only goes up to  $\approx 10$  meV, which is much lower than the top of the spin waves branch at 72.5 meV in the data. Second, the measured excitation becomes weaker when compared at

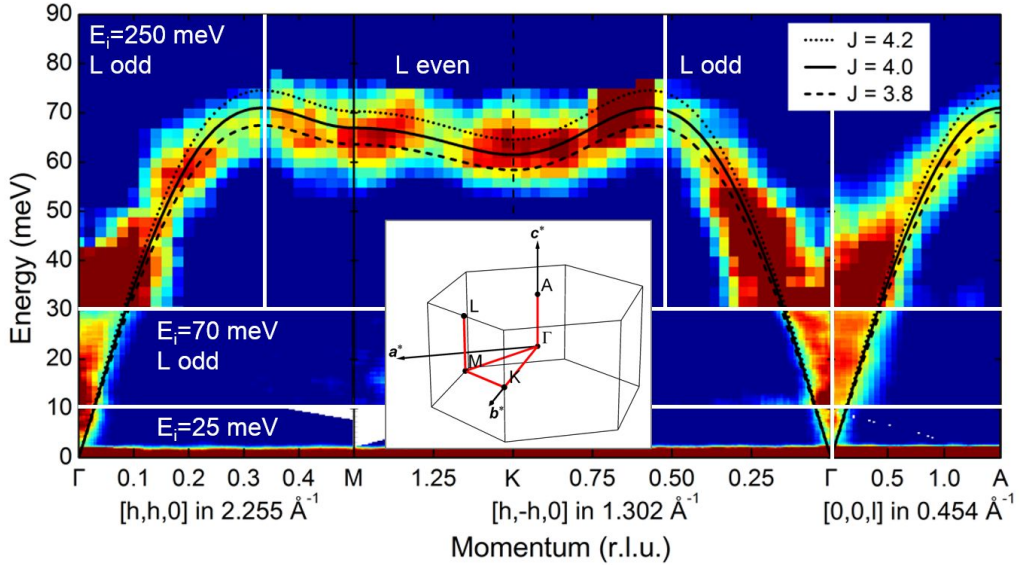


Figure 4.4: Full spin waves dispersion over the Brillouin zone along high symmetry directions, obtained from the MERLIN experiments with  $E_i = 250, 70$  and  $25$  meV. Data are chosen from the  $L$ -odd and  $L$ -even plane for a low- and high-energy region, respectively.

equivalent  $q$  points of different Brillouin zones: with increasing the  $q$  values the intensity of the measured excitations gets reduced following the magnetic form factor.

### 4.1.3 Determination of superexchange interactions

In order to analyze the data, I started with a minimal Heisenberg Hamiltonian only with nearest neighbor interaction ( $\mathcal{J}$ ). I then calculated the theoretical spin waves using a Holstein-Primakoff transformation. In this model Hamiltonian, the value of  $\mathcal{J}$  is determined from the total width of the full dispersion, as  $\mathcal{J} = 4.08$  meV, from the energy of the spin waves at the A point (see the insert in figure 4.5). The dashed line in the figure represents the theoretical spin waves calculated using this minimal model Hamiltonian. Surprisingly, this simple Hamiltonian appears to explain most of the essential features observed in the experimental dispersion. However, upon close inspections, this simple model Hamiltonian fails to reproduce some of the detailed features of the experimental data. For example, as shown in figure 4.5, there are clear discrepancies between the experimental data and the theoretical curves near the M point.

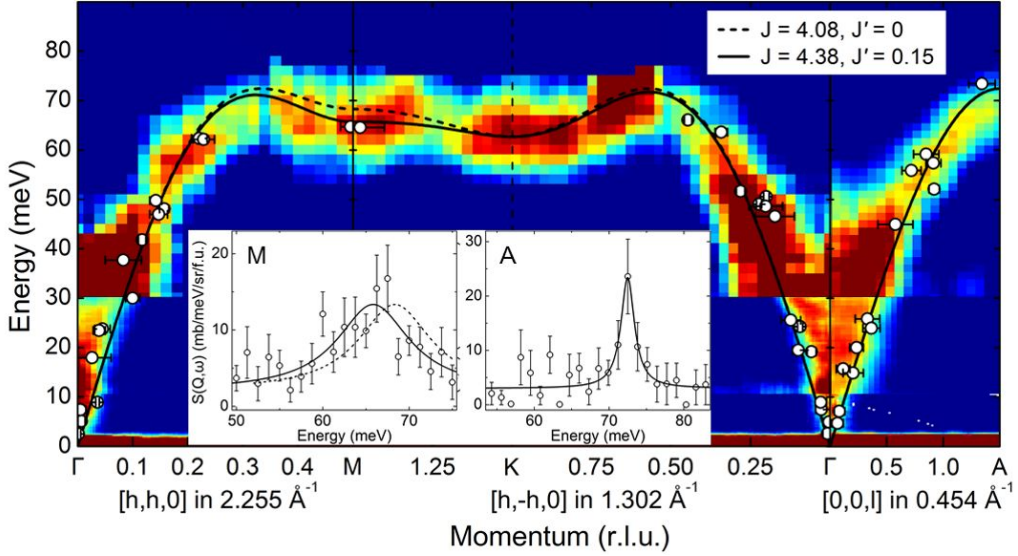


Figure 4.5: Measured full spin waves dispersion with the theoretical curves for the  $\mathcal{J}$ -only and  $\mathcal{J}$ - $\mathcal{J}'$  models. Insets show the constant- $q$  cuts at the M and A points. The solid line for the  $\mathcal{J}$ - $\mathcal{J}'$  model gives better fittings than the dashed line for the minimal  $\mathcal{J}$ -only model [42].

To resolve the discrepancies, I extend the minimal model Hamiltonian by including another exchange interaction term ( $\mathcal{J}'$ ) for the next nearest neighbors (NNN) in addition to a Dzyaloshinskii-Moriya term:

$$\mathcal{H} = \mathcal{J} \sum_{\text{NN}} \mathbf{S}_{\mathbf{r}} \cdot \mathbf{S}_{\mathbf{r}'} + \mathcal{J}' \sum_{\text{NNN}} \mathbf{S}_{\mathbf{r}} \cdot \mathbf{S}_{\mathbf{r}'} - \mathcal{D}_u \sum_{\mathbf{r}} \hat{u} \cdot (\mathbf{S}_{\mathbf{r}} \times \mathbf{S}_{\mathbf{r}+\mathbf{a}\hat{v}}), \quad (4.1)$$

where the first and second sums run over the NN and NNN respectively for the magnetic unit cell of the G-type structure. The third term describes a Dzyaloshinskii-Moriya interaction with  $\mathbf{r}+\mathbf{a}\hat{v}$  representing the next nearest neighbor along the  $[1\ 1\ 0]_h$  axis:  $\hat{u}$  is the chiral vector parallel to the  $[1\ \bar{1}\ 0]_h$ . This is the same Hamiltonian (3.27) in section 3.2.3. It should be noted that this  $\mathcal{D}$  term is an *effective* Dzyaloshinskii-Moriya interaction, composed of several actual microscopic interactions. In the calculations, the dispersion is scaled by an effective spin value of  $S_{\text{eff}} = \sqrt{\frac{5}{2}(\frac{5}{2} + 1)}$  to represent the spin parameter  $S = 5/2$  of Fe<sup>3+</sup>.

Using this new Hamiltonian without the DM term, i.e.  $\mathcal{D}_u = 0$  meV, I could determine a value of  $\mathcal{J} - 2\mathcal{J}'$  by fitting the data at the A point: the energy of the spin waves at the A point is obtained algebraically as  $E_A = 6S_{\text{eff}}(\mathcal{J} - 2\mathcal{J}')$ . I then

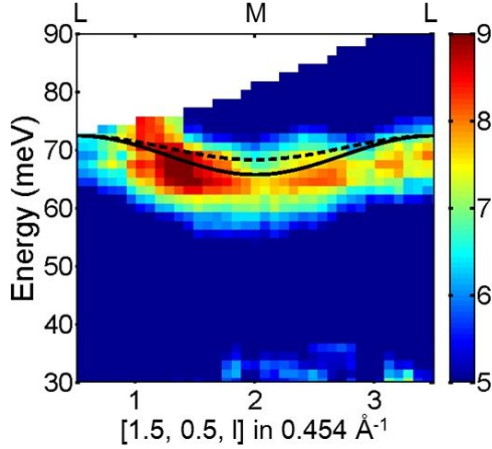


Figure 4.6: Spin waves dispersion along the L-M-L direction with the theoretical curves. The solid line ( $\mathcal{J}$ - $\mathcal{J}'$  model) improves the fitting compared to the dashed line ( $\mathcal{J}$ -only model) [42].

varied  $\mathcal{J}$  and  $\mathcal{J}'$  values systematically in the calculations to fit the experimental data for all the other directions, while keeping the  $\mathcal{J} - 2\mathcal{J}'$  value at 4.08 meV. In particular, the energy at the M and K points can be expressed by the following expressions:

$$E_M = 4S_{\text{eff}} \sqrt{2[(\mathcal{J} - 2\mathcal{J}')^2 - 2\mathcal{J}'(\mathcal{J} - 2\mathcal{J}')]}, \quad (4.2)$$

$$E_K = 3S_{\text{eff}} \sqrt{3[(\mathcal{J} - 2\mathcal{J}')^2 - \mathcal{J}'^2]}. \quad (4.3)$$

From the analysis of the data, the best fitting results were finally obtained with  $\mathcal{J} = 4.38$  and  $\mathcal{J}' = 0.15$  meV, respectively. Using this set of parameters, I succeeded in obtaining a better agreement between the experimental data and the theoretical curve than before. For instance, this new theoretical curve (solid line) now explains the small deviations seen in the  $q$ - $E$  regions around the M points in the previous calculations with the nearest neighbor interaction alone (see figure 4.5). Similar improvements can also be found around many other points of the  $q$ - $E$  space. In figure 4.6, I also display the data together with the theoretical curves for the L-M-L direction, showing again the improvement brought about by the inclusion of the additional term  $\mathcal{J}'$ . Although the inclusion of  $\mathcal{J}'$  improves the fittings, surprisingly the minimal Hamiltonian with a single exchange interaction ( $\mathcal{J}$ ) is a very good approximation to the observed experimental data for most of

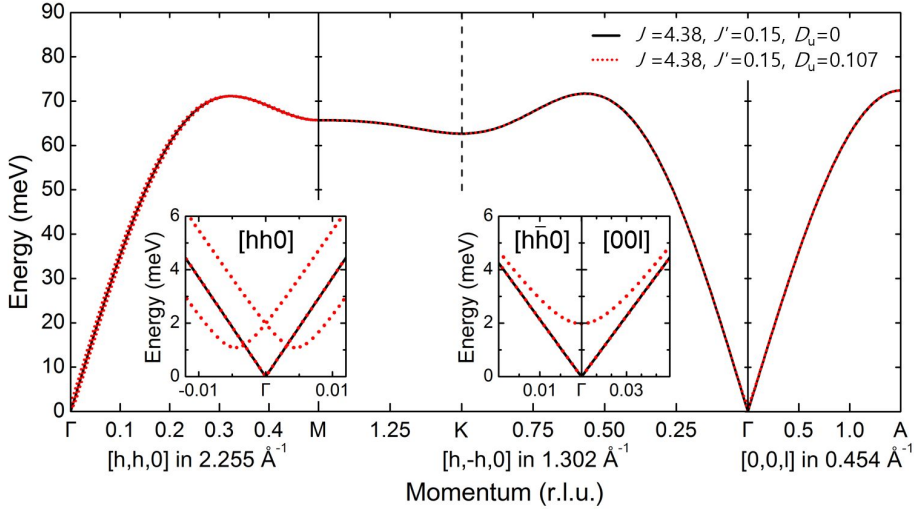


Figure 4.7: Calculated spin wave dispersion with  $\mathcal{J}$ - $\mathcal{J}'$  and  $\mathcal{J}$ - $\mathcal{J}'$ - $\mathcal{D}_u$  models along high symmetry directions. The difference appears only at low energy near the zone center [42].

the  $q$ - $E$  space. The origin of the antiferromagnetic next nearest interaction can be attributed to the large distortion of oxygen octahedron with respect to Fe ions occurring at the ferroelectric transition as discussed before.

I note that this spin Hamiltonian with two exchange interactions is also consistent with all the available bulk data. For example, the final values of  $\mathcal{J}$  and  $\mathcal{J}'$  produces a theoretical  $T_N = 620$  K, which is not far off from the experimental value of 640 K. Moreover, including the DM term with a value of  $\mathcal{D}_u = 0.107$  meV produces an angular deviation of  $3.24^\circ$  between neighboring spins along the  $[1\ 1\ 0]_h$  direction. This angular deviation corresponds to an incommensurate periodicity of  $2\pi \frac{\mathcal{J}-4\mathcal{J}'}{2\mathcal{D}_u} a \approx 620 \text{ \AA}$ ,  $a$  being the  $a$ -axis lattice constant. However, effects of the DM term can only be visible at the very low energy part of the spin waves near the zone center. As shown in 4.7, the inclusion of the DM term splits the low energy modes at the zone center and opens a gap of about 1 meV. I will discuss it in detail at the next section.

In conclusion, I had succeeded, for the first time, in measuring the full spin waves of BiFeO<sub>3</sub> by co-aligning 10 single crystals, and have determined the two most important exchange parameters, which are the nearest and next-nearest neighbor interactions:  $\mathcal{J} = 4.38$  and  $\mathcal{J}' = 0.15$  meV, respectively. Surprisingly, a simple spin Hamiltonian with these two exchange interactions is adequate to

explain the measured full spin waves over the entire Brillouin zone.

## 4.2 Low energy spin waves governed by DM interaction and anisotropy

Although the simple Heisenberg Hamiltonian discussed above describes the measured magnon dispersion quite well, the complex magnetic cycloid structure cannot be stabilised without the Dzyaloshinskii-Moriya (DM) interaction. Moreover, the single-ion anisotropy (SIA) is important in that a large uniaxial anisotropy is expected to destroy the cycloid, whilst smaller values causes the cycloid to become anharmonic. Both these interactions come in part from perturbations induced by a spin orbit coupling, and have a much smaller magnitude than the exchange interactions discussed above. Their effects are thus only apparent in the low energy magnon spectrum. Finally, the DM interaction, in particular, is also the microscopic origin of the Lifshitz invariant term in the free energy density [63] which is responsible for the non-linear magnetoelectric coupling between the cycloid and electric polarization called by some authors the *flexomagnetoelectric* interaction [84]. This was the motivation for detailed measurements of the low energy spin dynamics.

### 4.2.1 Analysis of 4F2 data

Low energy magnon dispersion was measured at several Brillouin zone centers over a wide temperature range. To visualize experimental data, I merged several constant-momentum or constant-energy scans into a two-dimensional array on momentum-energy space, and corrected data by the detailed balance factor to compare with data in different temperatures. I made a GUI program in MATLAB that has useful functions mentioned above. In figure 4.8, I plot measured low-energy magnon dispersion at the Brillouin zone centers  $(1, 0, \bar{1})_h$ ,  $(0, 0, 3)_h$  and  $(1, 0, 5)_h$  at 16 and 270 K. I found an unusual and unique feature, called “island-like” shape, around 1 meV. It is far from the typical V-shaped dispersion for simple antiferromagnets.

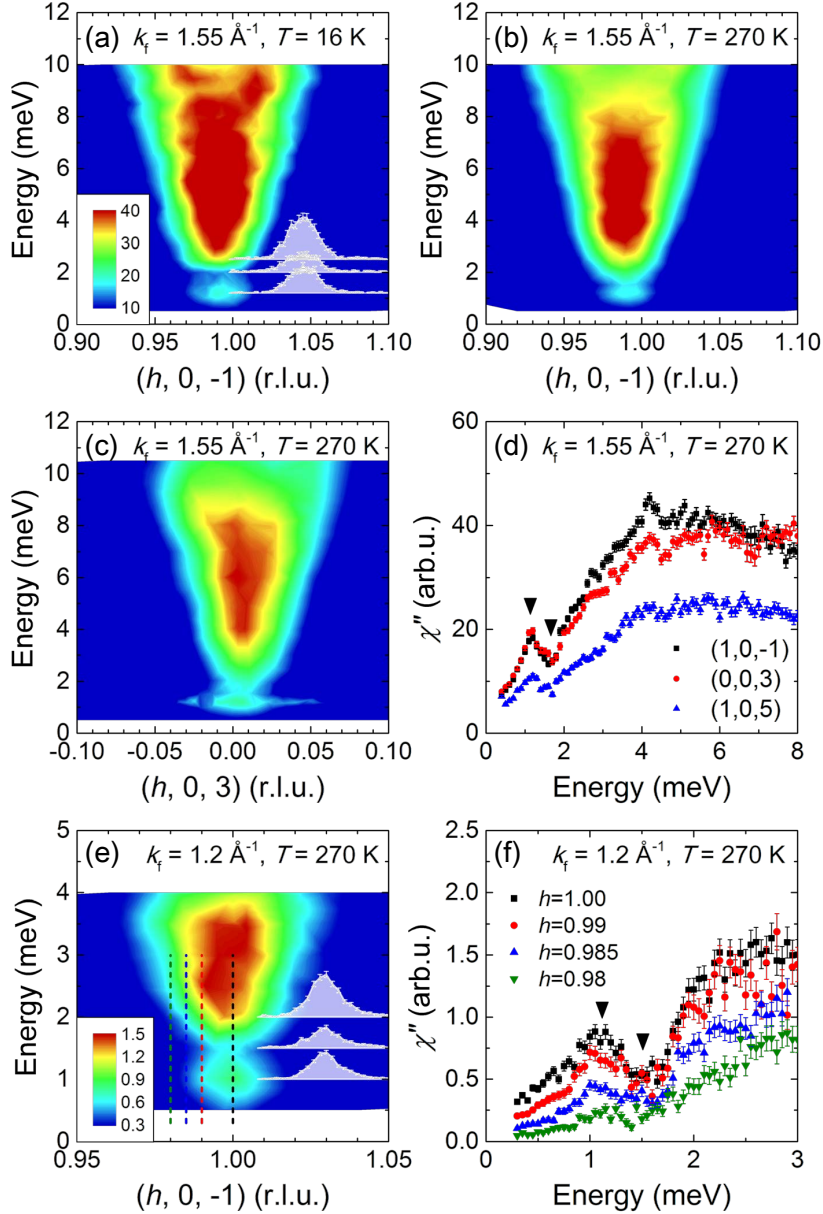


Figure 4.8: (a-c) Experimental  $\text{Im}[\chi(\mathbf{q}, \omega)]$  along the  $[h, 0, 0]$  direction at different temperatures and Brillouin zone centers with  $k_f = 1.55 \text{ \AA}^{-1}$ . (d) Energy scans at three different  $\Gamma$ -points with  $k_f = 1.55 \text{ \AA}^{-1}$ . (e) Higher-resolution  $q$ - $E$  map at  $\mathbf{q} = (1, 0, \bar{1})$  and  $T = 270 \text{ K}$  with  $k_f = 1.2 \text{ \AA}^{-1}$ . (f)  $E$ -scans along dashed lines in (e) with  $k_f = 1.2 \text{ \AA}^{-1}$ . In (a) and (e),  $q$ -scans are shown for three representative low energies.

### 4.2.2 Model Hamiltonian and simulations

Using full Hamiltonian (3.2), the full dispersion curve of spin waves was calculated by using linear spin wave theories. Now five models are examined with different parameters for  $\mathcal{J}$ ,  $\mathcal{D}_u$ ,  $\mathcal{D}_c$  and  $\mathcal{K}$ . Model 1 is the simplest, with only exchange interaction terms ( $\mathcal{D}_u = \mathcal{D}_c = \mathcal{K} = 0$ ). Model 2 includes the main DM term along  $[1, 1, 0]$  ( $\mathcal{D}_u > 0$ ,  $\mathcal{D}_c = \mathcal{K} = 0$ ) as well, which gives the long period magnetic cycloid. In model 3, the additional DM term along  $c$ -axis is included ( $\mathcal{D}_u > 0$ ,  $\mathcal{D}_c > 0$ ,  $\mathcal{K} = 0$ ), which causes a small tilting of the magnetic cycloid plane around the  $c$ -axis. Model 4 contains a small easy-axis SIA instead of the second DM term ( $\mathcal{D}_u > 0$ ,  $\mathcal{D}_c = 0$ ,  $\mathcal{K} > 0$ ). In contrast, a small easy-plane SIA is considered ( $\mathcal{D}_u > 0$ ,  $\mathcal{D}_c = 0$ ,  $\mathcal{K} < 0$ ) in model 5. The small SIA with the DM term produces a slightly anharmonic cycloid due to a modulation of the angle between adjacent spins along the cycloid axis [55], which will be discussed shortly. The magnon dispersion relation  $\omega(\mathbf{q})$  and dynamical structure factor  $S(\mathbf{q}, \omega)$  was calculated for each model using the Holstein-Primakoff boson operators as discussed in chapter 3.

Theoretical spectra along the  $[h\ 0\ 0]_h$  direction are given in figure 4.9. In model 1, three modes detected by different components of  $S(\mathbf{q}, \omega)$  are degenerate whereas these are split by the  $\mathcal{D}_u$  term in the model 2. The additional DM term,  $\mathcal{D}_c$  mixes the modes at the wave vectors  $\mathbf{q}$  and  $\mathbf{q} \pm \mathbf{Q}_m$  (with  $\mathbf{Q}_m = [0.0045\ 0.0045\ 0]$  being the incommensurate vector) and the energy dispersions are folded in a complicated way. However, the mixing amplitude vanishes asymptotically in the low-energy limit, and there is no noticeable difference in the low-energy spectrum. On the other hand, the SIA term in models 4 and 5 makes significant changes; it appreciably mixes the modes at  $\mathbf{q}$  and  $\mathbf{q} \pm 2\mathbf{Q}_m$  even at low energies, and the folded spectrum shows an energy gap at the zone center as indicated.

For a direct comparison with the experimental data, a theoretical simulation was performed for the dynamical magnetic susceptibility  $\text{Im}[\chi(\mathbf{q}, \omega)]$  convoluted with the instrumental resolution function. Taking the resolution matrices at  $E = 3$  meV for  $k_f = 1.55 \text{ \AA}^{-1}$  and at  $E = 1$  meV for  $k_f = 1.2 \text{ \AA}^{-1}$  as representative,  $\text{Im}[\chi(\mathbf{q}, \omega)]$  was numerically calculated with a million  $q$ -points sampled in a Gaussian distribution defined by the resolution ellipsoids and summed. In figure 4.9, the complex mode mixing and the gap in the model 4 reproduces the unique island-like shape very well. The difference is more obvious in the simulated constant- $q$  scans. The characteristic peak at low energy appears only with

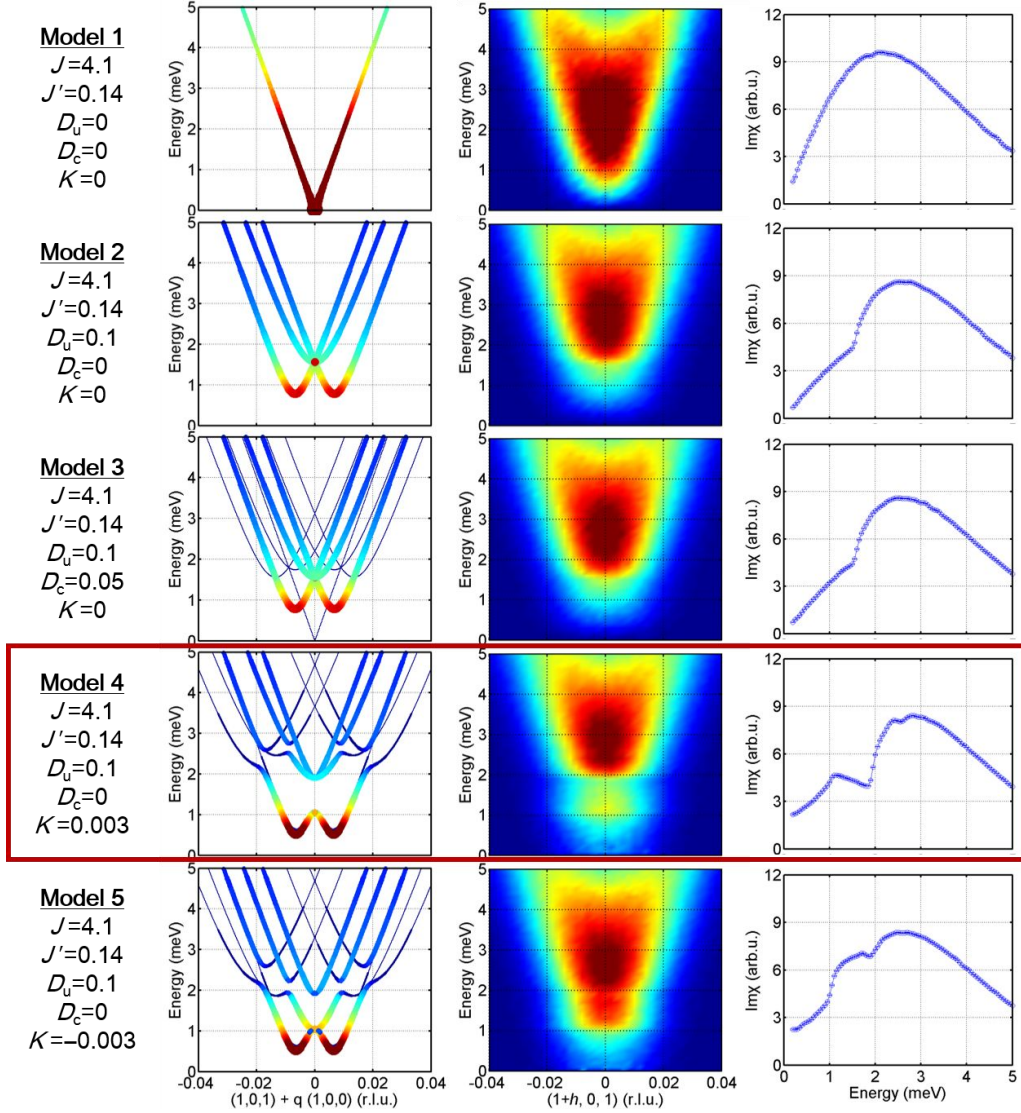


Figure 4.9: Calculated magnon dispersion curves, simulated  $\text{Im}[\chi(\mathbf{q}, \omega)]$  and  $E$ -scans convoluted with the instrumental resolution function centered on  $\mathbf{q} = (1, 0, \bar{1})_h$  for different model parameters.

coexistence of the DM interaction  $\mathcal{D}_u$  and the easy-axis SIA  $\mathcal{K}$ . In model 5, I repeated the calculation for the case of easy-plane magnetic anisotropy, which noticeably fails to reproduce the island-type low energy excitation.

### 4.2.3 Determination of DM interaction and SIA

In order to determine the parameters of the Hamiltonian (3.2), I examined the effect of  $\mathcal{J}$ ,  $\mathcal{D}_u$  and  $\mathcal{K}$  on the simulated  $E$ -scan results. To simplify the problem, the ratio of  $\mathcal{J}$  to  $\mathcal{J}'$  is fixed and their values at 16 K are taken from the previous work:  $\mathcal{J} = 4.38$ ,  $\mathcal{J}' = 0.15$  meV, where I used the effective spin length  $S_{\text{eff}} = \sqrt{\frac{5}{2}(\frac{5}{2} + 1)}$  [42]<sup>1</sup>. The effects of varying  $\mathcal{J}/\mathcal{J}_0$ ,  $\mathcal{D}_u$  and  $\mathcal{K}$  are shown in figure 4.10(a-c):  $\mathcal{J}_0$  is the value at 16 K.  $\mathcal{J}/\mathcal{J}_0$  scales the intensity of the  $E$ -scan,  $\mathcal{D}_u$  determines the position of the peak and dip, and  $\mathcal{K}$  determines the distance between the peak and dip, i.e. the size of the gap. I determine the best fit parameters for various temperatures: at 16 K  $\mathcal{J} = 4.38$ ,  $\mathcal{J}' = 0.15$ ,  $\mathcal{D}_u = 0.109$ , and  $\mathcal{K} = 0.0033$  meV, which are shown with the experimental results in figure 4.10(d-f). I estimate that  $\mathcal{D}_c$  is smaller than 0.05 meV, which appears to be one order of magnitude smaller than estimated from the tilting angle of cycloid plane reported by ref. [56]. I think that the small discrepancy between the data and simulation, in particular the features seen around 4–8 meV in in figure 4.10(e), is due to the fact that in the analysis I have used the common approach of approximating the instrument resolution volume by a Gaussian ellipsoid. However, the true resolution volume is an irregular polyhedron and as such can encompass additional modes not sampled by the Gaussian approximation, leading to extra peaks in the measured spectrum which are not in the simulations, but which do not represent additional modes.

### 4.2.4 Temperature dependence of interaction parameters

The position of the peak and dip varies with temperature as shown with the best fit curves in figure 4.11(a). Although the peak is almost constant, the dip energy changes with temperature. From the best fit parameters, the temperature dependence of  $\mathcal{J}\tilde{S}$ ,  $\mathcal{D}_u\tilde{S}$  and  $\mathcal{K}\tilde{S}$  was obtained as shown in figure 4.11(b), where  $\tilde{S}(T) = S_{\text{eff}}(T)/S_{\text{eff}}(T = 0)$  represents the temperature-dependent normalized moment obtained from ref. [85]. Encouragingly, it agrees with the structural

---

<sup>1</sup>When comparing my values with those in ref. [82], one should convert from my use of effective  $S$  value ( $S_{\text{eff}}$ ) to just  $S$ .

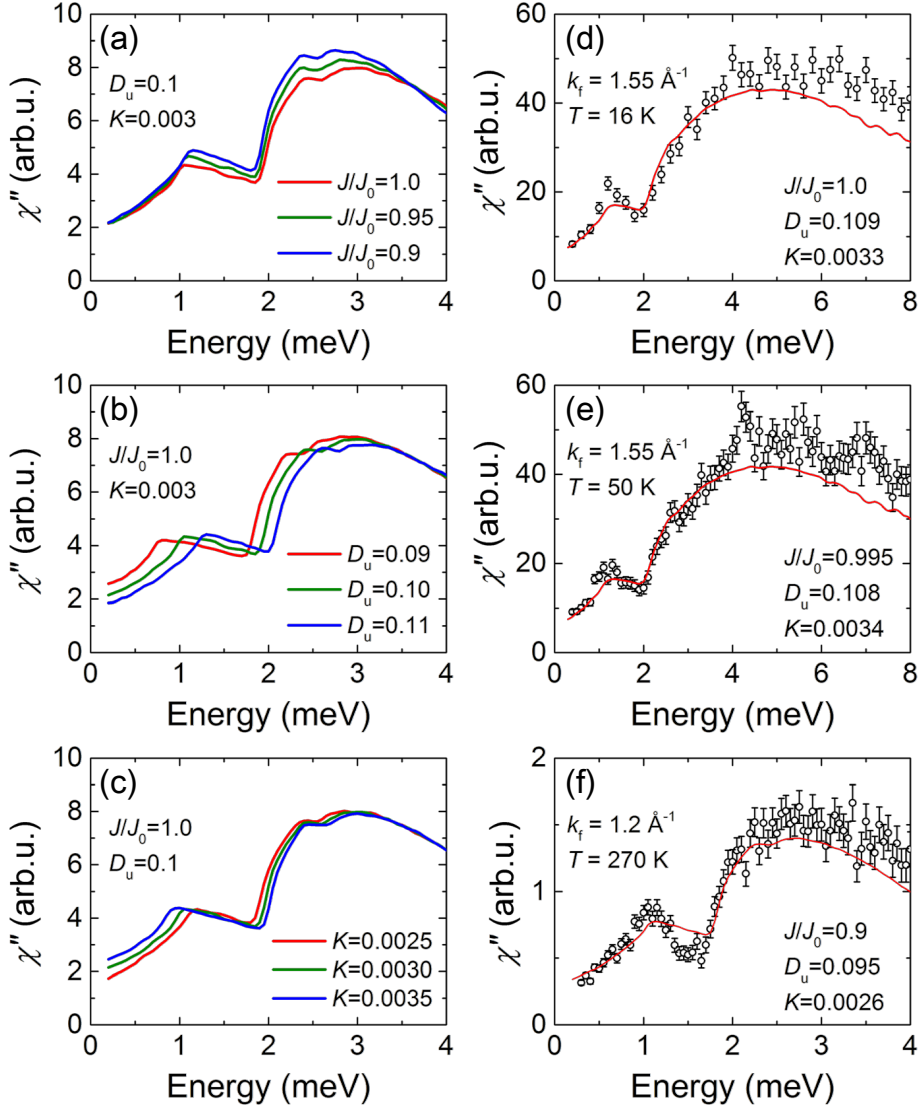


Figure 4.10: Simulation results for different (a)  $\mathcal{J}/\mathcal{J}_0$ , (b)  $D_u$  and (c)  $\mathcal{K}$ . Best fit results with  $k_f = 1.55 \text{ \AA}^{-1}$  at (d) 16 K, (e) 50 K and (f) with  $k_f = 1.2 \text{ \AA}^{-1}$  at 270 K [57].

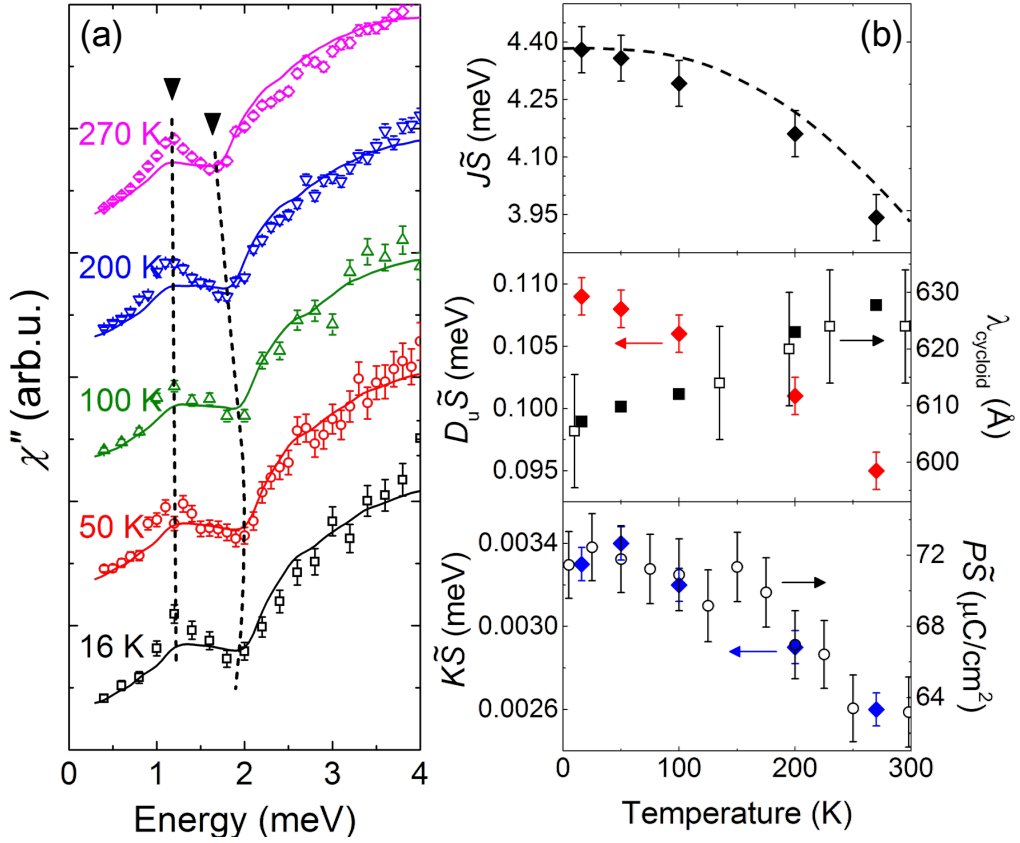


Figure 4.11: (a) Temperature dependence of  $\text{Im}[\chi(\mathbf{q}, \omega)]$  at  $\mathbf{q} = (1, 0, \bar{1})_h$  with best fit curves. (b) Temperature dependence of  $J\tilde{S}$ ,  $D_u\tilde{S}$ ,  $\mathcal{K}\tilde{S}$  and a period of the magnetic cycloid [57]. Temperature dependence of the normalized moment,  $\tilde{S}$  (dashed line) and the electric polarization ( $P$ ) are estimated using the structural data [85], while open symbols of  $\lambda_{\text{cycloid}}$  are taken from ref. [55].

Temp. (K)	$J\tilde{S}$ (meV)	$J'\tilde{S}$ (meV)	$D_u\tilde{S}$ (meV)	$\mathcal{K}\tilde{S}$ (meV)	$\lambda_{\text{cycloid}}$ (Å)
16	4.38	0.15	0.109	0.0033	607.19
50	4.358	0.1493	0.108	0.0034	609.79
100	4.292	0.147	0.106	0.0032	612.01
200	4.161	0.1425	0.101	0.0029	622.97
270	3.942	0.135	0.095	0.0026	627.76

Table 4.1: Temperature dependence of  $J\tilde{S}$ ,  $J'\tilde{S}$ ,  $D_u\tilde{S}$ ,  $\mathcal{K}\tilde{S}$  and a period of the magnetic cycloid.

change that governs each interaction term in the spin Hamiltonian.

I note that the decrease of  $\mathcal{J}\tilde{S}$ ,  $\mathcal{D}_u\tilde{S}$  and  $\mathcal{K}\tilde{S}$  reflects the temperature dependence of the normalized moment ( $\tilde{S}$ ). According to neutron diffraction studies, the moment (dashed line in figure 4.11(b)) is reduced by 10% from low to room temperatures, which almost entirely accounts for the observed change in  $\mathcal{J}\tilde{S}$ , making  $\mathcal{J}$  almost temperature independent.

The DM interaction is proportional to the vector  $\mathbf{r}_{\text{Fe}} \times \mathbf{r}_{\text{O}}$  [63], and thus correlates with the Fe-O-Fe bond angle, which increases slightly with temperature [85]. Thus  $\mathcal{D}_u$  should decrease with temperature, as observed. The incommensurate magnetic cycloid is nearly harmonic with a period approximately proportional to  $(\mathcal{J} - 4\mathcal{J}')/\mathcal{D}_u$  for a small  $\mathcal{K}$ . The periodicity  $\lambda_{\text{cycloid}}$  calculated using the best fit values and the lattice parameters from ref. [85] agrees well with the experimental results [55] as shown in the middle panel of figure 4.11(b). Of further interest, I could directly determine the magnetic anharmonicity value  $m \simeq 0.58\text{--}0.64$ <sup>2</sup> using the best parameters (see appendix A.5). The cycloid anharmonicity, arising from the SIA, allows the coupling of a  $\mathbf{q} = 0$  phonon to magnons beyond the first Brillouin zone [86], and is thus crucial in explaining the observations of many electromagnons in BiFeO<sub>3</sub>. I note that the intensity of third-order satellites is about 300 times weaker than that of first-order satellites in my results, in good agreement with the diffraction result [55, 75] although the  $m$  value is found to be larger than that estimated in ref. [55].

The SIA is thought to be connected to the two structural distortions leading to the acentric  $R3c$  space group: the ferroelectric (FE) displacement and the antiferro-distortive (AFD) rotation. It was recently pointed out by DFT calculations [68] that the exact type of magnetic anisotropy is crucially dependent on the details of the local distortions of the perovskite structure and thus the size of the electric polarization with the FE displacement favoring an easy-axis anisotropy and the AFD rotation inducing an easy-plane anisotropy. While the calculations produce a small *easy-plane* anisotropy, I find experimentally that a small easy-axis anisotropy prevails. Given the precision of DFT calculations, it is unsurprising that such a small difference compared to the total energy is difficult to compute. The temperature dependence of  $\mathcal{K}$  agrees with an increase in the Fe-Bi distance, determined by neutron diffraction [85]. The increasing Fe-Bi distance

---

<sup>2</sup>The period of anharmonic cycloid can be expressed as  $\lambda = 4\sqrt{m/\epsilon} K(m)$  where  $K(m)$  is the complete elliptic integral with the anharmonicity parameter  $m$ , and  $\epsilon = 4\mathcal{K}/(a^2(\mathcal{J} - 4\mathcal{J}'))$ . For a fixed  $\lambda$ ,  $m$  can be estimated numerically.

both reduces the SIA and the electric polarization which are thus correlated, as shown in figure 4.11(b): the polarization is calculated by using the experimental values as in ref. [52]. The fine sensitivity of the SIA to small structural changes may also explain the strong suppression of a magnetic domain under a modest uniaxial pressure  $P \approx 7$  MPa [87]. This small pressure could affect the SIA enough to favour the other two cycloid domains, but is unlikely change the exchange interactions enough to remove the cycloid that way. Furthermore, a large SIA, whilst not realised in BiFeO<sub>3</sub>, could suppress the cycloid leading to a much simpler structure like a G-type antiferromagnetism.

In summary, I confirm that the interplay of the DM interaction and easy-axis SIA is essential to explain the low-energy magnon spectra of BiFeO<sub>3</sub> measured by inelastic neutron scattering experiments. The values of  $\mathcal{J}$ ,  $\mathcal{D}_u$  and  $\mathcal{K}$  were determined at various temperatures by fitting the data, and their temperature dependence is found to be consistent with the structural changes observed by high resolution neutron diffraction [55, 85]. Using these experimental results, I uniquely determined the exact type and temperature dependence of the magnetic anisotropy and the magnetic anharmonicity.

### 4.3 Phonon dispersion in BiFeO<sub>3</sub>

Taking an advantage of the wide detector coverage of ToF INS measurement, phonon excitations were measured at high momentum in the same data used for the analysis of spin waves. To see the details of phonon excitations, TAS measurements were also conducted using cold and thermal neutrons.

#### 4.3.1 Analysis of MERLIN, 4F2 and 1T1 data

The broad phonon excitations were captured at the high momentum regions of the MERLIN datasets with the incident energy of 250 meV. However, the energy resolution was too poor due to the high incident energy, so that the elastic tail wiped up to 30 meV and  $\Delta E > 10$  meV. In the second measurement with the lower incident energies of 70 and 25 meV, I could find some optical phonon modes as well as relatively clear acoustic phonon modes, as shown in figure 4.12. Interestingly, the acoustic phonon modes cross the stiff magnon dispersion near  $\mathbf{q} = (0, -3, 3)_h$  which is the nuclear zone boundary but also the magnetic zone center.

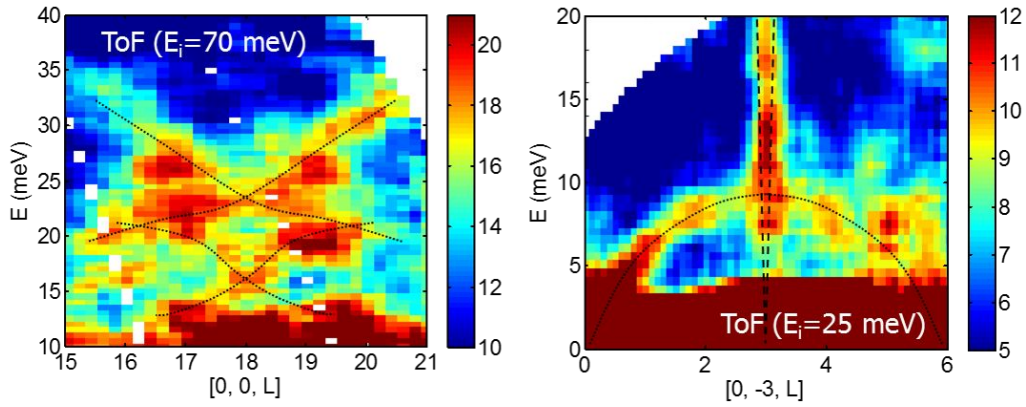


Figure 4.12: Phonon dispersion measured by the ToF method in the MERLIN experiments with  $E_i = 70$  and  $25$  meV. The stiff magnon and acoustic phonon dispersion are overlapped at about  $10$  meV near the magnetic zone center.

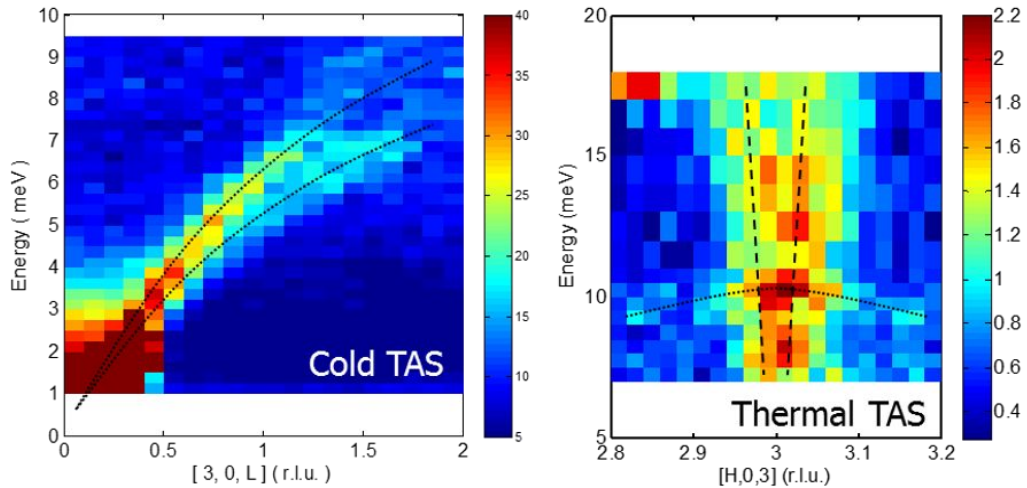


Figure 4.13: Phonon dispersion measured by the TAS method in the 4F2 and 1T1 experiments. The splitting of transverse and longitudinal acoustic phonon modes and the crossing between the stiff magnon and flat phonon dispersion are shown.

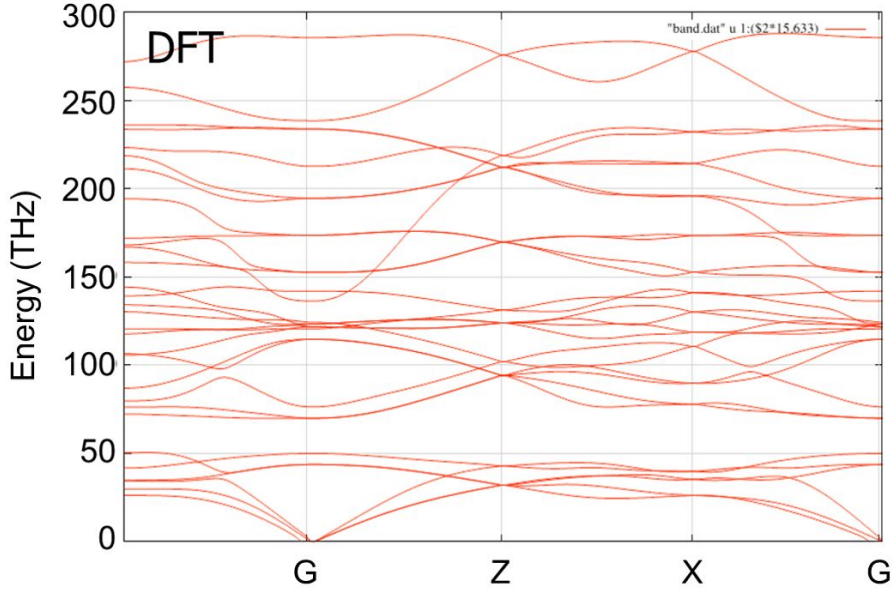


Figure 4.14: Phonon dispersion calculated by DFT in the rhombohedral setting. The soft modes due to an instability of the ground state are shown near the G point [88].

In order to investigate a possible magnon-phonon coupling at this point, I traced acoustic phonon modes along  $(3, 0, 0)_h$ - $(3, 0, 3)_h$  using cold and thermal neutron triple-axis spectrometers 4F2 and 1T1. Unfortunately, the signal of acoustic phonon modes was too weak near the target position  $(3, 0, 3)$ , while the splitting of transverse and longitudinal acoustic phonon modes are clearly shown in the left of figure 4.13. In thermal TAS data measured around  $\mathbf{q} = (3, 0, 3)_h$ , a crossing of the flat phonon modes and stiff magnon modes was measured, but the intensity of signal and resolution were not good enough to come to any conclusions regarding the magnon-phonon coupling.

In order to determine phonon dispersion clearly, Heung-Sik Kim conducted the DFT calculations for the phonon dispersion in the rhombohedral setting, as shown in figure 4.14. The soft modes near the G point (zone center) are related to an instability of the ground state. Due to the difficulties of calculation and the limited computing resources, the phonon dispersion in the hexagonal setting, which can be directly compared with the experimental data, is still in progress [88].



## 5. Summary

Multiferroic materials are one of the most interesting topics in condensed matter physics in the past 20 years.  $\text{BiFeO}_3$  is the most attractive compound due to its having multiferroicity above room temperature and a complex non-collinear magnetic structure. It is important to measure magnon and phonon for the study of its multiferroic nature and complex magnetism.

I coaligned ten single crystals with the total mass of 1.8 g within 3 degrees using the neutron four-circle diffractometer FCD at HANARO for inelastic neutron scattering experiments, which is the most efficient method to measure magnetic excitations. I had succeeded, for the first time, in measuring the full spin waves of  $\text{BiFeO}_3$  using two time-of-flight spectrometers: AMATERAS at J-PARC and MERLIN at ISIS. The two most dominant superexchange interactions between the nearest and next-nearest neighbors were determined:  $\mathcal{J}=4.38$  and  $\mathcal{J}'=0.15$  meV, respectively [42]. Surprisingly, a simple spin Hamiltonian with these two exchange interactions is adequate to explain the measured full spin waves over the entire Brillouin zone.

In order to study the smaller but still important terms in the spin Hamiltonian such as the Dzyaloshinskii-Moriya interaction and single-ion anisotropy, low-energy magnon excitations were measured in detail using the triple-axis spectrometer 4F2 and 1T1 at LLB. I confirm that the interplay of the DM interaction and easy-axis SIA is essential to explain the low-energy magnon spectra of  $\text{BiFeO}_3$ . The values of  $\mathcal{J}$ ,  $\mathcal{D}_u$  and  $\mathcal{K}$  were determined at various temperatures by fitting the data:  $\mathcal{D}_u = 0.11$  and  $\mathcal{K} = 0.033$  with the same  $\mathcal{J}$  and  $\mathcal{J}'$  [57]. Their temperature dependence is consistent with the structural changes observed by high resolution neutron diffraction [55, 85]. Using these experimental results, I uniquely determined the exact type – easy-axis – and temperature dependence of the magnetic anisotropy and the magnetic anharmonicity. The anharmonicity of magnetic cycloid was experimentally determined as  $m \sim 0.58\text{--}0.64$ , which agrees with the diffraction results [55, 75].

Taking an advantage of the wide detector coverage of ToF INS measurement, phonon excitations were measured at high momentum in the same data. In the detail measurements using cold and thermal neutron TAS, the crossing of magnon and phonon dispersion near the magnetic zone center. The study for a possible magnon-phonon coupling and the analysis for phonon dispersion are still in

progress.

The interplay of the DM interaction and anisotropy and their sensitivity to small structural changes may explain a strong strain dependence of the magnetic ground state in BiFeO<sub>3</sub> thin films. The anharmonicity of the magnetic cycloid may be confirmed experimentally under an applied magnetic field, because it is strongly related with the magnetic anisotropy. The relation between electromagnons and the interplay of the DM interaction and anisotropy may be another attractive topic.

# Appendix A. Magnetic ground state

BiFeO<sub>3</sub> has a complex magnetic structure due to the DM interaction and SIA. Starting with the simplest G-type antiferromagnetic structure, magnetic ground states are obtained by ground state energy analysis in this chapter. The spin cycloid structure appears due to the major DM term along  $[1\ 1\ 0]_h$  direction, and canted ferromagnetic components arise locally due to another DM term along  $[0\ 0\ 1]_h$  direction. The anisotropy term gives an anharmonic distortion to the regular cycloid.

## A.1 Hexagonal vs. pseudocubic notations

Let  $\hat{u}$ ,  $\hat{v}$ , and  $\hat{c}$  be the unit vectors along the  $[1, -1, 0]$ ,  $[1, 1, 0]$ , and  $[0, 0, 1]$  axes in the hexagonal notation. Three orthogonal directions are used to represent the components of spins:  $\mathbf{S}_r = (S_r^u, S_r^v, S_r^c)$ .

Primitive vectors  $\mathbf{B}_\alpha$  ( $\alpha = 1, 2, 3$ ) of the pseudo-cubic lattice are given by

$$\mathbf{B}_1 = -\frac{a}{2\sqrt{3}}\hat{u} + \frac{a}{2}\hat{v} + \frac{c}{6}\hat{c}, \quad (\text{A.1})$$

$$\mathbf{B}_2 = -\frac{a}{2\sqrt{3}}\hat{u} - \frac{a}{2}\hat{v} + \frac{c}{6}\hat{c}, \quad (\text{A.2})$$

$$\mathbf{B}_3 = \frac{a}{\sqrt{3}}\hat{u} + \frac{c}{6}\hat{c}. \quad (\text{A.3})$$

Reciprocal lattice vectors  $\mathbf{B}_\alpha^*$  are defined such that  $\mathbf{B}_\alpha \cdot \mathbf{B}_\beta^* = 2\pi\delta_{\alpha\beta}$ . Since  $\mathbf{B}_\alpha$ 's are nearly orthogonal,  $\mathbf{B}_\alpha^* \sim 2\pi\mathbf{B}_\alpha$ .

Primitive vectors in the hexagonal notation are given by

$$\mathbf{a} = \mathbf{B}_3 - \mathbf{B}_2, \quad \mathbf{b} = \mathbf{B}_1 - \mathbf{B}_3, \quad \mathbf{c} = 2(\mathbf{B}_1 + \mathbf{B}_2 + \mathbf{B}_3). \quad (\text{A.4})$$

Reciprocal lattice vectors are given by

$$\mathbf{a}^* = \frac{1}{3}(\mathbf{B}_1^* + \mathbf{B}_3^* - 2\mathbf{B}_2^*), \quad (\text{A.5})$$

$$\mathbf{b}^* = \frac{1}{3}(2\mathbf{B}_1^* - \mathbf{B}_2^* - \mathbf{B}_3^*), \quad (\text{A.6})$$

$$\mathbf{c}^* = \frac{1}{6}(\mathbf{B}_1^* + \mathbf{B}_2^* + \mathbf{B}_3^*). \quad (\text{A.7})$$

Important directions are given by

$$\mathbf{a}^* + \mathbf{b}^* = \mathbf{B}_1^* - \mathbf{B}_2^* = \frac{4\pi}{a} \hat{v} = 2.25 \text{\AA}^{-1} \times \hat{v}, \quad (\text{A.8})$$

$$\mathbf{a}^* - \mathbf{b}^* = \frac{1}{3}(2\mathbf{B}_3^* - \mathbf{B}_1^* - \mathbf{B}_2^*) = \frac{4\pi}{\sqrt{3}a} \hat{u} = 1.30 \text{\AA}^{-1} \times \hat{u}, \quad (\text{A.9})$$

$$\mathbf{c}^* = \frac{1}{6}(\mathbf{B}_1^* + \mathbf{B}_2^* + \mathbf{B}_3^*) = \frac{2\pi}{c} \hat{c} = 0.45 \text{\AA}^{-1} \times \hat{c}, \quad (\text{A.10})$$

where the lattice constant is  $a = 5.58 \text{\AA}$ .

## A.2 Spin cycloid: $\mathcal{J}$ - $\mathcal{J}'$ - $\mathcal{D}_u$ model

The classical ground state of the model (3.27) is a spiral (cycloid) in the  $vc$  plane, which is obtained by rotating the vector  $(0, 0, S)^t$  by site-dependent angles  $\phi_{\mathbf{r}}$ :

$$\mathbf{S}_{\mathbf{r}} = \begin{pmatrix} S_{\mathbf{r}}^u \\ S_{\mathbf{r}}^v \\ S_{\mathbf{r}}^c \end{pmatrix} = R_u(\phi_{\mathbf{r}}) \begin{pmatrix} 0 \\ 0 \\ S \end{pmatrix} = \begin{pmatrix} 0 \\ -S \sin \phi_{\mathbf{r}} \\ S \cos \phi_{\mathbf{r}} \end{pmatrix}, \quad \phi_{\mathbf{r}} = \mathbf{Q} \cdot \mathbf{r} + \phi_0, \quad (\text{A.11})$$

where  $R_u(\phi)$  is a rotation matrix around the  $u$  axis:

$$R_u(\phi) = \begin{pmatrix} 1 & 0 & 0 \\ 0 & \cos \phi & -\sin \phi \\ 0 & \sin \phi & \cos \phi \end{pmatrix}. \quad (\text{A.12})$$

Let us assume the following form for the propagation vector  $\mathbf{Q}$ :

$$\mathbf{Q} = \frac{6\pi}{c} \hat{c} + \mathbf{q} = \frac{6\pi}{c} \hat{c} + q \hat{v}. \quad (\text{A.13})$$

Here the first and second terms correspond, respectively, to the G-type antiferromagnetic order and the incommensuration induced by the  $\mathcal{D}_u$  term. The classical energy  $E_{\text{cl}}$  of this spin configuration is calculated. Each term in the Hamiltonian are calculated as

$$\mathbf{S}_{\mathbf{r}} \cdot \mathbf{S}_{\mathbf{r}+\Delta\mathbf{r}} = S^2 \cos(\phi_{\mathbf{r}+\Delta\mathbf{r}} - \phi_{\mathbf{r}}) = S^2 \cos(\mathbf{Q} \cdot \Delta\mathbf{r}), \quad (\text{A.14})$$

$$(\mathbf{S}_{\mathbf{r}} \times \mathbf{S}_{\mathbf{r}+a\hat{v}})^u = S^2 \sin(\phi_{\mathbf{r}+a\hat{v}} - \phi_{\mathbf{r}}) = S^2 \sin(qa). \quad (\text{A.15})$$

For later convenience, the following expressions are defined:

$$I_{\mathbf{k}} = \sum_{\Delta\mathbf{r}} \mathcal{J}_{\Delta\mathbf{r}} \cos(\mathbf{Q} \cdot \Delta\mathbf{r}) \cos(\mathbf{k} \cdot \Delta\mathbf{r}) - \mathcal{D}_u \sin(\mathbf{Q} \cdot (a\hat{v})) \cos(\mathbf{k} \cdot (a\hat{v})), \quad (\text{A.16})$$

$$J_{\mathbf{k}} = \sum_{\Delta\mathbf{r}} \mathcal{J}_{\Delta\mathbf{r}} \cos(\mathbf{k} \cdot \Delta\mathbf{r}). \quad (\text{A.17})$$

The classical energy is calculated as

$$\begin{aligned} \frac{E_{\text{cl}}}{NS^2} &= I_{\mathbf{0}} = \sum_{\Delta\mathbf{r}} \mathcal{J}_{\Delta\mathbf{r}} \cos(\mathbf{Q} \cdot \Delta\mathbf{r}) - \mathcal{D}_u \sin(\mathbf{Q} \cdot (a\hat{v})) \\ &= -\mathcal{J}(1 + 2\cos\frac{qa}{2}) + \mathcal{J}'(1 + \cos qa + 4\cos\frac{qa}{2}) - \mathcal{D}_u \sin qa \\ &= -3(\mathcal{J} - 2\mathcal{J}') - \mathcal{D}_u qa + \frac{\mathcal{J} - 4\mathcal{J}'}{4}(qa)^2. \end{aligned} \quad (\text{A.18})$$

Minimizing this with respect to  $q$  gives  $qa = \frac{2\mathcal{D}_u}{\mathcal{J} - 4\mathcal{J}'}$  for  $\mathcal{D}_u \ll \mathcal{J}, \mathcal{J}'$ .

### A.3 Canted spin cycloid: $\mathcal{J}$ - $\mathcal{J}'$ - $\mathcal{D}_u$ - $\mathcal{D}_c$ model

Let us add to the Hamiltonian (3.27) the another DM term

$$- \mathcal{D}_c \sum_{\mathbf{r}} (-1)^{m_{\mathbf{r}}} \hat{c} \cdot (\mathbf{S}_{\mathbf{r}} \times \mathbf{S}_{\mathbf{r}+(c/2)\hat{c}}), \quad \text{with } m_{\mathbf{r}} = \frac{\mathbf{r} \cdot \hat{c}}{c/6}, \quad (\text{A.19})$$

where the integer  $m_{\mathbf{r}}$  labels the hexagonal layer in which  $\mathbf{r}$  resides. The following ansatz is assumed for the classical ground state:

$$\begin{pmatrix} S_{\mathbf{r}}^u \\ S_{\mathbf{r}}^v \\ S_{\mathbf{r}}^c \end{pmatrix} = S \begin{pmatrix} (-1)^{m_{\mathbf{r}}} \sin\theta \sin\phi_{\mathbf{r}} \\ -\cos\theta \sin\phi_{\mathbf{r}} \\ \cos\phi_{\mathbf{r}} \end{pmatrix}, \quad \phi_{\mathbf{r}} = \mathbf{Q} \cdot \mathbf{r} + \phi_0, \quad (\text{A.20})$$

which is obtained by tilting the  $vc$  spiral configuration (ground state of (3.27)) around the  $c$ -axis by angles  $(-1)^{m_{\mathbf{r}}}\theta$  alternating along the  $c$  direction. Let us assume the following form for the propagation vector  $\mathbf{Q}$ :

$$\mathbf{Q} = \frac{6\pi}{c}\hat{c} + \mathbf{q} = \frac{6\pi}{c}\hat{c} + q\hat{v}. \quad (\text{A.21})$$

Here the first and second terms correspond, respectively, to the G-type antiferromagnetic order and the incommensuration induced by the  $\mathcal{D}_u$  term. The classical

energy  $E_{\text{cl}}$  of this spin configuration is calculated. Each term in the Hamiltonian is calculated as

$$\mathcal{J} \mathbf{S}_{\mathbf{r}} \cdot \mathbf{S}_{\mathbf{r}+\Delta\mathbf{r}} = \mathcal{J} S^2 [\cos^2 \theta \cos(\mathbf{Q} \cdot \Delta\mathbf{r}) + \sin^2 \theta \cos(\phi_{\mathbf{r}} + \phi_{\mathbf{r}+\Delta\mathbf{r}})], \quad (\text{A.22})$$

$$\mathcal{J}' \mathbf{S}_{\mathbf{r}} \cdot \mathbf{S}_{\mathbf{r}+\Delta\mathbf{r}} = \mathcal{J}' S^2 \cos(\mathbf{Q} \cdot \Delta\mathbf{r}), \quad (\text{A.23})$$

$$\mathcal{D}_u \hat{u} \cdot (\mathbf{S}_{\mathbf{r}} \times \mathbf{S}_{\mathbf{r}+a\hat{v}}) = \mathcal{D}_u S^2 \cos \theta \sin(qa), \quad (\text{A.24})$$

$$\mathcal{D}_c (-1)^{m_{\mathbf{r}}} \hat{c} \cdot (\mathbf{S}_{\mathbf{r}} \times \mathbf{S}_{\mathbf{r}+(c/2)\hat{c}}) = \frac{1}{2} \mathcal{D}_c S^2 \sin(2\theta) [1 - \cos(2\phi_{\mathbf{r}})]. \quad (\text{A.25})$$

Let us first assume that  $\mathbf{Q}$  is incommensurate ( $q > 0$ ). The terms oscillating with  $\mathbf{r}$  disappear when the sum over  $\mathbf{r}$  is taken. The classical energy is then calculated as

$$\begin{aligned} \frac{E_{\text{cl}}}{NS^2} &= -\mathcal{J} \cos^2 \theta \left(1 + 2 \cos \frac{qa}{2}\right) \\ &+ \mathcal{J}' \left(1 + \cos qa + 4 \cos \frac{qa}{2}\right) - \mathcal{D}_u \cos \theta \sin qa - \frac{1}{2} \mathcal{D}_c \sin 2\theta. \end{aligned} \quad (\text{A.26})$$

Taylor-expanding up to second order in terms of  $qa$  and  $\theta$  gives

$$\frac{E_{\text{cl}}}{NS^2} = -3(\mathcal{J} - 2\mathcal{J}') - \mathcal{D}_u qa + \frac{\mathcal{J} - 4\mathcal{J}'}{4} (qa)^2 - \mathcal{D}_c \theta + 3\mathcal{J}\theta^2. \quad (\text{A.27})$$

This is minimized at

$$qa = \frac{2\mathcal{D}_u}{\mathcal{J} - 4\mathcal{J}'}, \quad \theta = \frac{\mathcal{D}_c}{6\mathcal{J}}, \quad (\text{A.28})$$

leading to the energy

$$\left(\frac{E_{\text{cl}}}{NS^2}\right)_{\text{IC}} = -3(\mathcal{J} - 2\mathcal{J}') - \mathcal{D}_u qa - \frac{\mathcal{D}_u^2}{\mathcal{J} - 4\mathcal{J}'} - \frac{\mathcal{D}_c^2}{12\mathcal{J}}. \quad (\text{A.29})$$

On the other hand, suppose that  $\mathbf{Q}$  is commensurate ( $q = 0$ ). In contrast to the incommensurate case above, the following terms have non-zero contributions:

$$\sum_{\mathbf{r}} \cos(\phi_{\mathbf{r}} + \phi_{\mathbf{r}+\Delta\mathbf{r}}) = -N \cos(2\phi_0), \quad \sum_{\mathbf{r}} \cos(2\phi_{\mathbf{r}}) = N \cos(2\phi_0). \quad (\text{A.30})$$

The classical energy is then calculated as

$$\begin{aligned} \frac{E_{\text{cl}}}{NS^2} &= -3(\mathcal{J} - 2\mathcal{J}') + \left[3\mathcal{J} \sin^2 \theta - \frac{1}{2} \mathcal{D}_c \sin(2\theta)\right] [1 - \cos(2\phi_0)] \\ &\simeq -3(\mathcal{J} - 2\mathcal{J}') + (3\mathcal{J}\theta^2 - \mathcal{D}_c \theta) [1 - \cos(2\phi_0)]. \end{aligned} \quad (\text{A.31})$$

In the last line, the Taylor expansion is performed in terms of  $\theta$ . Setting  $\theta = \mathcal{D}_c/(6\mathcal{J})$  and  $\phi_0 = \pm\pi/2$ , the energy takes the minimum

$$\left(\frac{E_{\text{cl}}}{NS^2}\right)_{\text{C}} = -3(\mathcal{J} - 2\mathcal{J}') - \mathcal{D}_u qa - \frac{\mathcal{D}_c^2}{6\mathcal{J}}. \quad (\text{A.32})$$

The spin configuration in this ground state shows the weak ferromagnetism as observed in thin films.

In order for the incommensurate state to be realized in the bulk, the following inequality must be satisfied:

$$0 < \left(\frac{E_{\text{cl}}}{NS^2}\right)_{\text{C}} - \left(\frac{E_{\text{cl}}}{NS^2}\right)_{\text{IC}} = \frac{\mathcal{D}_u^2}{\mathcal{J} - 4\mathcal{J}'} - \frac{\mathcal{D}_c^2}{12\mathcal{J}}, \quad (\text{A.33})$$

namely,

$$\left(\frac{\mathcal{D}_u}{\mathcal{D}_c}\right)^2 > \frac{\mathcal{J} - 4\mathcal{J}'}{12\mathcal{J}}. \quad (\text{A.34})$$

For the measured value of  $\mathcal{D}_u = 0.11$ , the upper bound of  $\mathcal{D}_c$  is

$$\mathcal{D}_c < \mathcal{D}_u \sqrt{\frac{12\mathcal{J}}{\mathcal{J} - 4\mathcal{J}'}} = 0.41 \text{ meV}. \quad (\text{A.35})$$

Using (A.28), this condition can be rewritten as

$$\frac{\mathcal{J}'}{\mathcal{J}} < \frac{1}{4} - 3 \left(\frac{\theta}{qa}\right)^2. \quad (\text{A.36})$$

According to experiments, the period of the incommensuration is  $620 \text{ \AA}$  and  $\mathcal{J}'/\mathcal{J} = 0.034$ . Then an upper bound on  $\theta$

$$\theta < qa \sqrt{\frac{1}{12} - \frac{\mathcal{J}'}{3\mathcal{J}}} = 0.015 = 0.87^\circ. \quad (\text{A.37})$$

Therefore, the spin canting of angle  $\approx 1^\circ$  observed in SANS experiment [56] on bulk samples may thus be an overestimate. In thin films, on the other hand, weak ferromagnetism is observed rather than the cycloid, implying that the above conditions are violated. This may reflect an increase of the Dzyaloshinskii-Moriya interaction due to the greater structure distortions imposed by the epitaxial strains. However, an increase shape anisotropy may also play a role in destroying the cycloid, so further development of the current model is needed to elucidate the

different effects of  $\mathcal{D}_c$  and  $\mathcal{K}$ .

#### A.4 Anharmonic spin cycloid: $\mathcal{J}$ - $\mathcal{J}'$ - $\mathcal{D}_u$ - $\mathcal{K}$ model

If instead of  $\mathcal{D}_c$ , the single-ion anisotropy term,

$$-\mathcal{K} \sum_{\mathbf{r}} (S_{\mathbf{r}}^c)^2 \quad (\text{A.38})$$

is added to the Hamiltonian (3.27). The classical ground state is assumed to be

$$\mathbf{S}_{\mathbf{r}} = \begin{pmatrix} S_{\mathbf{r}}^u \\ S_{\mathbf{r}}^v \\ S_{\mathbf{r}}^c \end{pmatrix} = R_u(\phi_{\mathbf{r}}) \begin{pmatrix} 0 \\ 0 \\ S \end{pmatrix} = \begin{pmatrix} 0 \\ -S \sin \phi_{\mathbf{r}} \\ S \cos \phi_{\mathbf{r}} \end{pmatrix}, \quad \phi_{\mathbf{r}} = \mathbf{Q} \cdot \mathbf{r} + \phi_0 + \psi_{\mathbf{r}}, \quad (\text{A.39})$$

where  $\psi_{\mathbf{r}}$  is a modulation angle (from a perfect spin cycloid) caused by the  $\mathcal{K}$  term. Here,  $|\psi_{\mathbf{r}}| \ll 1$  is assumed.

Let us calculate the classical ground-state energy  $E_{\text{cl}}$ . Each term in the Hamiltonian is calculated as

$$\begin{aligned} \mathbf{S}_{\mathbf{r}} \cdot \mathbf{S}_{\mathbf{r}+\Delta\mathbf{r}} &= S^2 \cos(\phi_{\mathbf{r}+\Delta\mathbf{r}} - \phi_{\mathbf{r}}) = S^2 \cos(\mathbf{Q} \cdot \Delta\mathbf{r} + \psi_{\mathbf{r}+\Delta\mathbf{r}} - \psi_{\mathbf{r}}) \\ &\approx S^2 \cos(\mathbf{Q} \cdot \Delta\mathbf{r}) \left[ 1 - \frac{1}{2}(\psi_{\mathbf{r}+\Delta\mathbf{r}} - \psi_{\mathbf{r}})^2 \right] \\ &\quad - S^2 \sin(\mathbf{Q} \cdot \Delta\mathbf{r})(\psi_{\mathbf{r}+\Delta\mathbf{r}} - \psi_{\mathbf{r}}), \end{aligned} \quad (\text{A.40})$$

$$\begin{aligned} \hat{u} \cdot (\mathbf{S}_{\mathbf{r}} \times \mathbf{S}_{\mathbf{r}+a\hat{v}}) &= S^2 \sin(\phi_{\mathbf{r}+a\hat{v}} - \phi_{\mathbf{r}}) = S^2 \sin(qa + \psi_{\mathbf{r}+a\hat{v}} - \psi_{\mathbf{r}}) \\ &\approx S^2 \sin(qa) \left[ 1 - \frac{1}{2}(\psi_{\mathbf{r}+a\hat{v}} - \psi_{\mathbf{r}})^2 \right] + \cos(qa)(\psi_{\mathbf{r}+a\hat{v}} - \psi_{\mathbf{r}}), \end{aligned} \quad (\text{A.41})$$

$$\begin{aligned} (S_{\mathbf{r}}^c)^2 &= S^2 \cos^2 \phi_{\mathbf{r}} = \frac{S^2}{2} [1 + \cos(2\phi_{\mathbf{r}})] = \frac{S^2}{2} [1 + \cos(2\mathbf{Q} \cdot \mathbf{r} + 2\phi_0 + 2\psi_{\mathbf{r}})] \\ &\approx \frac{S^2}{2} \left[ 1 + \cos(2\mathbf{Q} \cdot \mathbf{r} + 2\phi_0) \left[ 1 - \frac{1}{2}(2\psi_{\mathbf{r}})^2 \right] - \sin(2\mathbf{Q} \cdot \mathbf{r} + 2\phi_0) \cdot (2\psi_{\mathbf{r}}) \right]. \end{aligned} \quad (\text{A.42})$$

Summing these over  $\mathbf{r}$ , let us take the Fourier transform on  $\psi_{\mathbf{r}}$  as

$$\psi_{\mathbf{r}} = \frac{1}{\sqrt{N}} \sum_{\mathbf{k} \neq \mathbf{0}} e^{i\mathbf{k} \cdot \mathbf{r}} \psi_{\mathbf{k}}, \quad (\text{A.43})$$

where the  $\mathbf{k} = \mathbf{0}$  term is excluded since it can be absorbed into  $\phi_0$ . Using

$$\begin{aligned} \frac{1}{2} \sum_{\mathbf{r}} (\psi_{\mathbf{r}+\Delta\mathbf{r}} - \psi_{\mathbf{r}})^2 &= \frac{1}{2} \sum_{\mathbf{k}} (e^{i\mathbf{k}\cdot\Delta\mathbf{r}} - 1)(e^{-i\mathbf{k}\cdot\Delta\mathbf{r}} - 1)\psi_{\mathbf{k}}\psi_{-\mathbf{k}} \\ &= \sum_{\mathbf{k}} (1 - \cos(\mathbf{k} \cdot \Delta\mathbf{r}))\psi_{\mathbf{k}}\psi_{-\mathbf{k}}, \end{aligned} \quad (\text{A.44})$$

$$\sum_{\mathbf{r}} \cos(2\mathbf{Q} \cdot \mathbf{r} + 2\phi_0) (\psi_{\mathbf{r}})^2 = \frac{1}{2} \sum_{\mathbf{k}} (e^{i2\phi_0}\psi_{\mathbf{k}-2\mathbf{Q}}\psi_{-\mathbf{k}} + e^{-i2\phi_0}\psi_{\mathbf{k}+2\mathbf{Q}}\psi_{-\mathbf{k}}), \quad (\text{A.45})$$

$$\sum_{\mathbf{r}} \sin(2\mathbf{Q} \cdot \mathbf{r} + 2\phi_0) \cdot \psi_{\mathbf{r}} = \frac{\sqrt{N}}{2i} (e^{i2\phi_0}\psi_{-2\mathbf{Q}} - e^{-i2\phi_0}\psi_{2\mathbf{Q}}), \quad (\text{A.46})$$

the following expressions are found:

$$\sum_{\mathbf{r}} \mathbf{S}_{\mathbf{r}} \cdot \mathbf{S}_{\mathbf{r}+\Delta\mathbf{r}} \approx S^2 \cos(\mathbf{Q} \cdot \Delta\mathbf{r}) \left[ N - \sum_{\mathbf{k}} \{1 - \cos(\mathbf{k} \cdot \Delta\mathbf{r})\} \psi_{\mathbf{k}}\psi_{-\mathbf{k}} \right], \quad (\text{A.47})$$

$$\sum_{\mathbf{r}} \hat{u} \cdot (\mathbf{S}_{\mathbf{r}} \times \mathbf{S}_{\mathbf{r}+a\hat{v}}) \approx S^2 \sin(qa) \left[ N - \sum_{\mathbf{k}} \{1 - \cos(\mathbf{k} \cdot (a\hat{v}))\} \psi_{\mathbf{k}}\psi_{-\mathbf{k}} \right], \quad (\text{A.48})$$

$$\begin{aligned} \sum_{\mathbf{r}} (S_{\mathbf{r}}^c)^2 &= \frac{S^2}{2} \left[ N + \sum_{\mathbf{k}} (e^{i2\phi_0}\psi_{\mathbf{k}-2\mathbf{Q}}\psi_{-\mathbf{k}} + e^{-i2\phi_0}\psi_{\mathbf{k}+2\mathbf{Q}}\psi_{-\mathbf{k}}) \right. \\ &\quad \left. - \frac{\sqrt{N}}{2i} (e^{i2\phi_0}\psi_{-2\mathbf{Q}} - e^{-i2\phi_0}\psi_{2\mathbf{Q}}) \right] \end{aligned} \quad (\text{A.49})$$

The classical energy is thus calculated as

$$\begin{aligned} \frac{E_{\text{cl}}}{S^2} &= NI_0 + \sum_{\mathbf{k}} (I_{\mathbf{k}} - I_0)\psi_{\mathbf{k}}\psi_{-\mathbf{k}} \\ &\quad - \frac{K}{2} \sum_{\mathbf{k}} (e^{i2\phi_0}\psi_{\mathbf{k}-2\mathbf{Q}}\psi_{-\mathbf{k}} + e^{-i2\phi_0}\psi_{\mathbf{k}+2\mathbf{Q}}\psi_{-\mathbf{k}}) \\ &\quad + \frac{\sqrt{N}K}{2i} (e^{i2\phi_0}\psi_{-2\mathbf{Q}} - e^{-i2\phi_0}\psi_{2\mathbf{Q}}) - \frac{NK}{2}. \end{aligned} \quad (\text{A.50})$$

Minimizing this with respect to  $\{\psi_{\mathbf{r}}\}$ ,

$$\begin{aligned}
 0 &= \frac{\partial}{\partial \psi_{-\mathbf{k}}} \left( \frac{E_{\text{cl}}}{S^2} \right) \\
 &= 2(I_{\mathbf{k}} - I_0)\psi_{\mathbf{k}} - K(e^{i2\phi_0}\psi_{\mathbf{k}-2\mathbf{Q}} + e^{-i2\phi_0}\psi_{\mathbf{k}+2\mathbf{Q}}) \\
 &\quad + \frac{\sqrt{N}K}{2i}(e^{i2\phi_0}\delta_{\mathbf{k},2\mathbf{Q}} - e^{-i2\phi_0}\delta_{\mathbf{k},-2\mathbf{Q}}).
 \end{aligned} \tag{A.51}$$

Ignoring the second term,

$$\psi_{\pm 2\mathbf{Q}} = -\sqrt{N} \frac{\pm K}{4i(I_{2\mathbf{Q}} - I_0)} e^{\pm i2\phi_0}, \quad \psi_{\mathbf{k}} = 0 \quad (\mathbf{k} \neq \pm 2\mathbf{Q}). \tag{A.52}$$

This result means that the modulation angle  $\psi_{\mathbf{r}}$  is given by

$$\psi_{\mathbf{r}} = -\frac{K}{2(I_{2\mathbf{Q}} - I_0)} \sin(2\mathbf{Q} \cdot \mathbf{r} + 2\phi_0), \tag{A.53}$$

where

$$\begin{aligned}
 I_0 &= \sum_{\Delta\mathbf{r}} \mathcal{J}_{\Delta\mathbf{r}} \cos(\mathbf{Q} \cdot \Delta\mathbf{r}) - \mathcal{D}_u \sin(\mathbf{Q} \cdot (a\hat{v})) \\
 &= -\mathcal{J}(1 + 2\cos\frac{qa}{2}) + \mathcal{J}'(1 + \cos qa + 4\cos\frac{qa}{2}) - \mathcal{D}_u \sin qa \\
 &\approx -3(\mathcal{J} - 2\mathcal{J}') - \mathcal{D}_u qa + \frac{\mathcal{J} - 4\mathcal{J}'}{4}(qa)^2
 \end{aligned} \tag{A.54}$$

$$\begin{aligned}
 I_{2\mathbf{Q}} - I_0 &= \sum_{\Delta\mathbf{r}} \mathcal{J}_{\Delta\mathbf{r}} \cos(\mathbf{Q} \cdot \Delta\mathbf{r}) [\cos(2\mathbf{Q} \cdot \Delta\mathbf{r}) - 1] \\
 &\quad - \mathcal{D}_u \sin(\mathbf{Q} \cdot (a\hat{v})) [\cos(2\mathbf{Q} \cdot (a\hat{v})) - 1] \\
 &= -2\mathcal{J} \cos\frac{qa}{2} (\cos qa - 1) \\
 &\quad + \mathcal{J}' \left[ \cos qa (\cos 2qa - 1) + 4\cos\frac{qa}{2} (\cos qa - 1) \right] \\
 &\quad - \mathcal{D}_u \sin qa (\cos 2qa - 1) \\
 &\approx (\mathcal{J} - 4\mathcal{J}')(qa)^2
 \end{aligned} \tag{A.55}$$

Therefore, in order to validate the initial assumption  $|\psi_{\mathbf{r}}| \ll 1$ , the condition  $\mathcal{K} \ll 2(\mathcal{J} - 4\mathcal{J}')(qa)^2$  must be satisfied. Using the experimental values  $\mathcal{J} = 4.38$ ,  $\mathcal{J}' = 0.15$  meV and  $qa = 0.0565$ ,  $2(\mathcal{J} - 4\mathcal{J}')(qa)^2 \approx 0.0285$ . The assumption is

valid for the measured value of  $\mathcal{K} = 0.0033$ .

Next let us determine the incommensuration pitch  $q$ . Inserting (A.52) into (A.50) yields

$$\begin{aligned}
\frac{E_{\text{cl}}}{NS^2} &= I_0 + 2(I_{2\mathbf{Q}} - I_0) \frac{1}{N} \psi_{2\mathbf{Q}} \psi_{-2\mathbf{Q}} + \frac{\mathcal{K}}{2i\sqrt{N}} (e^{i2\phi_0} \psi_{-2\mathbf{Q}} - e^{-i2\phi_0} \psi_{2\mathbf{Q}}) - \frac{\mathcal{K}}{2} \\
&= I_0 + 2(I_{2\mathbf{Q}} - I_0) \left( \frac{\mathcal{K}}{4(I_{2\mathbf{Q}} - I_0)} \right)^2 - \frac{\mathcal{K}}{2} \cdot 2 \cdot \frac{\mathcal{K}}{4(I_{2\mathbf{Q}} - I_0)} - \frac{\mathcal{K}}{2} \\
&= I_0 - \frac{\mathcal{K}^2}{8(I_{2\mathbf{Q}} - I_0)} - \frac{\mathcal{K}}{2}.
\end{aligned} \tag{A.56}$$

Since

$$I_0 = \mathcal{O}(\mathcal{J}(qa)^2), \quad \frac{\mathcal{K}^2}{I_0 - I_{2\mathbf{Q}}} = \mathcal{O}\left(\frac{\mathcal{K}^2}{\mathcal{J}(qa)^2}\right), \tag{A.57}$$

the second term of (A.56) may be neglected as long as the condition  $\mathcal{K} \ll 2(\mathcal{J} - 4\mathcal{J}')(qa)^2$  introduced above is satisfied. Therefore,  $\mathcal{K} = 0.002\text{--}0.004$  meV does not change  $qa$  much, in contrary to ref. [82]. For further convenience,  $qa$  is rather fixed to the experimental value and the model parameters are tuned so that the desired value of  $qa$  is obtained.

## A.5 Anharmonicity of spin cycloid

In order to obtain the anharmonicity of the spin cycloid, I focus on the derivative ( $\nabla L_i$ ) and the anisotropy terms, and ignore the small canting out of the cycloid plane. The corresponding Landau-Ginzburg free energy density can be then written as

$$\begin{aligned}
f &= f_{\text{exch}} + f_{\text{L}} + f_{\text{an}} \\
&= A \sum_{i=x,y,z} (\nabla l_i)^2 - \alpha \mathbf{P} \cdot [\mathbf{l}(\nabla \cdot \mathbf{l}) + \mathbf{l} \times (\nabla \times \mathbf{l})] - K_u l_z^2,
\end{aligned} \tag{A.58}$$

where  $M_0$  is the magnitude of the magnetization vector  $\mathbf{M}_i$  of the sublattices,  $\mathbf{P}$  is the spontaneous polarization vector, and  $\mathbf{l} = (\mathbf{M}_1 - \mathbf{M}_2)/2M_0$  is the antiferromagnetic unit vector. The first term is an exchange interaction term with the inhomogeneous exchange constant  $A$  (exchange stiffness), the second term is the Lifshitz invariant term with the inhomogeneous magnetoelectric (flexomagneto-

electric) interaction constant  $\alpha$ , and the last term is an uniaxial anisotropy term with the magnetic anisotropy constant  $K_u$ .

Let  $\mathbf{l} = (\sin \theta \cos \phi, \sin \theta \sin \phi, \cos \theta)$ , so each term can be written as

$$f_{\text{exch}} = A \sum_{i,j} (\partial_i l_j)^2 = A \left[ (\nabla \theta)^2 + \sin^2 \theta (\nabla \phi)^2 \right], \quad (\text{A.59})$$

$$\begin{aligned} f_{\text{L}} &= \alpha P_z (l_x \partial_x l_z + l_y \partial_y l_z - l_z \partial_x l_x - l_z \partial_y l_y) \\ &= -\alpha P_z [\cos \phi (\partial_x \theta) + \sin \phi (\partial_y \theta) \\ &\quad - \sin \theta \cos \theta (\sin \phi (\partial_x \phi) - \cos \phi (\partial_y \phi))], \end{aligned} \quad (\text{A.60})$$

$$f_{\text{an}} = -K_u l_z^2 = -K_u \cos^2 \theta. \quad (\text{A.61})$$

The Euler-Lagrange equations for  $f(\theta, \phi, \partial_i \theta, \partial_i \phi)$  can be derived as

$$\begin{aligned} 2A (\nabla^2 \theta) + 2\alpha P_z \sin^2 \theta (\sin \phi (\partial_x \phi) - \cos \phi (\partial_y \phi)) \\ - \sin 2\theta (A (\nabla \phi)^2 + K_u) = 0, \end{aligned} \quad (\text{A.62})$$

$$2A \nabla \cdot (\sin^2 \theta (\nabla \phi)) - 2\alpha P_z \sin^2 \theta (\sin \phi (\partial_x \theta) - \cos \phi (\partial_y \theta)) = 0. \quad (\text{A.63})$$

The solutions are

$$\nabla \phi = \mathbf{0}, \quad \sin \phi (\partial_x \theta) - \cos \phi (\partial_y \theta) = 0 \quad (\text{A.64})$$

$$\phi = \text{const} = \arctan \left( \frac{\partial_y \theta}{\partial_x \theta} \right) \quad (\text{A.65})$$

$$2A (\nabla^2 \theta) - K_u \sin 2\theta = 0. \quad (\text{A.66})$$

The solution gives a cycloid spin structure on the plane defined by the  $z$ -axis and a direction in the  $xy$ -plane. The coordinate dependence of the angle  $\theta$  generally exhibits a nonlinear behavior due to equation A.66. By rotating the coordinate system, so that  $\theta(x, y) = \theta(r)$ , i.e., the cycloid lies in the  $rz$ -plane, it can be rewritten as

$$2A \frac{d^2 \theta}{dr^2} - K_u \sin 2\theta = 0. \quad (\text{A.67})$$

This is the sine-Gordon equation for a nonlinear oscillator, which has two different solutions depending on the sign of  $K_u$ .

$$\varphi = \begin{cases} \theta, & K_u < 0 \\ \theta + \frac{\pi}{2}, & K_u > 0 \end{cases}. \quad (\text{A.68})$$

In both cases, the equation can be reduced to

$$\frac{d^2\varphi}{dr^2} + \frac{\varepsilon}{2} \sin 2\varphi = 0 \quad (\text{A.69})$$

where  $\varepsilon = |K_u|/A$ . Then the solution is obtained by integrating this, as follows

$$\left(\frac{d\varphi}{dr}\right)^2 + \varepsilon \sin^2\varphi = C, \quad (\text{A.70})$$

$$\frac{d\varphi}{dr} = \pm \sqrt{\frac{\varepsilon}{m}} \sqrt{1 - m \sin^2\varphi}, \quad (\text{A.71})$$

$$r(\varphi) = \pm \sqrt{\frac{m}{\varepsilon}} F(\varphi, m), \quad (\text{A.72})$$

where  $C$  is the constant of integration,  $m \equiv \varepsilon/C = |K_u|/AC$  and  $F(\theta, m) = \int_0^\theta \frac{d\theta'}{\sqrt{1 - m \sin^2\theta'}}$  is the incomplete elliptic integral of the first kind with the parameter  $m$ . The period of the cycloid is

$$\lambda = r(2\pi) - r(0) = 4\sqrt{\frac{m}{\varepsilon}} K(m), \quad (\text{A.73})$$

where  $K(m) = F(\frac{\pi}{2}, m) = \int_0^{\pi/2} \frac{d\theta}{\sqrt{1 - m \cos^2\theta}}$  is the complete elliptic integral of the first kind. The anharmonicity parameter  $m$  can be obtained from this relation for given  $\varepsilon$  and  $\lambda$ . Note that  $m = 0$  for  $K_u = 0$  and it approaches 1 for  $|K_u| \gg A$ .

The angle  $\varphi$  can be expressed by the Jacobi amplitude as the inverse of the incomplete elliptic integral,

$$\varphi(r) = F^{-1}\left(\pm \sqrt{\frac{\varepsilon}{m}} r, m\right) = \pm \text{am}\left(\sqrt{\frac{\varepsilon}{m}} r, m\right). \quad (\text{A.74})$$

The two possible signs correspond to the winding direction of spins in the cycloid. Choosing a positive sign,

$$\theta(r) = \begin{cases} \text{am}\left(\sqrt{\frac{|K_u|}{Am}} r, m\right), & K_u < 0 \\ \text{am}\left(\sqrt{\frac{K_u}{Am}} r, m\right) - \frac{\pi}{2}, & K_u > 0 \end{cases}. \quad (\text{A.75})$$

The shape of the anharmonic cycloid can be obtained in terms of the Jacobi

elliptic function,

$$\frac{L_z}{L} = \cos \varphi = \operatorname{cn} \left( \sqrt{\frac{\varepsilon}{m}} r, m \right) \quad (\text{A.76})$$

$$\frac{L_r}{L} = \sin \varphi = \operatorname{sn} \left( \sqrt{\frac{\varepsilon}{m}} r, m \right) \quad (\text{A.77})$$

for the easy-plane anisotropy ( $K_u < 0$ ) and

$$\frac{L_z}{L} = \cos \left( \varphi - \frac{\pi}{2} \right) = \operatorname{sn} \left( \sqrt{\frac{\varepsilon}{m}} r, m \right) \quad (\text{A.78})$$

$$\frac{L_r}{L} = \sin \left( \varphi - \frac{\pi}{2} \right) = -\operatorname{cn} \left( \sqrt{\frac{\varepsilon}{m}} r, m \right) \quad (\text{A.79})$$

for the easy-axis anisotropy ( $K_u > 0$ ). It can be rewritten with  $\lambda$  using the relation A.73 as

$$\frac{L_z}{L} = \operatorname{cn} \left( \frac{4\mathbf{K}(m)}{\lambda} r, m \right), \quad \frac{L_r}{L} = \operatorname{sn} \left( \frac{4\mathbf{K}(m)}{\lambda} r, m \right) \quad (\text{A.80})$$

for the easy-plane anisotropy and

$$\frac{L_z}{L} = \operatorname{sn} \left( \frac{4\mathbf{K}(m)}{\lambda} r, m \right), \quad \frac{L_r}{L} = -\operatorname{cn} \left( \frac{4\mathbf{K}(m)}{\lambda} r, m \right) \quad (\text{A.81})$$

for the easy-axis anisotropy.

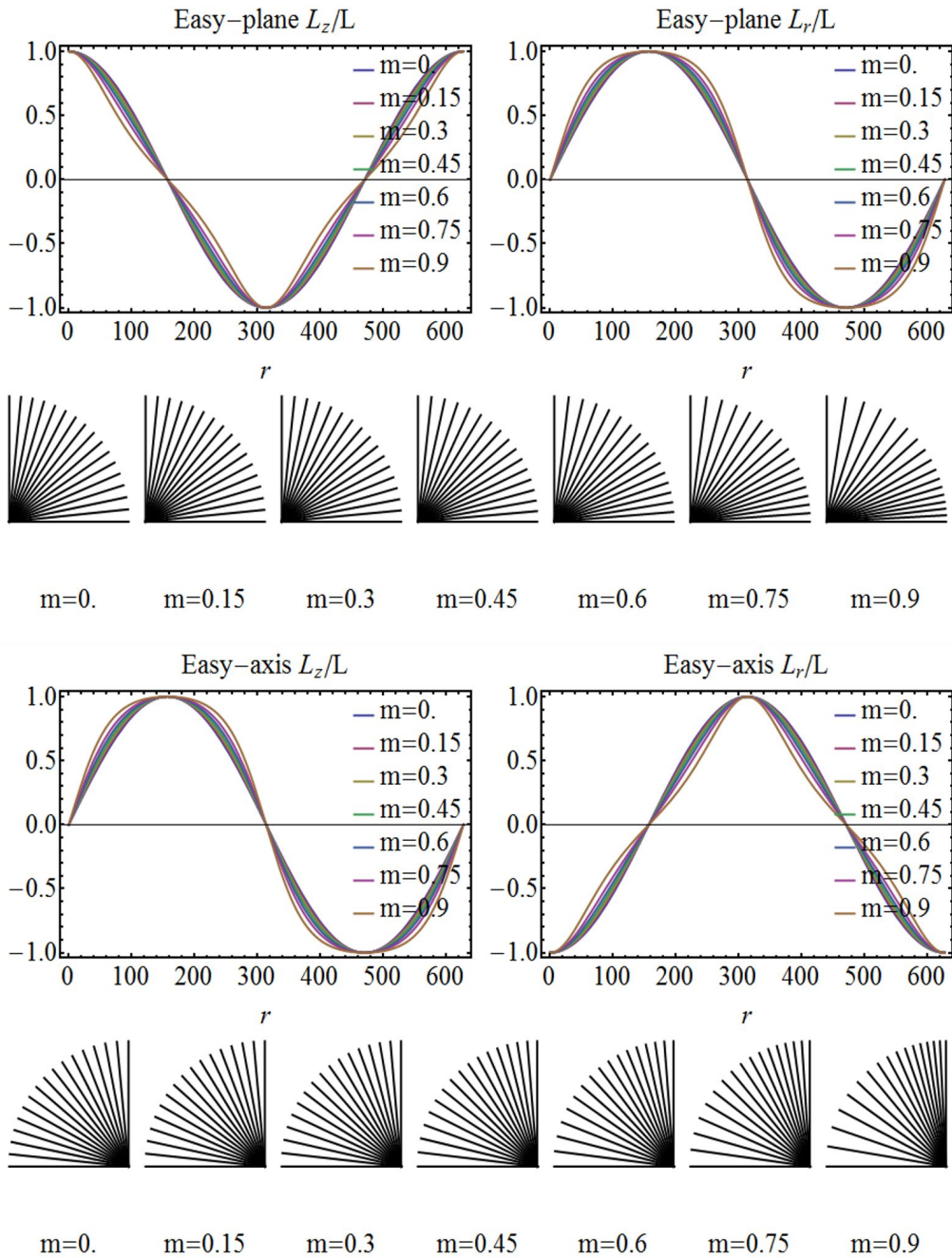


Figure A.1: Anharmonicity of spin cycloid with an easy-plane and easy-axis anisotropy.



## Appendix B. Equivalence of L-G free energy and spin Hamiltonian

To compare the spin Hamiltonian 3.2 with the L-G free energy 3.1, let us consider the classical (magnetic) ground state and the corresponding energy. When the exchange interaction is dominant and the DM term is negligible, the ground state is a collinear order. Considering the collinear state, the ground state energy obtained from the spin Hamiltonian and the free energy are

$$\begin{aligned} \mathcal{H} &= \sum_{\mathbf{r}} \left[ \sum_{\Delta} \mathcal{J}_{\Delta} \mathbf{S}_{\mathbf{r}} \cdot \mathbf{S}_{\mathbf{r}+\Delta} - \mathcal{K} (\mathbf{S}_{\mathbf{r}} \cdot \hat{\mathbf{c}})^2 \right] \\ &= NS^2 (-3\mathcal{J} + 6\mathcal{J}' - \mathcal{K} \cos^2 \theta), \end{aligned} \quad (\text{B.1})$$

$$F = \int dV [\lambda \mathbf{l}^2 - K_u l_c^2] = V (\lambda - K_u \cos^2 \theta), \quad (\text{B.2})$$

where  $M_0$  is the magnitude of the magnetization vector  $\mathbf{M}_i$  of sublattices,  $\mathbf{l} = (\mathbf{M}_1 - \mathbf{M}_2)/2M_0$  is the antiferromagnetic unit vector and  $\theta$  is the angle between  $\mathbf{l}$  and the  $c$ -axis. Clearly,  $\lambda < 0$  or  $\mathcal{J} > 0$  for the AFM ground state and  $\theta = 0$  for an easy-axis anisotropy  $K_u > 0$  or  $\mathcal{K} > 0$ . Here, we can find the relations

$$V\lambda = NS^2 (-3\mathcal{J} + 6\mathcal{J}'), \quad (\text{B.3})$$

$$VK_u = NS^2 \mathcal{K}. \quad (\text{B.4})$$

The DM interaction favours a magnetic cycloid. If the small canting out of the cycloid plane and the SIA are ignored, the ground state is a harmonic cycloid that lies on the  $vc$ -plane. Considering the harmonic cycloid with

$$\mathbf{S}_{\mathbf{r}} = S (0, \sin \theta_{\mathbf{r}}, \cos \theta_{\mathbf{r}}), \quad \theta_{\mathbf{r}} = \theta_0 + \mathbf{Q} \cdot \mathbf{r}, \quad (\text{B.5})$$

where  $\mathbf{Q} = \mathbf{Q}_G + \mathbf{Q}_m = (0.0045, 0.0045, 3)$ , the ground state energies are

$$\begin{aligned} \mathcal{H} &= \sum_{\mathbf{r}, \Delta} \mathcal{J}_\Delta \mathbf{S}_\mathbf{r} \cdot \mathbf{S}_{\mathbf{r}+\Delta} - \sum_{\mathbf{r}} \mathcal{D}_u \hat{\mathbf{u}} \cdot (\mathbf{S}_\mathbf{r} \times \mathbf{S}_{\mathbf{r}+a\hat{\mathbf{v}}}) \\ &= NS^2 \left[ -\mathcal{J} \left( 1 + 2 \cos \frac{\Delta\theta}{2} \right) \right. \\ &\quad \left. + \mathcal{J}' \left( 1 + 4 \cos \frac{\Delta\theta}{2} + \cos \Delta\theta \right) + \mathcal{D}_u \sin \Delta\theta \right] \\ &\approx NS^2 \left[ (-3\mathcal{J} + 6\mathcal{J}') + \frac{\mathcal{J} - 4\mathcal{J}'}{4} a^2 (d_v\theta)^2 + \mathcal{D}_u a (d_v\theta) \right], \end{aligned} \quad (\text{B.6})$$

$$\begin{aligned} F &= \int dV \left[ \lambda \mathbf{l}^2 + A \sum_i (\nabla l_i)^2 - \alpha \mathbf{P} \cdot [\mathbf{l}(\nabla \cdot \mathbf{l}) + \mathbf{l} \times (\nabla \times \mathbf{l})] \right] \\ &= V \left[ \lambda + A (d_v\theta)^2 - \alpha P_z (d_v\theta) \right], \end{aligned} \quad (\text{B.7})$$

where  $\Delta\theta = \theta_{\mathbf{r}+a\hat{\mathbf{v}}} - \theta_{\mathbf{r}} = a(d_v\theta)$  is the angle difference between spins along the cycloid direction  $[1 \ 1 \ 0]_{\text{hex}}$  and  $\mathbf{P}$  is the spontaneous polarization vector. Note that  $\alpha > 0$  or  $\mathcal{D}_u < 0$  for the clockwise rotation and  $\alpha < 0$  or  $\mathcal{D}_u > 0$  for the counterclockwise. Now, we can find the relations

$$VA = NS^2 a^2 \left( \frac{\mathcal{J} - 4\mathcal{J}'}{4} \right), \quad (\text{B.8})$$

$$V\alpha P_z = -NS^2 a \mathcal{D}_u. \quad (\text{B.9})$$

The terms responsible for the canting out of the cycloid plane are

$$\mathcal{H}_{\text{DM}}^c = - \sum_{\mathbf{r}} (-1)^{\frac{6}{5}\mathbf{r} \cdot \hat{\mathbf{c}}} \mathcal{D}_c \hat{\mathbf{c}} \cdot (\mathbf{S}_\mathbf{r} \times \mathbf{S}_{\mathbf{r}+\frac{c}{2}\hat{\mathbf{c}}}), \quad (\text{B.10})$$

$$F_{\text{DM}} = - \int dV 2\beta M_0 \mathbf{P} \cdot (\mathbf{m} \times \mathbf{l}), \quad (\text{B.11})$$

where  $\mathbf{m} = (\mathbf{M}_1 + \mathbf{M}_2)/2M_0$  is the magnetization unit vector. Note that these vanish without a local ferromagnetic moment  $\mathbf{m}$ . The ground state is the canted cycloid

$$\frac{\mathbf{M}_1}{M_0} = \begin{pmatrix} \sin \Phi \sin \theta \\ \cos \Phi \sin \theta \\ \cos \theta \end{pmatrix}, \quad \frac{\mathbf{M}_2}{M_0} = \begin{pmatrix} \sin \Phi \sin \theta \\ -\cos \Phi \sin \theta \\ -\cos \theta \end{pmatrix}, \quad (\text{B.12})$$

---

where  $\Phi$  is the canting angle and  $\theta$  is the rotation angle on the cycloid plane. Whilst the ground state energy corresponding to other terms previously discussed are also changed in this state, the differences may be ignored for small  $\Phi \ll 1$ . The classical energies are now

$$\begin{aligned}\mathcal{H}_{\text{DM}}^c &= - \sum_{\mathbf{r}} \mathcal{D}_c \sin \left( \phi_{\mathbf{r} + \frac{c}{2} \hat{\mathbf{c}}} - \phi_{\mathbf{r}} \right) \sin^2 \theta_{\mathbf{r}} \\ &= \sum_{\mathbf{r}} \mathcal{D}_c \sin 2\Phi \sin^2 \theta_{\mathbf{r}},\end{aligned}\tag{B.13}$$

$$\begin{aligned}F_{\text{DM}} &= - \int dV 2\beta M_0 P_z \sin \Phi \cos \Phi \sin^2 \theta \\ &= - \int dV \beta M_0 P_z \sin 2\Phi \sin^2 \theta,\end{aligned}\tag{B.14}$$

so that we can find the relation

$$V \beta M_0 P_z = N S^2 \mathcal{D}_c.\tag{B.15}$$



# Appendix C. Codes for the detector trajectory

To simulate detector trajectory in elastic scattering, I made a Mathematica code *DT-elastic.nb*.

```

1 Module[
2 {RM, k, Ki, Kf, dK, mdsc, trsc, lambda, Ei, a, axes, fs}, (* Localized variables *)
3 RM := RotationMatrix[# Degree] &;
4 Ki = {1, 0}; Kf = RM[#].Ki &; dK = Ki - Kf[#] &;
5 mdsc = 2; axes = 2 trsc {Ki, Kf[60], Kf[-60]};
6 fs = 25;
7
8 CreateDialog[
9 Manipulate[
10 k = 2 Pi/lambda; trsc = k/a;
11 Row[{
12 (* Upper panel: Configuration of sample and detector *)
13 Show[
14 Graphics[{
15 (* Pink circle and arrow: [100] direction of the sample *)
16 {Pink, Circle[{0, 0}, 1],
17 Arrow[{{0, 0}, Kf[alphafix - gamma]}],
18 Text[Style["100", fs], 1.2 Kf[alphafix - gamma]],
19 (* Dashed line: the path of beam *)
20 {Dashed, Arrow[{-mdsc Ki, {0, 0}, mdsc Kf[betafix]}, {0, .1}]},
21 (* Purple arrows: the incident and final wavevectors *)
22 {Purple, Thick, Arrow[{- (mdsc/2) Ki, {0, 0}]},
23 Arrow[{{0, 0}, (mdsc/2) Kf[betafix]}],
24 Text[Style["ki", fs], -1.1 (mdsc/2) Ki],
25 Text[Style["kf", fs], 1.1 (mdsc/2) Kf[betafix]]},
26 (* Red arrow: the momentum change dk *)
27 {Red, Thick, Arrow[{{0, 0}, (mdsc/2) dK[betafix]}],
28 Text[Style["dk", fs], (mdsc/2) (1 + .1/Norm[dK[betafix]]) dK[betafix]]},
29 (* Blue arc: the arrangement of the detector *)
30 {Blue, Thickness [.02],
31 Circle[{0, 0}, mdsc, {betastt Degree, betaend Degree}]},
32 (* Green dot: the position of the detector cell *)
33 {Green, PointSize [.03], Point[mdsc Kf[betafix]]}}
34 , PlotRange -> {-1.1 mdsc, 1.1 mdsc}, ImageSize -> 500], (* Options of Show *)
35
36 Show[
37 (* Purple line : the axes and labels *)
38 Graphics[{Purple, Thick,
39 Arrow[{-axes[[1]], axes [[1]]}, Text[Style["h_0_0", fs], 1.12 axes [[1]]],
40 Arrow[{-axes[[2]], axes [[2]]}, Text[Style["0_h_0", fs], 1.05 axes [[2]]],
41 Arrow[{-axes[[3]], axes [[3]]}, Text[Style["h_-h_0", fs], 1.05 axes [[3]]}],
42 (* Red arrow: the momentum change dk *)

```

## Appendix C. Codes for the detector trajectory

```

43 Graphics[{{Red, Arrowheads[.05],
44   Arrow[{{0, 0}, trsc RM[gamma - alphafix].dK[betafix]}]},
45
46 (* Blue area: the total dk-coverage of the detector *)
47 ParametricPlot[
48   trsc RM[gamma - alpha].dK[theta], {theta, betastt, betaend}, {alpha, -0.001, alphafix},
49   PlotStyle -> LightBlue, Mesh -> {Floor[(betaend - betastt)/30], 360/30}],
50
51 (* Green curve: dk-coverage with the fixed sample *)
52 ParametricPlot[
53   trsc RM[gamma - alphafix].dK[theta], {theta, betastt, betaend},
54   PlotStyle -> {Blue, Thickness[.005]}],
55
56 (* Light green curve: dk-coverage of the chosen detector cell *)
57 ParametricPlot[
58   trsc RM[gamma - alpha].dK[betafix], {alpha, -0.001, alphafix},
59   PlotStyle -> {Green, Thickness[.005]}]
60
61 , Axes -> True, AxesStyle -> fs, ImageSize -> 800>(* Options of Show *)
62 }],(* Options of Row *)
63
64 (* Controls of Manipulate *)
65 {{lambda, 0.5, "Wavelength_of_Beam_(ang)"}, ControlType -> InputField, FieldSize -> 5},
66 {{betastt, 10, "Start_angle_of_Detector_bank"}, ControlType -> InputField, FieldSize -> 5},
67 {{betaend, 100, "End_angle_of_Detector_bank"}, ControlType -> InputField, FieldSize -> 5},
68 {{a, 1, "a*_Lin_reciprocal_space_(ang^-1)"}, ControlType -> InputField, FieldSize -> 5},
69   Delimiter,
70 {{gamma, 0, "Angle_of_Incident_Beam"}, -180, 180, 1, Appearance -> "Labeled"},
71 {{alphafix, 0, "Rotation_Angle_of_Sample"}, 0, 360, 1, Appearance -> "Labeled"},
72 {{betafix, 0.5 (betastt + betaend), "Angle_of_Detector_Cell"}, betastt, betaend, 1, Appearance
73   -> "Labeled"}
74 , SaveDefinitions -> True, ControlPlacement -> Top>(* Options of Manipulate *)
75 , WindowTitle -> "The.dk_coverage_of_the_detector",
76 Background -> White];(* Options of Dialog *)
77 ](* End of Module *)

```

To simulate detector trajectory in inelastic scattering, I made a Mathematica code *DT-inelastic.nb*.

```

1 Module[
2   {RM, k, Ki, Kf, Q, z, mdsc, trsc, a, lambda, Ei, axes, vecf, vecQ,
3     pstl, mshn, mstl, fs},(* Localized variables *)
4   RM := RotationMatrix[# Degree, {0, 0, 1}] &;
5   Ki = {1, 0, 0}; Kf := #2 RM[#1].Ki &; Q := Ki - Kf[#1, #2] &; z = {0, 0, 1};
6   mdsc = 2; axes = 2 trsc {Ki, Kf[60, 1], Kf[-60, 1]};
7   fs = 25;
8
9   CreateDialog[
10    Manipulate[
11     k = 2 Pi/lambda; trsc = k/a;

```

```

12  vecf = Kf[betafix, Sqrt[1 - Eloss/Ei]];
13  vecQ = Q[betafix, Sqrt[1 - Eloss/Ei]];
14  Row[{
15    Show[
16      (* Pink circle and arrow: [100] direction of the sample *)
17      ParametricPlot3D[{Cos[t], Sin[t], 0}, {t, 0, 2 Pi}, PlotStyle -> Pink],
18      Graphics3D[{Pink, Arrow[{{0, 0, 0}, Kf[alphafix - gamma, 1]}],
19        Text[Style["100", fs], 1.2 Kf[alphafix - gamma, 1]]}],
20
21    Graphics3D[{
22      (* Dashed line: the path of beam *)
23      {Dashed,
24        Arrow[{-mdsc Ki, {0, 0, 0}, mdsc Kf[betafix, 1]}, {0, .1}]},
25      (* Purple arrows: the incident and final wavevectors *)
26      {Purple, Thick,
27        Arrow[{-mdsc/2 Ki, {0, 0, 0}], Arrow[{{0, 0, 0}, (mdsc/2) vecf]},
28        Text[Style["ki", fs], -1.1 (mdsc/2) Ki], Text[Style["kf", fs], 1.1 (mdsc/2) vecf]},
29      (* Red arrow: the momentum change dk *)
30      {Red, Thick,
31        Arrow[{{0, 0, 0}, (mdsc/2) vecQ]}, Text[Style["Q", fs], (mdsc/2) (1 + .1/Norm[vecQ])
32          vecQ]}],
33
34      (* Blue arc: the arrangement of the detector *)
35      ParametricPlot3D[mdsc {Cos[t], Sin[t], 0}, {t, betastt Degree, betaend Degree},
36        PlotStyle -> {Blue, Thickness[.02]}],
37      (* Green dot: the position of the detector cell *)
38      Graphics3D[{Green, Sphere[mdsc Kf[betafix, 1], 0.1]}]
39
40      , ImageSize -> 400, PlotRange -> {{-mdsc, mdsc}, {-mdsc, mdsc}, All}, Axes -> False,
41      Boxed -> False, ViewPoint -> {0, 0, Infinity}],(* Options of 1st Show *)
42
43    Show[
44      (* Purple line: the axes and labels *)
45      Graphics3D[{Purple, Thick,
46        Arrow[{-axes[[1]], axes [[1]]}],
47        Text[Style["h_0_0", fs], 1.15 axes [[1]]],
48        Arrow[{-axes[[2]], axes [[2]]}],
49        Text[Style["0_h_0", fs], 1.05 axes [[2]]],
50        Arrow[{-axes[[3]], axes [[3]]}],
51        Text[Style["h_-h_0", fs], 1.05 axes [[3]]}],
52      (* Red arrow: the momentum change dk *)
53      Graphics3D[{Red, Arrowheads[.02], Arrow[{{0, 0, 0}, trsc RM[gamma - alphafix].vecQ]}],
54
55      (* Light blue volume: the total dk-coverage of the detector *)
56      pstl = {LightBlue, Opacity[0.4]};
57      mshn = {Floor[(betaend - betastt)/30], Floor[Ei/4]};
58      mstl = {Gray};
59      ParametricPlot3D[
60        trsc RM[gamma].Q[theta, Sqrt[1 - el/Ei]] + el z, {theta, betastt, betaend}, {el, 0, Ei}
        , PlotStyle -> pstl, Mesh -> mshn, MeshStyle -> mstl],

```

## Appendix C. Codes for the detector trajectory

```

61 ParametricPlot3D[
62   trsc RM[gamma - alphafix].Q[theta, Sqrt[1 - el/Ei]] + el z, {theta, betastt, betaend}, {el,
63     0, Ei}
64   , PlotStyle -> pstl, Mesh -> mshn, MeshStyle -> mstl],
65 ParametricPlot3D[
66   trsc RM[gamma - alpha].Q[betastt, Sqrt[1 - el/Ei]] + el z, {alpha, -0.001, alphafix}, {el, 0,
67     Ei}
68   , PlotStyle -> pstl, Mesh -> {6, Floor[Ei/4]}, MeshStyle -> mstl],
69 ParametricPlot3D[
70   trsc RM[gamma - alpha].Q[betaend, Sqrt[1 - el/Ei]] + el z, {alpha, -0.001, alphafix}, {el, 0,
71     Ei}
72   , PlotStyle -> pstl, Mesh -> {6, Floor[(betaend - betastt)/30], 6}],
73
74 (* Blue surface: dk-coverage with the fixed energy loss *)
75 ParametricPlot3D[
76   trsc RM[gamma - alpha].Q[theta, Sqrt[1 - Eloss/Ei]] + Eloss z, {theta, betastt, betaend}, {
77     alpha, -0.001, alphafix}
78   , PlotStyle -> {Blue, Opacity[0.6]}, Mesh -> False, BoundaryStyle -> {Thick, Blue}],
79 (* Green surface: dk-coverage of the chosen detector cell *)
80 ParametricPlot3D[
81   trsc RM[gamma - alpha].Q[betafix, Sqrt[1 - el/Ei]] + el z, {el, 0, Ei}, {alpha, -0.001,
82     alphafix}
83   , PlotStyle -> {Green, Opacity[0.6]}, Mesh -> False, BoundaryStyle -> {Thick, Green}]
84   , Axes -> True, AxesStyle -> fs, AxesOrigin -> {0, 0, 0}, BoxRatios -> {1, 1, 0.5},
85     BoxStyle -> Dashed,
86   ViewPoint -> {0.5, -5, 5}, ImageSize -> 800>(* Options of Show *)
87   ]],(* Options of Row *)
88
89 (* Controls of Manipulate *)
90 {{lambda, Sqrt[81.805/Ei], "Wavelength_of_beam_(ang)"},
91   ControlType -> InputField, FieldSize -> 5, Enabled -> False},
92 {{Ei, 20, "Incident_Energy_(meV)"}, ControlType -> InputField, FieldSize -> 5},
93 {{betastt, 10, "Start_Angle_of_Detector"}, ControlType -> InputField, FieldSize -> 5},
94 {{betaend, 100, "End_Angle_of_Detector"}, ControlType -> InputField, FieldSize -> 5},
95 {{a, 1, "a*_lin_reciprocal_space_(ang^-1)"}, ControlType -> InputField, FieldSize -> 5},
96 Delimiter, {{gamma, 0, "Angle_of_Incident_Beam"}, 0, 180, 1, Appearance -> "Labeled"},
97 {{alphafix, 0, "Rotation_Angle_of_Sample"}, 0, 360, 1, Appearance -> "Labeled"},
98 {{betafix, 0.5 (betastt + betaend), "Angle_of_Detector_Cell"}, betastt, betaend, 1, Appearance
99   -> "Labeled"},
100 {{Eloss, 3 Floor[Ei/10], "Energy_loss"}, 0, Ei, Floor[Ei/10], Appearance -> "Labeled"}
101 , SaveDefinitions -> True, ControlPlacement -> Top
102 , WindowTitle -> "The_Q-E_coverage_of_the_detector",
103 Background -> White];(* Options of Dialog *)
104 ]

```

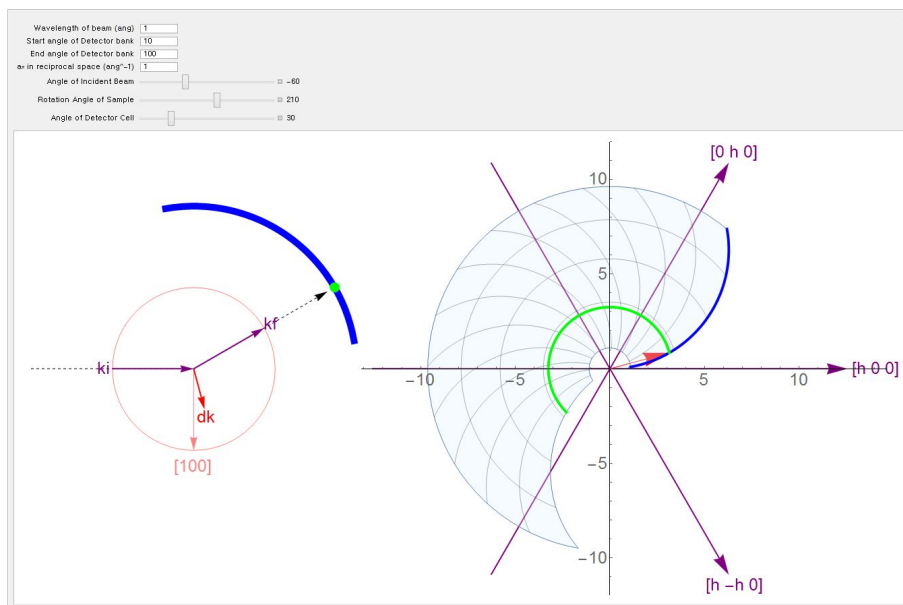


Figure C.1:  $Q$  coverage simulation using *DT-elastic.nb* code.

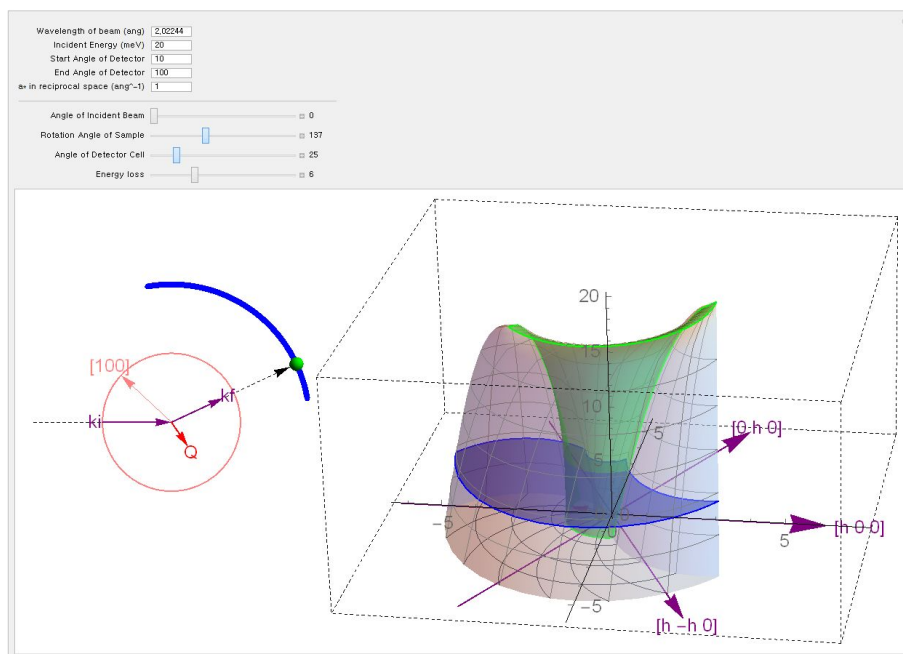


Figure C.2:  $Q$ - $E$  coverage simulation using *DT-inelastic.nb* code. Three dimensional detector trajectory is plotted by a rotation angle of the sample.



## Appendix D. Codes for the spin waves calculations

To calculate the dynamical structure factor  $S(\mathbf{q}, \omega)$ , I made a MATLAB code *calc\_dis.m*.

```

1 function [eng,int] = calc_dis(paraset, qpos)
2 % calculate dispersion relation by solving eigenvalue problem
3 % input – paraset=[S J1 J2 D1 D2 K] : parameters
4 %     qpos=array(n,3) : array of q points in hexagonal r.l.u.
5 % output – eng=array(n,m): energy of m modes
6 %     int=array(n,m): intensity corresponding to eng
7
8 % set hexagonal reciprocal lattice vector in cubic(cartesian) coord.
9 B1=[1;0;0]; B2=[0;1;0]; B3=[0;0;1];
10 B12=B1-B2; B23=B2-B3; B31=B3-B1;
11 A1=B2+B3; A2=B3+B1; A3=B1+B2;
12 NN = [B1 B2 B3]; NNN = [A1 A2 A3 B12 B23 B31];
13
14 Qa=2*pi*(1/3)*(B1-2*B2+B3); Qb=2*pi*(1/3)*(2*B1-B2-B3); Qc=2*pi*(1/6)*(B1+B2+B3);
15
16 % parameters
17 pS = paraset(1);           % S: spin number
18 SS = sqrt(pS*(pS+1));    % SS: quantum spin number
19 pJ1 = paraset(2);         % J1: NN interaction
20 pJ2 = paraset(3);         % J2: NNN interaction
21 pD1 = paraset(4);         % D1: DM interaction along [110]
22 pD2 = paraset(5);         % D2: DM interaction along [001]
23 pK = paraset(6);         % K: SIA parameter
24
25 pq = -2*pD1/(pJ1-4*pJ2);  % q: modulation index
26 qq = [pq/2 -pq/2 0];     % q: modulation vector
27 % qq = [pq/2 0 -pq/2];   % q: modulation vector
28 QQ = 2*pi*[0.5 0.5 0.5] + qq; % Q: propagation vector
29
30 n = size(qpos,1);
31
32 %% For various models
33 % Make k-array and H matrix-array, and get Energy and Intensity
34
35 % if pD1==0 && pD2==0 % D1=D2=0: basic J(-K) model, 1 mode
36 %
37 %     % make k points in cubic notation
38 %     % dim(k) = (n,3)
39 %     k = qpos*[Qa Qb Qc]';
40 %
41 %     % make Hamiltonian matrix-array for q-array
42 %     % dim(HM)=(2,2,n)

```

## Appendix D. Codes for the spin waves calculations

---

```

43 %   HM = H0M1(k);
44 %   % get energy and intensity
45 %   [eng,int] = getEI(HM);
46
47 if pD1==0 && pD2==0 % D1=D2=0: basic J(-K) model, degenerate 3 modes
48     % for a direct comparison
49
50     % make q points in cubic for 3 momenta: k-Q, k and k+Q
51     % dim(k) = (3n,3)
52     k = [ ( qpos*[Qa Qb Qc]' - ones(n,1)*QQ );
53           ( qpos*[Qa Qb Qc]' );
54           ( qpos*[Qa Qb Qc]' + ones(n,1)*QQ ) ];
55
56     % make Hamiltonian matrix--array for q--array
57     % dim(HM)=(2,2,3n)
58     HM = H0M1(k);
59     % get energy and intensity
60     [peng,pint] = getEI(HM);
61
62     % rearrange result array
63     % eng(n,9) = [E(k-Q)(n,3) E(k)(n,3) E(k+Q)(n,3)]
64     eng = [peng(1:n,:) peng(n+1:2*n,:) peng(2*n+1:3*n,:)];
65     int = [pint(1:n,:) pint(n+1:2*n,:) pint(2*n+1:3*n,:)];
66
67 elseif pD2==0 && pK==0 % D2=K=0: J-D1 model, 3 modes
68
69     % make q points in cubic for 3 momenta: k-Q, k and k+Q
70     % dim(k) = (3n,3)
71     k = [ ( qpos*[Qa Qb Qc]' - ones(n,1)*QQ );
72           ( qpos*[Qa Qb Qc]' );
73           ( qpos*[Qa Qb Qc]' + ones(n,1)*QQ ) ];
74
75     % make Hamiltonian matrix--array for q--array
76     % dim(HM)=(2,2,3n)
77     HM = H0M1(k);
78     % get energy and intensity
79     [peng,pint] = getEI(HM);
80
81     % rearrange result array
82     % eng(n,9) = [E(k-Q)(n,3) E(k)(n,3) E(k+Q)(n,3)]
83     eng = [peng(1:n,:) peng(n+1:2*n,:) peng(2*n+1:3*n,:)];
84     int = [pint(1:n,:) pint(n+1:2*n,:) pint(2*n+1:3*n,:)];
85
86 elseif pK==0 % K=0: J-D1-D2 model, 3*3 modes
87
88     % make q points in cubic for 3 momenta: k-Q, k and k+Q
89     % dim(k) = (3n,3)
90     k = [ ( qpos*[Qa Qb Qc]' - ones(n,1)*QQ );
91           ( qpos*[Qa Qb Qc]' );
92           ( qpos*[Qa Qb Qc]' + ones(n,1)*QQ ) ];

```

---

```

93
94 % make Hamiltonian matrix-array for q-array
95 % dim(HM)=(6,6,3n)
96 HM = H0M3(k,qq) + HpD(k);
97 % HM = HpD2(k);
98 % get energy and intensity
99 [peng,pint] = getEI(HM);
100
101 % rearrange result array
102 % eng(n,9) = [E(k-Q)(n,3) E(k)(n,3) E(k+Q)(n,3)]
103 eng = [peng(1:n,:) peng(n+1:2*n,:) peng(2*n+1:3*n,:)];
104 int = [pint(1:n,:) pint(n+1:2*n,:) pint(2*n+1:3*n,:)];
105
106 elseif pD2==0 % D2=0: J-D1-K model, 3*3 modes
107
108 Kt = pK/(II(2*qq)-II([0 0 0])); % Ktilde in Furukawa's note
109 DD = pK/2 - 2*CC(qq); % D in Furukawa's note
110
111 % make q points in cubic for 3 momenta: k-Q, k and k+Q
112 % dim(k) = (3n,3)
113 k = [ ( qpos*[Qa Qb Qc]' - ones(n,1)*QQ );
114 ( qpos*[Qa Qb Qc]' );
115 ( qpos*[Qa Qb Qc]' + ones(n,1)*QQ ) ];
116
117 % make Hamiltonian matrix-array for q-array
118 % dim(HM)=(6,6,3n)
119 HM = H0M3(k,2*qq) + HpK(k);
120 % get energy and intensity
121 [peng,pint] = getEI(HM);
122
123 % rearrange result array
124 % eng(n,9) = [E(k-Q)(n,3) E(k)(n,3) E(k+Q)(n,3)]
125 eng = [peng(1:n,:) peng(n+1:2*n,:) peng(2*n+1:3*n,:)];
126 int = [pint(1:n,:) pint(n+1:2*n,:) pint(2*n+1:3*n,:)];
127
128 else
129 disp('no model')
130 eng = zeros(n,1);
131 int = zeros(n,1);
132 end
133
134 %% Calculate dispersion energy and intensity
135 % get eigenvalues and eigenvectors: generalized Bogoliubov transform
136 % parallel computing using 'parfor': it can be expanded to GPU computing
137 function [Eng,Int] = getEI(HM)
138 N = size(HM,3);
139
140 % g: metric for Bogoliubov transform
141 dim = size(HM,1)/2;
142 g = [eye(dim) zeros(dim); zeros(dim) -eye(dim)];

```

## Appendix D. Codes for the spin waves calculations

```

143
144     parfor i=1:N
145         % get eigenvalues and eigenvectors
146         [V,D] = eig(g*HM(:,i));
147
148         % remove imaginary values
149         idx = imag(diag(D))~=0;
150         D(:,idx) = 0; V(:,idx) = 0;
151
152         % sort eigenvalues and eigenvectors
153         % in order of [e1 e2 e3 ... -e1 -e2 -e3 ...]
154         [eigs,idx] = sort(diag(D),'descend');
155         V = V(:,[idx(1:dim) idx(2*dim:-1:dim+1)]);
156
157         % rescale eigenvectors to satisfy the condition for Bogoliubov transform
158         % V'*g*V = I
159         fac = sqrt(abs(1./diag(V'*g*V)));
160         fac(isinf(fac)) = 0; % prevent NaN from 0*inf
161         V = V .* (ones(dim*2,1)*fac');
162
163         % put the values of energy and intensity into the output variables
164         % kk= -k-Q (i=[ 1, n], p=-1), int~ (V_2x - V_5x)^2
165         % kk= -k (i=[ n+1,2n], p= 0), int~ (V_2x + V_5x)^2
166         % kk= -k+Q (i=[2n+1,3n], p= 1), int~ (V_2x - V_5x)^2
167         p = floor(i/n)-floor(N/n/2);
168         Eng(i,:) = 2*SS * eigs(1:dim);
169         idx1=ceil(dim/2); idx2=dim+1:2*dim;
170         Int(i,:) = SS/2* abs( V(idx1,idx2) + (-1)^p * V(idx1+dim,idx2) ).^2;
171     end
172 end
173
174 %% Make Hamiltonian matrix for various models
175 % Hamiltonian matrix for J(-K) model: D1=D2=0
176
177 % Basic Hamiltonian matrix for J-K model and J-D1 model
178 % J-K model: only k mode
179 % J-D1 model: splitting k and k(+/-)Q modes
180 function out = H0M1(kk)
181     % input: k array(N,3)
182     % output: H array(2,2,N)
183
184     % M1,M2: parts of Hamiltonian matrix
185     % arrange element arrays in order of
186     % M(N,4) = [M_11 M_21 , M_12 M_22]
187     % reshape M'(4,N) to M(2,2,N)
188     M1 = AA(kk)+pK/4;
189     M2 = BB(kk)+pK/4;
190
191     out = [M1 M2 , M2 M1];
192     out = reshape(out', 2,2,[]);

```

```

193     end
194
195 % Hamiltonian matrix for J-D1(-D2/K) model: splitting k and k(+/-)Q modes
196 % J-D1-D2 model: mixing between k and k(+/-)q
197 % J-D1-K model: mixing between k and k(+/-)2q
198     function out = H0M3(kk,qqq)
199         % input: k array(N,3), q array(1,3)
200         % output: H array(6,6,N)
201
202         qqAr = ones(size(kk,1),1)*qqq;
203         Ap = AA( kk + qqAr ); A0 = AA( kk ); Am = AA( kk - qqAr );
204         Bp = BB( kk + qqAr ); B0 = BB( kk ); Bm = BB( kk - qqAr );
205         Z0 = zeros(size(kk,1),1);
206
207         % M1,M2: parts of Hamiltonian matrix
208         % arrange element arrays in order of
209         % M(N,9) = [M_11 M_21 M_31 M_12 M_22 M_32 M_13 M_23 M_33]
210         % reshape M'(9,N) to M(3,3,N)
211         M1 = [Ap+pK/4 Z0 Z0 , Z0 A0+pK/4 Z0 , Z0 Z0 Am+pK/4];
212         M1 = reshape(M1', 3,3,[]);
213         M2 = [Bp+pK/4 Z0 Z0 , Z0 B0+pK/4 Z0 , Z0 Z0 Bm+pK/4];
214         M2 = reshape(M2', 3,3,[]);
215
216         out = [M1 M2; M2 M1];
217     end
218
219 % perturbed Hamiltonian matrix for J-D1-K model: D2=0
220     function out = HpK(kk)
221         % input: k array(N,3)
222         % output: H array(6,6,N)
223
224         qqAr = ones(size(kk,1),1)*qqq;
225         Cp = CC( kk + qqAr ); Cm = CC( kk - qqAr );
226         Z0 = zeros(size(kk,1),1);
227
228         % M1,M2: parts of Hamiltonian matrix
229         % arrange element arrays in order of
230         % M(N,9) = [M_11 M_21 M_31 M_12 M_22 M_32 M_13 M_23 M_33]
231         % reshape M'(9,N) to M(3,3,N)
232         M1 = [Z0 Cp+DD Z0 , Cp+DD Z0 Cm+DD , Z0 Cm+DD Z0];
233         M1 = reshape(M1', 3,3,[]);
234         M2 = [Z0 -Cp Z0 , -Cp Z0 -Cm , Z0 -Cm Z0];
235         M2 = reshape(M2', 3,3,[]);
236
237         out = [M1 M2; M2 M1];
238     end
239
240 % perturbed Hamiltonian matrix for J-D1-D2 model: K=0
241     function out = HpD(kk)
242         % input: k array(N,3)

```

## Appendix D. Codes for the spin waves calculations

```

243     % output: H array(6,6,N)
244
245     qqAr = ones(size(kk,1),1)*qq;
246     Fp = FF( kk + qqAr ); F0 = FF( kk ); Fm = FF( kk - qqAr );
247     Z0 = zeros(size(kk,1),1);
248
249     % arrange element arrays in order of
250     % M(N,9) = [M_11 M_21 M_31 M_12 M_22 M_32 M_13 M_23 M_33]
251     % reshape M'(9,N) to M(3,3,N)
252     % M1 = [Z0 +Fp-F0 Z0 , +Fp-F0 Z0 +F0-Fm , Z0 +F0-Fm Z0];
253     % M1 = reshape(M1', 3,3,[]);
254     % M2 = [Z0 +Fp+F0 Z0 , -Fp-F0 Z0 +F0+Fm , Z0 -F0-Fm Z0];
255     % M2 = reshape(M2', 3,3,[]);
256     M1 = [Z0 F0 Z0 , Fp Z0 Fm , Z0 F0 Z0];
257     M1 = reshape(M1', 3,3,[]);
258
259     % out = [M1 M2; -M2 -M1];
260     out = [M1 -M1; M1 -M1];
261
262     end
263
264     %% perturbed Hamiltonian matrix for J-D1-D2 model: K=0
265     function out = HpD2(kk)
266         % input: k array(N,3)
267         % output: H array(6,6,N)
268
269         qqAr = ones(size(kk,1),1)*qq;
270         wp = ww( kk+qqAr ); w0 = ww( kk ); wm = ww( kk-qqAr );
271         Fp = FF( kk+qqAr ); F0 = FF( kk ); Fm = FF( kk-qqAr );
272         eLp = (e2L( kk+qqAr )./e2L( kk )).^0.5;
273         eLm = (e2L( kk-qqAr )./e2L( kk )).^0.5;
274         Z0 = zeros(size(kk,1),1);
275
276         % arrange element arrays in order of
277         % M(N,9) = [M_11 M_21 M_31 M_12 M_22 M_32 M_13 M_23 M_33]
278         % reshape M'(9,N) to M(3,3,N)
279         M0 = [wp Z0 Z0 , Z0 w0 Z0 , Z0 Z0 wm];
280         M0 = reshape(M0', 3,3,[]);
281         M1 = [Z0 Fp.*eLp-F0 Z0 , Fp.*eLp-F0 Z0 F0-Fm.*eLm , Z0 F0-Fm.*eLm Z0];
282         M1 = reshape(M1', 3,3,[]);
283         M2 = [Z0 Fp.*eLp+F0 Z0 , -Fp.*eLp-F0 Z0 F0+Fm.*eLm , Z0 -F0-Fm.*eLm Z0];
284         M2 = reshape(M2', 3,3,[]);
285
286         out = [M0+M1 M2; -M2 M0-M1];
287
288     end
289
290     %% functions for making Hamiltonian
291
292     function out = ww(kk)

```

```

293     out = ( (JJ(kk)-II([0 0 0])) .* (II(kk)-II([0 0 0])) ) .^0.5;
294 end
295
296 function out = e2L(kk)
297     out = ( (II(kk)-II([0 0 0])) ./ (JJ(kk)-II([0 0 0])) ) .^0.5;
298 end
299
300 function out = JJ(kk)
301     out = -pJ1* sum( cos(kk*NN) ,2) -pJ2* sum( cos(kk*NNN) ,2);
302 end
303
304 function out = II(kk)
305     QQAr = ones(size(kk,1),1)*QQ;
306
307     out = -pJ1* sum( cos(QQAr*NN) .* cos(kk*NN) ,2) ...
308         -pJ2* sum( cos(QQAr*NNN) .* cos(kk*NNN) ,2) ...
309         -pD1* ( sin(QQAr*B12) .* cos(kk*B12) );
310 end
311
312 function out = AA(kk)
313     out = 0.5*(II(kk)+JJ(kk))-II([0,0,0]);
314 end
315
316 function out = BB(kk)
317     out = 0.5*(JJ(kk)-II(kk));
318 end
319
320 function out = CC(kk)
321     qqAr = ones(size(kk,1),1)*qq;
322     QQAr = ones(size(kk,1),1)*QQ;
323     out = pK/8 + Kt/4* ...
324         ( -pJ1* sum( sin(qqAr*NN).*sin(QQAr*NN).*cos(kk*NN) ,2)...
325         -pJ2* sum( sin(qqAr*NNN).*sin(QQAr*NNN).*cos(kk*NNN) ,2)...
326         +pD1* ( sin(qqAr*B12).*cos(qqAr*B12).*cos(kk*B12) ) );
327 end
328
329 function out = FF(kk)
330     out = pD2/2 * ( cos(kk*sum(NN,2)) -1/3 *sum(cos(kk*NN),2) );
331 end
332
333 end

```

To simulate the  $E$ -scan and  $q$ - $E$  map convoluted with the resolution function, I made a MATLAB code *convol\_Escan.m*.

```

1 function [chi,err] = convol_Escan(h_fig,para,stt ,Erng,np)
2 %
3 %
4
5 % sample orientation

```

## Appendix D. Codes for the spin waves calculations

```

6 | dirset = edit2num(h_fig, {'dir11', 'dir12', 'dir13';
7 |                       'dir21', 'dir22', 'dir23';
8 |                       'dir31', 'dir32', 'dir33'});
9 | qlen = [edit2num(h_fig, {'leng1', 'leng2', 'leng3'}) 1];
10
11 | % resolution matrix in
12 | resmat = edit2num(h_fig, {'Res11', 'Res12', 'Res13', 'Res14';
13 |                          'Res21', 'Res22', 'Res23', 'Res24';
14 |                          'Res31', 'Res32', 'Res33', 'Res34';
15 |                          'Res41', 'Res42', 'Res43', 'Res44'});
16
17 | % generate normally distributed random points with sigma_i
18 | Aij = resmat .* (qlen'*qlen);
19 | Rth = 0.5*atan(2*Aij(1,2)/(Aij(1,1)-Aij(2,2)));
20 | RM = [cos(Rth) -sin(Rth) 0; sin(Rth) cos(Rth) 0; 0 0 1];
21 | Bij = RM' * Aij(1:3,1:3) * RM;
22 | Rsig = 1./sqrt(diag(Bij)');
23
24 | pts = randn(np,3) .* (ones(np,1) * Rsig);
25 | pts = pts * RM';
26 | % make Q-points from scan position
27 | qpos = ones(np,1)*stt + pts*dirset;
28
29 | % calculate dispersion
30 | tic
31 | [o_eng, o_int] = calc_dis(para, qpos);
32 | toc
33
34 | % gaussian convolution along E-axis
35 | chi = zeros(size(Erng));
36 | err = chi;
37 | s = size(o_eng,2);
38 | dQx = pts(:,1)*ones(1,s);
39 | dQy = pts(:,2)*ones(1,s);
40
41 | for i=1:length(Erng)
42 |     dE = Erng(i)-o_eng(:);
43 |     Efac = 2*Aij(1,4)*dQx(:).*dE + 2*Aij(2,4)*dQy(:).*dE + Aij(4,4)*dE.^2;
44 |     meas = o_int(:) .* exp(-0.5 * Efac);
45 |     chi(i) = sum(meas)/np;
46 |     err(i) = sqrt(sum(meas.^2)/np - chi(i)^2) / sqrt(np);
47 | end
48 | end

```

To build a GUI panel and plot the calculated results, I made a MATLAB code *calc\_dis.m*.

```

1 | function BFOmagnon
2 |
3 | h_fig = figure('name','Magnon dispersion','numbertitle','off','color',[204,229,255]/255,...

```

```

4     'position',[100,100,500,650], 'resizefcn',@resize_main,'menubar','none',...
5     'CloseRequestFcn',@close_main);
6
7 % make uicontrols in main panel
8 % set position, style, related info first, then call this function
9     function ui_conf(vpos,hpos,ui_style,ui_string)
10        bgcolor = get(gcf,'color');
11        h_text = 20;
12        h_edit = 23;
13        for i=1:length(ui_style)
14            switch ui_style{i}
15                case 'T' % text (bold)
16                    uicontrol('style','text','string',ui_string{i},...
17                        'userdata',[sum(hpos(1:(2*i-1))),vpos,hpos(2*i),h_text],...
18                        'fontsize',10,'backgroundcolor',bgcolor,'horizontalalignment','left',...
19                        'fontweight','bold')
20                case 't' % text
21                    uicontrol('style','text','string',ui_string{i},...
22                        'userdata',[sum(hpos(1:(2*i-1))),vpos,hpos(2*i),h_text],...
23                        'fontsize',10,'backgroundcolor',bgcolor,'horizontalalignment','left')
24                case 'e' % edit (enable)
25                    uicontrol('style','edit','tag',ui_string{i},...
26                        'userdata',[sum(hpos(1:(2*i-1))),vpos,hpos(2*i),h_edit],...
27                        'fontsize',10,'backgroundcolor','w')
28                case 'ef' % edit (enable)
29                    uicontrol('style','edit','tag',ui_string{i}{1},...
30                        'userdata',[sum(hpos(1:(2*i-1))),vpos,hpos(2*i),h_edit],...
31                        'fontsize',10,'backgroundcolor','w','callback',ui_string{i}{2})
32                case 'E' % edit (disable)
33                    uicontrol('style','edit','tag',ui_string{i},...
34                        'userdata',[sum(hpos(1:(2*i-1))),vpos,hpos(2*i),h_edit],...
35                        'fontsize',10,'backgroundcolor','w','enable','off')
36                case 'p' % popup menu
37                    uicontrol('style','popupmenu','tag',ui_string{i}{1},'string',ui_string{i}{2},...
38                        'userdata',[sum(hpos(1:(2*i-1))),vpos+2,hpos(2*i),h_edit],...
39                        'fontsize',10,'backgroundcolor','w')
40                case 'b' % push button
41                    uicontrol('style','pushbutton','string',ui_string{i}(1),...
42                        'userdata',[sum(hpos(1:(2*i-1))),vpos,hpos(2*i),h_edit],...
43                        'fontsize',10,'callback',ui_string{i}{2})
44            end
45        end
46    end
47
48    vps = -30; hps = 20;
49
50    vpos = vps;
51    hpos = [hps 40 5 150 10 60 10 60];
52    ui_style = {'T','e','b','b'};
53    ui_string = {'Title','title',{'Load',@load_para},{'Save',@save_para}};

```

## Appendix D. Codes for the spin waves calculations

---

```

54 | ui_conf(vpos,hpos, ui_style , ui_string )
55 |
56 | %% Lattice parameters
57 | vpos = vpos - 25;
58 | hpos = [hps 200];
59 | ui_style = {'T'};
60 | ui_string = {'Lattice info'};
61 | ui_conf(vpos,hpos, ui_style , ui_string )
62 |
63 | vpos = vpos - 25;
64 | hpos = [hps 15 5 60 10 15 5 60 10 15 5 60 5 30];
65 | ui_style = {'t','ef','t','ef','t','ef','t'};
66 | ui_string = {'a',{'lat.a'},@recip},'b',{'lat.b'},@recip},'c',{'lat.c'},@recip},'\AA');
67 | ui_conf(vpos,hpos, ui_style , ui_string )
68 |
69 | vpos = vpos - 25;
70 | hpos = [hps 15 5 60 10 15 5 60 10 15 5 60 5 40];
71 | ui_style = {'t','ef','t','ef','t','ef','t'};
72 | ui_string = {'\alpha',{'lat.alp'},@recip},'\beta',{'lat.bet'},@recip},'\gamma',{'lat.gam'},@recip},'(deg)'};
73 | ui_conf(vpos,hpos, ui_style , ui_string )
74 |
75 | vpos = vpos - 25;
76 | hpos = [hps 15 5 60 10 15 5 60 10 15 5 60 5 40];
77 | ui_style = {'t','E','t','E','t','E','t'};
78 | ui_string = {'a*','rec.a','b*','rec.b','c*','rec.c'},'\AA^{-1}'};
79 | ui_conf(vpos,hpos, ui_style , ui_string )
80 |
81 | vpos = vpos - 25;
82 | hpos = [hps 15 5 60 10 15 5 60 10 15 5 60 5 40];
83 | ui_style = {'t','E','t','E','t','E','t'};
84 | ui_string = {'\alpha*','rec.alp','\beta*','rec.bet','\gamma*','rec.gam'},'(deg)'};
85 | ui_conf(vpos,hpos, ui_style , ui_string )
86 |
87 | %% Interaction parameters
88 | vpos = vpos - 30;
89 | hpos = [hps 200];
90 | ui_style = {'T'};
91 | ui_string = {'Interaction parameters'};
92 | ui_conf(vpos,hpos, ui_style , ui_string )
93 |
94 | vpos = vpos - 25;
95 | hpos = [hps 20 5 60 10 20 5 60 10 20 5 60];
96 | ui_style = {'t','e','t','e','t','e'};
97 | ui_string = {'S','par.S','J1','par.J1','J2','par.J2'};
98 | ui_conf(vpos,hpos, ui_style , ui_string )
99 |
100 | vpos = vpos - 25;
101 | hpos = [hps 20 5 60 10 20 5 60 10 20 5 60];
102 | ui_style = {'t','e','t','e','t','e'};

```

---

```

103 | ui_string = {'D1','par_D1','D2','par_D2','K','par_K'};
104 | ui_conf(vpos,hpos,ui_style , ui_string )
105 |
106 | %% Plot dispersion line
107 | vpos = vpos - 30;
108 | hpos = [hps 200];
109 | ui_style = {'T'};
110 | ui_string = {'Plot dispersion line'};
111 | ui_conf(vpos,hpos,ui_style , ui_string )
112 |
113 | vpos = vpos - 25;
114 | hpos = [hps 50 5 30 5 30 5 30 10 40 5 30 5 30 5 30];
115 | ui_style = {'t','e','e','e','t','e','e','e'};
116 | ui_string = {'Starting','line_s1','line_s2','line_s3',...
117 |             'along','line_d1','line_d2','line_d3'};
118 | ui_conf(vpos,hpos,ui_style , ui_string )
119 |
120 | vpos = vpos - 25;
121 | hpos = [hps 50 5 50 5 50 10 30 5 50 10 100];
122 | ui_style = {'t','e','e','t','e','b'};
123 | ui_string = {'Q range','line.Q1','line.Q2','step','line.Q3', {'Line Plot',@dis_line}};
124 | ui_conf(vpos,hpos,ui_style , ui_string )
125 |
126 | %% Sample orientation
127 | vpos = vpos - 30;
128 | hpos = [hps 200];
129 | ui_style = {'T'};
130 | ui_string = {'Sample orientation'};
131 | ui_conf(vpos,hpos,ui_style , ui_string )
132 |
133 | vpos = vpos - 25;
134 | hpos = [hps 30 5 30 5 30 5 30 10 60];
135 | ui_style = {'t','ef','ef','ef','E'};
136 | ui_string = {'Q1',{'dir11',@qlen},{'dir12',@qlen},{'dir13',@qlen},'leng1'};
137 | ui_conf(vpos,hpos,ui_style , ui_string )
138 |
139 | vpos = vpos - 25;
140 | hpos = [hps 30 5 30 5 30 5 30 10 60];
141 | ui_style = {'t','ef','ef','ef','E'};
142 | ui_string = {'Q2',{'dir21',@qlen},{'dir22',@qlen},{'dir23',@qlen},'leng2'};
143 | ui_conf(vpos,hpos,ui_style , ui_string )
144 |
145 | vpos = vpos - 25;
146 | hpos = [hps 30 5 30 5 30 5 30 10 60];
147 | ui_style = {'t','ef','ef','ef','E'};
148 | ui_string = {'Qz',{'dir31',@qlen},{'dir32',@qlen},{'dir33',@qlen},'leng3'};
149 | ui_conf(vpos,hpos,ui_style , ui_string )
150 |
151 | %% Resolution information
152 | vpos = vpos + 105;

```

## Appendix D. Codes for the spin waves calculations

---

```

153 | hps = hps + 220;
154 |
155 | vpos = vpos - 30;
156 | hpos = [hps 200];
157 | ui_style = {'T'};
158 | ui_string = {'Resolution matrix'};
159 | ui_conf(vpos,hpos,ui_style , ui_string )
160 |
161 | vpos = vpos - 25;
162 | hpos = [hps 60 5 60 5 60 5 60];
163 | ui_style = {'e', 'ef', 'E', 'ef'};
164 | ui_string = {'Res11', {'Res12', @symmet}, 'Res13', {'Res14', @symmet}};
165 | ui_conf(vpos,hpos,ui_style , ui_string )
166 | vpos = vpos - 25;
167 | hpos = [hps 60 5 60 5 60 5 60];
168 | ui_style = {'E', 'e', 'E', 'ef'};
169 | ui_string = {'Res21', 'Res22', 'Res23', {'Res24', @symmet}};
170 | ui_conf(vpos,hpos,ui_style , ui_string )
171 | vpos = vpos - 25;
172 | hpos = [hps 60 5 60 5 60 5 60];
173 | ui_style = {'E', 'E', 'e', 'E'};
174 | ui_string = {'Res31', 'Res32', 'Res33', 'Res34'};
175 | ui_conf(vpos,hpos,ui_style , ui_string )
176 | vpos = vpos - 25;
177 | hpos = [hps 60 5 60 5 60 5 60];
178 | ui_style = {'E', 'E', 'E', 'e'};
179 | ui_string = {'Res41', 'Res42', 'Res43', 'Res44'};
180 | ui_conf(vpos,hpos,ui_style , ui_string )
181 |
182 | %% Simulation: E-scan
183 | hps = hps-220;
184 | vpos = vpos - 30;
185 | hpos = [hps 200];
186 | ui_style = {'T'};
187 | ui_string = {'Simulate E-scan'};
188 | ui_conf(vpos,hpos,ui_style , ui_string )
189 |
190 | vpos = vpos - 25;
191 | hpos = [hps 50 5 30 5 30 5 30 10 60 5 60];
192 | ui_style = {'t', 'e', 'e', 'e', 't', 'e'};
193 | ui_string = {'Starting', 'Escan_s1', 'Escan_s2', 'Escan_s3', '# of points', 'Escan_np'};
194 | ui_conf(vpos,hpos,ui_style , ui_string )
195 |
196 | vpos = vpos - 25;
197 | hpos = [hps 50 5 50 5 50 10 30 5 50 10 100];
198 | ui_style = {'t', 'e', 'e', 't', 'e', 'b'};
199 | ui_string = {'E range', 'Escan_E1', 'Escan_E2', 'step', 'Escan_E3', {'Simulate', @sim_Escan}};
200 | ui_conf(vpos,hpos,ui_style , ui_string )
201 |
202 | %% Simulation: Q-E contour

```

```

203 | vpos = vpos - 30;
204 | hpos = [hps 200];
205 | ui_style = {'T'};
206 | ui_string = {'Simulate contour map'};
207 | ui_conf(vpos,hpos,ui_style , ui_string )
208 |
209 | vpos = vpos - 25;
210 | hpos = [hps 50 5 30 5 30 5 30 10 40 5 30 5 30 5 30];
211 | ui_style = {'t','e','e','e','t','e','e','e'};
212 | ui_string = {'Starting','cont_s1','cont_s2','cont_s3','along','cont_d1','cont_d2','cont_d3'};
213 | ui_conf(vpos,hpos,ui_style , ui_string )
214 |
215 | vpos = vpos - 25;
216 | hpos = [hps 50 5 50 5 50 10 30 5 50 10 60 5 60];
217 | ui_style = {'t','e','e','t','e','t','e'};
218 | ui_string = {'Q range','cont_Q1','cont_Q2','step','cont_Q3','# of points','cont_np'};
219 | ui_conf(vpos,hpos,ui_style , ui_string )
220 |
221 | vpos = vpos - 25;
222 | hpos = [hps 50 5 50 5 50 10 30 5 50 10 100];
223 | ui_style = {'t','e','e','t','e','b'};
224 | ui_string = {'E range','cont_E1','cont_E2','step','cont_E3','Contour Plot',@sim_contour}};
225 | ui_conf(vpos,hpos,ui_style , ui_string )
226 |
227 | start_main(h_fig)
228 |
229 | end
230 |
231 | %%
232 | function start_main(h_fig)
233 |
234 | fname = 'lastpar.mat';
235 | if exist(fname,'file')
236 |     load(fname)
237 |     set(h_fig,'position',pos)
238 |     for i=1:length(tag)
239 |         set(findobj(h_fig,'type','uicontrol','style','edit',...
240 |             'tag',tag{i}),'string',para{i})
241 |     end
242 | end
243 | end
244 |
245 | function close_main(h_fig,~)
246 |
247 | fname = 'lastpar.mat';
248 | pos = get(h_fig,'position');
249 | h_edt = findobj(h_fig,'type','uicontrol','style','edit');
250 | tag = get(h_edt,'tag');
251 | para = get(h_edt,'string');
252 |

```

## Appendix D. Codes for the spin waves calculations

---

```
253 save(fname,'pos', 'tag', 'para')
254
255 delete(h_fig)
256 end
257
258 function resize_main(h_fig,~)
259 % for resizing main control figure
260 size = get(h_fig, 'position');
261 h_ctr = findobj(h_fig, 'type', 'uicontrol');
262
263 for i=1:length(h_ctr)
264     pos = get(h_ctr(i), 'userdata');
265     pos = pos + [0 size(4) 0 0];
266     set(h_ctr(i), 'position', pos)
267 end
268 end
269
270 %%
271 function load_para(h_but,~)
272
273 [fname,pname] = uigetfile('*.*mat','Load Parameters From');
274 if fname==0
275     return
276 end
277
278 parfile = fullfile(pname,fname);
279 if exist(parfile, 'file')
280     load(fname)
281 else
282     msgbox('No such parameter file.\n','Error', 'error')
283     return
284 end
285 for i=1:length(tag)
286     set(findobj(get(h_but, 'parent'), 'type', 'uicontrol', 'style', 'edit', ...
287         'tag', tag{i}), 'string', para{i})
288 end
289 end
290
291 function save_para(h_but,~)
292
293 [fname,pname] = uiputfile('*.*mat','Save Parameters As');
294 if fname==0
295     return
296 end
297
298 parfile = fullfile(pname,fname);
299 h_edt = findobj(get(h_but, 'parent'), 'type', 'uicontrol', 'style', 'edit');
300 tag = get(h_edt, 'tag');
301 para = get(h_edt, 'string');
302 save(parfile, 'tag', 'para')
```

```

303 msgbox(['Saved parameters in ' parfile ])
304
305 end
306
307 %%
308 function recv = recip_vec(latpar,latang)
309 % make reciprocal lattice vectors
310 %
311
312 cx = cos(latang(2));
313 cy = (cos(latang(1))-cos(latang(3))*cos(latang(2))) / sin(latang(1));
314 latv = [ latpar(1)*[1 0 0]; ...
315         latpar(2)*[cos(latang(3)) sin(latang(3)) 0];...
316         latpar(3)*[cx cy sqrt(1-cx^2-cy^2)] ];
317 vol = dot(latv(1,:),cross(latv(2,:),latv(3,:)));
318 recv = 2*pi/vol*[cross(latv(2,:),latv(3,:)) ;...
319                cross(latv(3,:),latv(1,:)) ;...
320                cross(latv(1,:),latv(2,:))];
321 end
322
323 function recip(h_edt,~)
324 % get reciprocal lattice information
325 %
326
327 % get lattice parameters and angles
328 h_fig = get(h_edt,'parent');
329 latpar = edit2num(h_fig, {'lat_a','lat_b','lat_c'});
330 latang = edit2num(h_fig, {'lat_alp','lat_bet','lat_gam'}) * pi/180;
331
332 recv = recip_vec(latpar,latang);
333
334 % get reciprocal lattice parameters / put in control panel
335 recpar = [norm(recv(1,:)) norm(recv(2,:)) norm(recv(3,:))];
336 recang = [acos(dot(recv(2,:),recv(3,:))/(recpar(2)*recpar(3))) ,...
337          acos(dot(recv(3,:),recv(1,:))/(recpar(3)*recpar(1))) ,...
338          acos(dot(recv(1,:),recv(2,:))/(recpar(1)*recpar(2)))] * 180/pi;
339
340 set(findobj(h_fig, 'style','edit','tag','rec_a'),'string',sprintf('%5.4f',recpar(1)))
341 set(findobj(h_fig, 'style','edit','tag','rec_b'),'string',sprintf('%5.4f',recpar(2)))
342 set(findobj(h_fig, 'style','edit','tag','rec_c'),'string',sprintf('%5.4f',recpar(3)))
343 set(findobj(h_fig, 'style','edit','tag','rec_alp'),'string',sprintf('%5.2f',recang(1)))
344 set(findobj(h_fig, 'style','edit','tag','rec_bet'),'string',sprintf('%5.2f',recang(2)))
345 set(findobj(h_fig, 'style','edit','tag','rec_gam'),'string',sprintf('%5.2f',recang(3)))
346
347 qlen(h_edt)
348 end
349
350 function qlen(h_edt,~)
351 % get reciprocal lattice from lattice information
352 %

```

## Appendix D. Codes for the spin waves calculations

---

```

353
354 % get recip. lattice parameters and angles
355 h_fig = get(h_edt,'parent');
356 latpar = edit2num(h_fig, {'lat_a', 'lat_b', 'lat_c'});
357 latang = edit2num(h_fig, {'lat_alp', 'lat_bet', 'lat_gam'}) * pi/180;
358 recv = recip_vec(latpar, latang);
359
360 % sample orientation
361 dirset = edit2num(h_fig, {'dir11', 'dir12', 'dir13';
362                          'dir21', 'dir22', 'dir23';
363                          'dir31', 'dir32', 'dir33'});
364
365 % make Q1,Q2,Qz
366 Qv = dirset*recv;
367
368 % get reciprocal lattice parameters / put in control panel
369 qleng = [norm(Qv(1,:)) norm(Qv(2,:)) norm(Qv(3,:))];
370 set(findobj(h_fig, 'style', 'edit', 'tag', 'leng1'), 'string', qleng(1))
371 set(findobj(h_fig, 'style', 'edit', 'tag', 'leng2'), 'string', qleng(2))
372 set(findobj(h_fig, 'style', 'edit', 'tag', 'leng3'), 'string', qleng(3))
373
374 end
375
376 function symmet(h_edt, ~)
377 % symmetrize resolution matrix
378 %
379 h_fig = get(h_edt, 'parent');
380 in = edit2num(h_fig, {'Res12', 'Res13', 'Res14', 'Res23', 'Res24', 'Res34'});
381
382 set(findobj(h_fig, 'style', 'edit', 'tag', 'Res21'), 'string', in(1))
383 set(findobj(h_fig, 'style', 'edit', 'tag', 'Res31'), 'string', in(2))
384 set(findobj(h_fig, 'style', 'edit', 'tag', 'Res41'), 'string', in(3))
385 set(findobj(h_fig, 'style', 'edit', 'tag', 'Res32'), 'string', in(4))
386 set(findobj(h_fig, 'style', 'edit', 'tag', 'Res42'), 'string', in(5))
387 set(findobj(h_fig, 'style', 'edit', 'tag', 'Res43'), 'string', in(6))
388
389 end
390
391 function out = edit2num(h_fig, tags)
392 out = zeros(size(tags));
393 for i=1:length(tags(:))
394     out(i) = str2double(get(findobj(h_fig, 'style', 'edit', 'tag', tags{i}), 'string'));
395 end
396 end
397
398 %% Plot
399 function dis_line(h_but, ~)
400 h_fig = get(h_but, 'parent');
401
402 % parameters

```

```

403 para = edit2num(h_fig, {'par_S', 'par_J1', 'par_J2', 'par_D1', 'par_D2', 'par_K'});
404
405 % starting point, direction, range
406 stt = edit2num(h_fig, {'line_s1', 'line_s2', 'line_s3'});
407 dir = edit2num(h_fig, {'line_d1', 'line_d2', 'line_d3'});
408 rng = edit2num(h_fig, {'line_Q1', 'line_Q2', 'line_Q3'});
409
410 Qrng = rng(1):rng(3):rng(2);
411 qpos = ones(length(Qrng),1)*stt + Qrng*dir;
412
413 tic
414 [o_eng, o_int] = calc_dis(para, qpos);
415 toc
416
417 qrng = Qrng*ones(1,9);
418 est = ceil(max(o_eng(:)))/100000;
419 r_eng = round(o_eng/est)*est;
420
421 t_eng = zeros(size(o_eng));
422 t_int = zeros(size(o_eng));
423
424 for i=1:length(Qrng)
425     temp = unique(r_eng(i,:));
426     for j=1:length(temp)
427         t_eng(i,j) = temp(j);
428         t_int(i,j) = sum(o_int(i,r_eng(i,:) == temp(j)));
429     end
430 end
431
432 % plot
433 figure('position',[200,100,500,500], 'color','w');
434 t_int = t_int(:,(size(t_int,2)-2):(size(t_int,2)));
435 nz = (t_int(:) > 0);
436 t_sz = sqrt(t_int)/sqrt(max(t_int(:))*100);
437 scatter(qrng(nz), t_eng(nz), t_sz(nz), t_int(nz), 'fill')
438
439 yrng = get(gca, 'ylim');
440 crng = get(gca, 'clim');
441 set(gca, 'ylim', [0 yrng(2)], 'clim', [0 crng(2)], 'box', 'on', 'linewidth', 1, 'fontsize', 20)
442 grid on
443
444 title({get(findobj(h_fig, 'tag', 'title'), 'string');
445     ['S= ' num2str(para(1)) ', J_1= ' num2str(para(2)) ', J_2= ' num2str(para(3))];
446     ['D_1= ' num2str(para(4)) ', D_2= ' num2str(para(5)) ', K= ' num2str(para(6))]}],...
447     'fontsize', 15)
448 sttstr = ['(' strrep(num2str(stt), ' ', ',') ')'];
449 dirstr = ['(' strrep(num2str(dir), ' ', ',') ')'];
450 xlabel([sttstr ' + q ' dirstr ' (r.l.u.)'])
451 ylabel('Energy (meV)')
452

```

```

453 end
454
455 function sim_Escan(h_but,~)
456 % simulate E-scan
457 %
458
459 h_fig = get(h_but,'parent');
460
461 % parameters
462 para = edit2num(h_fig, {'par_S', 'par_J1', 'par_J2', 'par_D1', 'par_D2', 'par_K'});
463
464 % starting point, range, # of points
465 stt = edit2num(h_fig, {'Escan_s1', 'Escan_s2', 'Escan_s3'});
466 rng = edit2num(h_fig, {'Escan_E1', 'Escan_E2', 'Escan_E3'});
467 np = edit2num(h_fig, {'Escan_np'});
468
469 Erng = rng(1):rng(3):rng(2);
470 [chi, err] = convol_Escan(h_fig, para, stt, Erng, np);
471
472 figure('position', [500, 100, 500, 500], 'color', 'w');
473 errorbar(Erng, chi, err, 'ok')
474
475 xrng = get(gca, 'xlim');
476 yrng = get(gca, 'ylim');
477 set(gca, 'xlim', [0 xrng(2)], 'ylim', [0 yrng(2)], 'box', 'on', ...
478     'linewidth', 2, 'fontsize', 20)
479 grid on
480
481 sttstr = [' strrep(num2str(stt), ' ', ',') ''];
482 title({'get(findobj(h_fig, 'tag', 'title'), 'string')',
483     ['S= ' num2str(para(1)) ', J_1= ' num2str(para(2)) ', J_2= ' num2str(para(3))];
484     ['D_1= ' num2str(para(4)) ', D_2= ' num2str(para(5)) ', K= ' num2str(para(6))];
485     ['Q=' sttstr ', np=' num2str(np)]}, 'fontsize', 15)
486 xlabel('Energy (meV)')
487 ylabel('Im\chi (arb.u.)')
488
489 end
490
491 function sim_contour(h_but,~)
492
493 h_fig = get(h_but,'parent');
494
495 % parameters
496 para = edit2num(h_fig, {'par_S', 'par_J1', 'par_J2', 'par_D1', 'par_D2', 'par_K'});
497
498 % starting point, direction, range, # of points
499 stt = edit2num(h_fig, {'cont_s1', 'cont_s2', 'cont_s3'});
500 dir = edit2num(h_fig, {'cont_d1', 'cont_d2', 'cont_d3'});
501 rng = edit2num(h_fig, {'cont_Q1', 'cont_Q2', 'cont_Q3', 'cont_E1', 'cont_E2', 'cont_E3'});
502 np = str2double(get(findobj(h_fig, 'style', 'edit', 'tag', 'cont_np'), 'string'));
    
```

---

```

503
504 Qrng = rng(1):rng(3):rng(2);
505 Erng = rng(4):rng(6):rng(5);
506
507 [X,Y] = meshgrid( Qrng, Erng );
508 Z = zeros(size(X));
509 Ze = Z;
510
511 for i=1:length(Qrng)
512     stt2 = stt + Qrng(i)*dir;
513     [Z(:,i),Ze(:,i)] = convol_Escan(h_fig,para,stt2,Erng,np);
514 end
515
516 figure('position',[500,100,500,500]);
517
518 pcolor(X,Y,Z); axis xy; shading interp;
519
520 yrng = get(gca,'ylim');
521 crng = get(gca,'clim');
522 set(gca,'ylim',[0 yrng(2)],'clim',[0 crng(2)],'box','on','layer','top',...
523     'linewidth',2,'fontsize',20)
524
525 title({get(findobj(h_fig,'tag'),'title'),'string'};
526     ['S= ' num2str(para(1)) ', J_1= ' num2str(para(2)) ', J_2= ' num2str(para(3))];
527     ['D_1= ' num2str(para(4)) ', D_2= ' num2str(para(5)) ', K= ' num2str(para(6))]],...
528     'fontsize',15)
529 sttstr = ['(' strrep(num2str(stt),' ',' ') ')'];
530 dirstr = ['(' strrep(num2str(dir),' ',' ') ')'];
531 xlabel([sttstr ' + q ' dirstr ' (r.l.u.)'])
532 ylabel('Energy (meV)')
533 end

```



## References

- [1] I. Dzyaloshinsky, Zh. Eksp. Teor. Fiz. **37**, 881 (1959), [Sov. Phys.-JETP **10**, 628 (1960)].
- [2] D. N. Astrov, Zh. Eksp. Teor. Fiz. **38**, 984 (1960), [Sov. Phys.-JETP **11**, 708 (1961)].
- [3] G. A. Smolenskii and I. E. Chupis, Sov. Phys. Uspekhi **25**, 475 (1982).
- [4] Y. N. Venevtsev and V. V. Gagulin, Ferroelectrics **162**, 23 (1994).
- [5] I. Dzyaloshinsky, J. Phys. Chem. Solids **4**, 241 (1958).
- [6] T. Moriya, Phys. Rev. **120**, 91 (1960).
- [7] H. Schmid, Ferroelectrics **162**, 317 (1994).
- [8] N. A. Hill, J. Phys. Chem. B **104**, 6694 (2000).
- [9] N. A. Spaldin and M. Fiebig, Science **309**, 391 (2005).
- [10] W. Eerenstein, N. D. Mathur, and J. F. Scott, Nature **442**, 759 (2006).
- [11] S.-W. Cheong and M. Mostovoy, Nature Materials **6**, 13 (2007).
- [12] R. Ramesh and N. A. Spaldin, Nature Materials **6**, 21 (2007).
- [13] M. Fiebig, J. Phys. D **38**, R123 (2005).
- [14] D. Khomskii, J. Magn. Magn. Mater. **306**, 1 (2006).
- [15] T. Kimura, Annual Review of Materials Research **37**, 387 (2007).
- [16] Y. Tokura and S. Seki, Advanced Materials **22**, 1554 (2010).
- [17] Y. Noda, H. Kimura, M. Fukunaga, S. Kobayashi, I. Kagomiya, and K. Kohn, J. Phys.: Condens. Matter **20**, 434206 (2008).
- [18] D. I. Khomskii, *Transition Metal Compounds*, 1st ed. (Cambridge University Press, Cambridge, 2014).
- [19] I. A. Sergienko and E. Dagotto, Phys. Rev. B **73**, 094434 (2006).

- [20] T. Arima, A. Tokunaga, T. Goto, H. Kimura, Y. Noda, and Y. Tokura, *Phys. Rev. Lett.* **96**, 097202 (2006).
- [21] H. Katsura, N. Nagaosa, and A. V. Balatsky, *Phys. Rev. Lett.* **95**, 057205 (2005).
- [22] D. Khomskii, *Physics* **2**, 20 (2009).
- [23] T. Kimura, T. Goto, H. Shintani, K. Ishizaka, T. Arima, and Y. Tokura, *Nature* **426**, 55 (2003).
- [24] O. Heyer, N. Hollmann, I. Klassen, S. Jodlauk, L. Bohatý, P. Becker, J. A. Mydosh, T. Lorenz, and D. Khomskii, *J. Phys.: Condens. Matter* **18**, L471 (2006).
- [25] N. Ikeda, H. Ohsumi, K. Ohwada, K. Ishii, T. Inami, K. Kakurai, Y. Murakami, K. Yoshii, S. Mori, Y. Horibe, and H. Kitô, *Nature* **436**, 1136 (2005).
- [26] Y. Choi, H. Yi, S. Lee, Q. Huang, V. Kiryukhin, and S.-W. Cheong, *Phys. Rev. Lett.* **100**, 047601 (2008).
- [27] M. Fiebig, C. Degenhardt, and R. V. Pisarev, *J. Appl. Phys.* **91**, 8867 (2002).
- [28] S. Lee, A. Pirogov, M. Kang, K.-H. Jang, M. Yonemura, T. Kamiyama, S.-W. Cheong, F. Gozzo, N. Shin, H. Kimura, Y. Noda, and J.-G. Park, *Nature* **451**, 805 (2008).
- [29] J. Oh, M. Le, J. Jeong, J.-h. Lee, H. Woo, W.-Y. Song, T. Perring, W. Buyers, S.-W. Cheong, and J.-G. Park, *Phys. Rev. Lett.* **111**, 257202 (2013).
- [30] H. Ishiwara, *Current Applied Physics* **12**, 603 (2012).
- [31] D. Lebeugle, A. Mougin, M. Viret, D. Colson, and L. Ranno, *Phys. Rev. Lett.* **103**, 257601 (2009).
- [32] J. Wang, J. B. Neaton, H. Zheng, V. Nagarajan, S. B. Ogale, B. Liu, D. Viehland, V. Vaithyanathan, D. G. Schlom, U. V. Waghmare, N. A. Spaldin, K. M. Rabe, M. Wuttig, and R. Ramesh, *Science* **299**, 1719 (2003).
- [33] S. Ishiwata, Y. Taguchi, H. Murakawa, Y. Onose, and Y. Tokura, *Science* **319**, 1643 (2008).

- 
- [34] T. Kimura, G. Lawes, and A. Ramirez, *Phys. Rev. Lett.* **94**, 137201 (2005).
- [35] S. H. Chun, Y. S. Chai, Y. S. Oh, D. Jaiswal-Nagar, S. Y. Haam, I. Kim, B. Lee, D. H. Nam, K.-T. Ko, J.-H. Park, J.-H. Chung, and K. H. Kim, *Phys. Rev. Lett.* **104**, 037204 (2010).
- [36] J.-G. Park, M. D. Le, J. Jeong, and S. Lee, *Journal of Physics: Condensed Matter* **26**, 433202 (2014).
- [37] D. Lebeugle, D. Colson, A. Forget, M. Viret, P. Bonville, J. F. Marucco, and S. Fusil, *Phys. Rev. B* **76**, 024116 (2007).
- [38] W. Eerenstein, F. D. Morrison, J. Dho, M. G. Blamire, J. F. Scott, and N. D. Mathur, *Science* **307**, 1203; author reply 1203 (2005).
- [39] J. Wang, A. Scholl, H. Zheng, S. B. Ogale, D. Viehland, D. G. Schlom, N. A. Spaldin, K. M. Rabe, M. Wuttig, L. Mohaddes, J. Neaton, U. Waghmare, T. Zhao, and R. Ramesh, *Science* **307**, 1203b (2005).
- [40] H. Béa, M. Bibes, S. Petit, J. Kreisel, and A. Barthélémy, *Philosophical Magazine Letters* **87**, 165 (2007).
- [41] T. Choi, S. Lee, Y. J. Choi, V. Kiryukhin, and S.-W. Cheong, *Science* **324**, 63 (2009).
- [42] J. Jeong, E. A. Goremychkin, T. Guidi, K. Nakajima, G. Jeon, S.-A. Kim, S. Furukawa, Y. Kim, S. Lee, V. Kiryukhin, S.-W. Cheong, and J.-G. Park, *Phys. Rev. Lett.* **108**, 077202 (2012).
- [43] J. Moreau, C. Michel, R. Gerson, and W. James, *J. Phys. Chem. Solids* **32**, 1315 (1971).
- [44] Y. E. Roginskaya, Y. Y. Tomashpol'skii, Y. N. Venevtsev, V. Petrov, and G. Zhdanov, *Zh. Eksp. Teor. Fiz.* **50**, 69 (1966), [*Sov. Phys.-JETP* **23**, 47 (1966)].
- [45] W. Kaczmarek, M. Polomska, and Z. Pajak, *Phys. Lett. A* **47**, 227 (1974).
- [46] S. V. Kiselev, R. P. Ozerov, and G. S. Zhdanov, *Dokl. Akad. Nauk. SSSR* **145**, 1255 (1962), [*Sov. Phys. Dokl.* **7**, 742 (1962)].

- [47] R. Haumont, J. Kreisel, P. Bouvier, and F. Hippert, *Phys. Rev. B* **73**, 132101 (2006).
- [48] S. M. Selbach, T. Tybell, M.-A. Einarsrud, and T. Grande, *Advanced Materials* **20**, 3692 (2008).
- [49] I. Kornev, S. Lisenkov, R. Haumont, B. Dkhil, and L. Bellaiche, *Phys. Rev. Lett.* **99**, 227602 (2007).
- [50] D. Arnold, K. Knight, F. Morrison, and P. Lightfoot, *Phys. Rev. Lett.* **102**, 027602 (2009).
- [51] R. Haumont, I. Kornev, S. Lisenkov, L. Bellaiche, J. Kreisel, and B. Dkhil, *Phys. Rev. B* **78**, 134108 (2008).
- [52] S. Lee, M. T. Fernandez-Diaz, H. Kimura, Y. Noda, D. T. Adroja, S. Lee, J. Park, V. Kiryukhin, S.-W. Cheong, M. Mostovoy, and J.-G. Park, *Phys. Rev. B* **88**, 060103 (2013).
- [53] I. Sosnowska and A. Zvezdin, *J. Magn. Magn. Mater.* **140-144**, 167 (1995).
- [54] Y. Popov and A. Zvezdin, *JETP Letters* **57**, 65 (1993).
- [55] I. Sosnowska and R. Przeniosło, *Phys. Rev. B* **84**, 144404 (2011).
- [56] M. Ramazanoglu, M. Laver, W. Ratcliff, S. M. Watson, W. C. Chen, A. Jackson, K. Kothapalli, S. Lee, S.-W. Cheong, and V. Kiryukhin, *Phys. Rev. Lett.* **107**, 207206 (2011).
- [57] J. Jeong, M. D. Le, P. Bourges, S. Petit, S. Furukawa, S.-A. Kim, S. Lee, S.-W. Cheong, and J.-G. Park, *Phys. Rev. Lett.* **113**, 107202 (2014).
- [58] J. Jeong, S. Lee, and J.-G. Park, *J. Korean Magn. Soc.* **22**, 103 (2012).
- [59] T. E. Mason, *Physics Today* **59**, 44 (2006).
- [60] <http://www.mlz-garching.de/englisch/neutron-research/experimental-methods/inelastic-scattering.html>.
- [61] M. Nakamura, R. Kajimoto, Y. Inamura, F. Mizuno, M. Fujita, T. Yokoo, and M. Arai, *Journal of the Physical Society of Japan* **78**, 093002 (2009).

- 
- [62] A. M. Kadomtseva, A. K. Zvezdin, Y. F. Popov, A. P. Pyatakov, and G. P. Vorobév, *JETP Letters* **79**, 571 (2004).
- [63] A. K. Zvezdin and A. P. Pyatakov, *Europhys. Lett.* **99**, 57003 (2012).
- [64] R. S. Fishman, N. Furukawa, J. T. Haraldsen, M. Matsuda, and S. Miyahara, *Phys. Rev. B* **86**, 220402 (2012).
- [65] Z. Xu, J. Wen, T. Berlijn, P. M. Gehring, C. Stock, M. B. Stone, W. Ku, G. Gu, S. M. Shapiro, R. J. Birgeneau, and G. Xu, *Phys. Rev. B* **86**, 174419 (2012).
- [66] R. S. Fishman, *Phys. Rev. B* **87**, 224419 (2013).
- [67] R. Fishman, J. Haraldsen, N. Furukawa, and S. Miyahara, *Phys. Rev. B* **87**, 134416 (2013).
- [68] C. Weingart, N. Spaldin, and E. Bousquet, *Phys. Rev. B* **86**, 094413 (2012).
- [69] J. H. Lee and R. S. Fishman, private communication.
- [70] A. V. Zalesskii, A. K. Zvezdin, A. A. Frolov, and A. A. Bush, *JETP Letters* **71**, 465 (2000).
- [71] A. V. Zalesskii, A. A. Frolov, A. K. Zvezdin, A. A. Gippius, E. N. Morozova, D. F. Khozevc, A. S. Bush, and V. S. Pokatilov, *J. Exp. Theor. Phys.* **95**, 101 (2002).
- [72] A. Palewicz, T. Szumiata, R. Przeniosło, I. Sosnowska, and I. Margiolaki, *Sol. State. Comm.* **140**, 359 (2006).
- [73] R. Przeniosło, M. Regulski, and I. Sosnowska, *J. Phys. Soc. Japan* **75**, 084718 (2006).
- [74] R. Przeniosło, A. Palewicz, M. Regulski, I. Sosnowska, R. M. Ibberson, and K. S. Knight, *J. Phys.: Condens. Matter* **23**, 279501 (2011).
- [75] M. Ramazanoglu, W. Ratcliff, Y. J. Choi, S. Lee, S.-W. Cheong, and V. Kiryukhin, *Phys. Rev. B* **83**, 174434 (2011).
- [76] P. Rovillain, R. de Sousa, Y. Gallais, A. Sacuto, M. A. Méasson, D. Colson, A. Forget, M. Bibes, A. Barthélémy, and M. Cazayous, *Nature Materials* **9**, 975 (2010).

- [77] R. de Sousa, M. Allen, and M. Cazayous, *Phys. Rev. Lett.* **110**, 267202 (2013).
- [78] T. Holstein and H. Primakoff, *Phys. Rev.* **58**, 1098 (1940).
- [79] A. Yoshimori, *Journal of the Physical Society of Japan* **14**, 807 (1959).
- [80] S. Furukawa and Y. B. Kim, private communication.
- [81] K. Ohoyama, S. Lee, S. Yoshii, Y. Narumi, T. Morioka, H. Nojiri, G. Jeon, S.-W. Cheong, and J.-G. Park, *J. Phys. Soc. Japan* **80**, 125001 (2011).
- [82] M. Matsuda, R. S. Fishman, T. Hong, C. H. Lee, T. Ushiyama, Y. Yanagisawa, Y. Tomioka, and T. Ito, *Phys. Rev. Lett.* **109**, 067205 (2012).
- [83] Y. Wang, J. E. Saal, P. Wu, J. Wang, S. Shang, Z.-K. Liu, and L.-Q. Chen, *Acta Materialia* **59**, 4229 (2011).
- [84] A. K. Zvezdin and A. P. Pyatakov, *physica status solidi (b)* **246**, 1956 (2009).
- [85] A. Palewicz, I. Sosnowska, R. Przeniosło, and A. W. Hewat, *Acta Physica Polonica A* **117**, 296 (2010).
- [86] R. de Sousa and J. Moore, *Phys. Rev. B* **77**, 012406 (2008).
- [87] M. Ramazanoglu, W. Ratcliff, H. T. Yi, A. A. Sirenko, S.-W. Cheong, and V. Kiryukhin, *Phys. Rev. Lett.* **107**, 067203 (2011).
- [88] H.-S. Kim and J. Yu, private communication.

## 국문초록

# 다강체 $\text{BiFeO}_3$ 의 스핀동역학 연구: Dzyaloshinskii-Moriya 상호작용과 비등방성의 상호 영향

정재홍

물리천문학부 물리학전공

서울대학교 대학원

강유전성과 자성을 동시에 보이는 다강성 물질은 두 가지 서로 다른 질서변수가 함께 공존하는 성질과 그들 사이의 상호작용 때문에 매우 흥미로운 물질이다. 특히 다강성 물질은 자기전기 상호작용을 이용한 새로운 소자 개발을 위해 폭넓게 연구되었다. 비스머트 철산화물  $\text{BiFeO}_3$ 의 강유전성 상전이 온도와 반강자성 상전이 온도는 각각 약 1100 K과 640 K로 상온 이상에서 다강성을 가지는 유일한 물질이며 따라서 이러한 소자개발에 매우 적합하다. 이 물질은 또한 620 Å의 매우 긴 주기의 엇맞는 사이클로이드 및 그에 수직방향으로의 스핀 기울어짐에 의한 약한 강자성을 포함하는 복잡한 자기구조를 가지고 있다. 이러한 복잡한 자기구조 및 자기전기 상호작용을 이해하기 위해 스핀동역학을 연구하고 스핀 해밀토니안을 결정하는 것은 매우 중요한 일이다.

이 논문은 단결정을 이용한 비탄성 중성자산란 실험을 통해  $\text{BiFeO}_3$ 의 마그논 및 포논 들뜸 현상을 측정하고 근본적인 스핀 해밀토니안을 구하는 연구를 자세히 다룬다. 비탄성 중성자산란 실험은 자성 들뜸 현상을 관찰하는 데 매우 효과적이지만 큰 단결정이 필요하다. 실험을 위해 한국원자력연구원의 연구용 원자로 하나로의 사축회절장치 FCD를 이용하여 전체 질량 1.9 g의 10개의 단결정을 2도 이하의 각도로 정렬하였다. 전체 브릴루앙 영역에 대한 스핀과 분산 관계를 비행시간 분광장치인 일본 J-PARC 연구소의 AMATERAS와 영국 ISIS 연구소의 MERLIN을 이용하여 측정하였다. 에너지 72.5 meV에 걸친 전체 스핀파는 최근접 이웃과 다음근접 이웃 사이의 교환상호작용을 포함하는 간단한 스핀 해밀토니안으로 잘 설명된다. 복잡한 자기구조에서 비롯되는 작은 변화를 관찰하기 위해 브릴루앙 영역 중심에서 낮은 에너지 영역의 마그논 들뜸을 삼축분광장치인 프랑스 LLB 연구소의 4F2와 1T1를 이용하여 측정하였다. 낮은 에너지 마그논 들뜸은 Dzyaloshinskii-Moriya 상호작용과 단원자 비등방성의

상호 영향으로 인한 독특한 모습을 보였다. 이 두 가지 상호작용은 이 물질의 특이한 자기구조와 자기전기 상호작용을 이해하는 데 가장 중요하다. 전체 스핀 해밀토니언을 이용하여 마그논 분산관계를 이론적으로 계산하기 위해 회전틀에서의 선형 스핀파 이론을 이용하여 복잡한 바닥상태에 대한 섭동적 접근방법을 개발하였다. 여러 가지 모형에 대한 계산결과와 실험결과를 비교하여 스핀 해밀토니언의 모든 상수를 온도에 따라 결정하였다. 쉬운 축 비등방성을 확인하였고 스핀 사이클로이드의 비조화도를 구하였다. 상수들의 온도에 따른 변화는 물성 및 구조 변화 경향과 직접적으로 연결되어 있다. 비탄성 중성자산란 실험의 넓은 측정 범위를 이용하여 포논 분산관계 또한 측정할 수 있었다.

**주요어:** 다강성,  $\text{BiFeO}_3$ , 마그논, 스핀파, 비탄성중성자산란

**학 번:** 2007-20440